MASTER'S DEGREE IN MICRO AND NANOTECHNOLOGIES FOR INTEGRATED SYSTEMS

Master's Degree Thesis

Fabrication and Characterization of wide band gap semiconductors for ultraviolet sensing, based on ZnO nanoparticles and bulk SiC

Supervisors

Prof. Giancarlo CICERO

Daily Supervisors

PhD. Hendrik Joost VAN GINKEL

PhD. Joost ROMIJN

Prof. Sten VOLLEBREGT

Candidate

Mattia ORVIETANI

08-2022

Abstract

The aim of the project described in the following consists on the fabrication, optimization and characterization of ultraviolet (UV) photodetectors based on wide band gap (WBG) semiconductors.
The fabrication will imply devices based only zinc oxide (ZnO) nanoparticles based devices. The process consist of wafer level patterning of metallic electrodes to contact the ZnO nanoparticle film. The last step performed involves the deposition of the metal nanoparticles through the combination of spark ablation and impaction printing technology trying to create a conductive path between electrodes at die level. The obtained devices undergo a thermal treatment in order to fully oxidize the zinc particles and thus obtaining only a zinc oxide phase, taking into account the temperature effect on the metal electrodes.
A morphology analysis has been carried out to understand the roughness and porosity of the film deposited, but anyhow their relevance for the purpose of the material is not really effective for the photodetection mechanism.
An electrical characterization of the devices obtained, and other already fabricated photodiode based on silicon carbide SiC. The performances of ZnO samples has been tested in different operating conditions (temperature and light effect).
Optical characterization involves both the devices based on the WBG semiconductor which imply the measurement of the optical response of the DUT stimulated by different monochromatic light, then the evaluation of the response time.
Finally, we will sum up with the final data and importance aspects to take into account regarding the production method and performances showing their benefits and drawbacks.

Le projet décrit ci-après a pour objet: la fabrication, l'optimisation et la caractérisation de photodétecteurs à rayons ultraviolets (UV) basés sur des semi-conducteurs à large bande (WBG). La fabrication impliquera des dispositifs à base uniquement d'oxyde de zinc (ZnO) des dispositifs à base de nanoparticules. Le procédé consiste à modeler au niveau de la plaquette différents métaux indispensables comme électrodes de contact de nanoparticules de zinc, afin de comprendre quel type de contact sera mis en place. La dernière étape consiste à déposer les nanoparticules métalliques grâce à la combinaison de l'ablation d'étincelles et de la technologie d'impression par impaction en essayant de créer un chemin conducteur entre les électrodes au niveau des matrices. Les appareils obtenus subissent un traitement thermique afin d'oxyder complètement la particule de zinc et d'obtenir ainsi seulement une phase d'oxyde de zinc, en tenant compte de l'effet de température sur les électrodes métalliques. Une analyse morphologique a été effectuée pour comprendre la rugosité et la porosité du film déposé, mais de toute façon leur pertinence pour le but du matériau n'est pas vraiment efficace pour le mécanisme de photodétection. Une caractérisation électrique des dispositifs obtenus et d'autres photodiodes déjà fabriquées à base de carbure de silicium SiC. Les performances des échantillons ZnO ont été testées dans différentes conditions de fonctionnement (température et effet de la lumière). La caractérisation optique implique à la fois les dispositifs basés sur le semi-conducteur WBG qui impliquent la mesure de la réponse optique du DUT stimulée par une lumière monochromatique différente, puis l'évaluation du temps de réponse. Enfin, nous résumerons avec les données finales et les aspects d'importance à prendre en compte en ce qui concerne la méthode de production et les performances montrant leurs avantages et inconvénients.

Table of Contents

List of Figures

Acronyms

WBG
wide band gap

NP
nanoparticle

RT
room temperature

UV
ultraviolet

PD
photodetector

DFT
density functional theory

LDA
local density approximations

MSM
metal-semiconductor-metal

DUT
device under test

LED
light emitting diode

SEM
scanning electron microscope

AFM

atomic force microscope

EDS

energy dispersive spectroscopy

DIP

dual in package

PCB

printed circuit board

BZ

brillouin zone

VIS

visible

NIR

near infrared

Chapter 1

Introduction

In the last few decades, the need of advanced and reliable UV PD's has grown widely in field such as solar UV monitoring, emitter calibration lithography aligners, secure, space-to-space communications, astronomical studies [1]. The UV spectrum ranges from 100 nm to 400 nm, just below the shortest wavelengths of the visible spectrum. As shown in *figure 1.1*, the spectrum is further subdivided into UVA, UVB, UVC, and VUV. This additional characterization is required because even minor differences in the energy of UV radiation can result in different effects on biological or chemical substances. The harmful effects of sunlight on biological systems are almost entirely due to radiation from the Sun's ultraviolet spectrum.

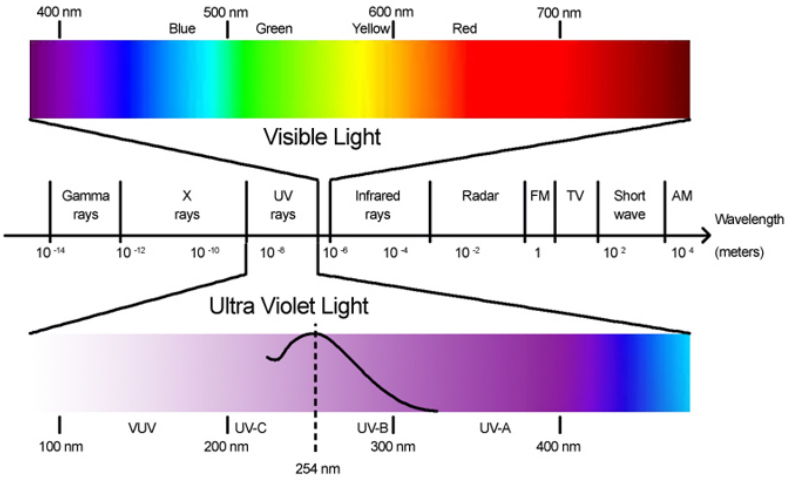

Figure 1.1: Electromagnetic spectrum

The ozone layer, on the other hand, absorbs radiation with wavelengths shorter than 280nm, resulting in a region known as the "solar blind region." Similarly, the radiation above 280nm and below 400nm is referred to as the "visible-blind region" of the spectrum because these wavelengths are not imperceptible to human being. UV radiation has beneficial effects; for example, UVA stimulates photosynthesis and vitamin synthesis, whereas UVB activates vitamin D. At the same time, it is widely accepted that UV radiation has a negative impact on humans. Prolonged UVA exposure causes sunburn and premature aging, whereas UVB causes skin cancer and cataracts. UVC is the most dangerous of the three because of its

high concentration which may cause DNA ionization and cause severe mutations. However, the requirements of UV instrumentation capable of working in harsh environments, high temperature and extreme radiation conditions have drawn the attention to wide band gap semiconductor. Among the large available choice, particular interest has given to GaN or SiC, but also ZnO, may have an impact [1].

Chapter 2

State of the Art

2.1 WBG semiconductor

Semiconductors differ from insulators and metal for their conductivity behaviour which leans on their band structure. The conduction and valence energy are split and they do not overlap a in case of metal materials. At the same time, the separation between conduction electrons and valence electrons is not high as compared to insulator, where the valence electrons are tighten within their band without jumping in the conduction band. Furthermore, the possibility to tune the conductivity of these materials by external impurities make the largest and widest material used in microelectronics. Despite of the well known crystallize semiconductor, such as Ge, Si with an energy gap of 0.6 eV and 1.12 eV respectively at RT, an underclass of these type of material has been identified as wide band gap semiconductor, which shows similar property to standard semiconductor but they have different intrinsic characteristic, examples are GaN, 4H-SiC with an energy gap of 3.4 eV and 3.24 eV respectively at RT.
According to Shockley model, the free carriers conduction (and valence) follow an exponential law related to the position of the Fermi level with respect to the conduction (and valence) energy, by combining this equations with the mass action is possible to determine an approximate estimation of the relationship between the energy gap of a semiconductor and its intrinsic carriers, as reported in *equation 2.1*.

$$n_i(T) = \sqrt{n(T)p(T)} = \sqrt{N_c(T)N_v(T)}e^{\frac{E_g(T)}{2k_bT}} \tag{2.1}$$

where $N_c(T)$ and $N_v(T)$ are the conduction and valence band effective density of state, which are generally $\propto T^{\frac{3}{2}}$ and $E_g(T)$ is the energy gap which also is dependent on temperature, but its behaviour is extremely dependent on the crystallography structure of the concerned material, therefore is hard to make any prediction, for a deeper insight [2]. The evaluations of intrinsic carrier for different doped WBG semiconductor (both n an p-type) with atoms above 10^{15}cm^{-3} at different temperature condition as depicted in *figure 2.1*, shows that even at high temperature the electronic properties will remain unaffected, making them reliable and stable, while for lower band gap semiconductors there is a huge change, where extrinsic carriers become comparable to intrinsic ones, affecting their conductivity thus modifying their operating condition and behaviour.

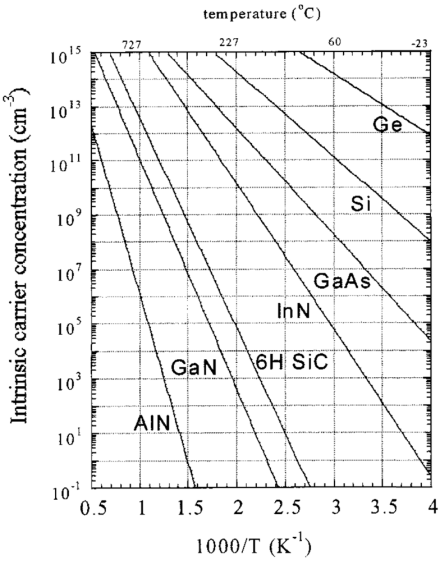

Figure 2.1: Comparison of intrinsic carrier concentration in semilogaritmic scale between wide band (6H-SiC, GaN, AlN) and low band gap (Si, GaAs, Ge) semiconductor [3]

Moreover, in power applications, generally large current flows in the semiconductor device implying high power dissipation in its resistance as well as considerable instantaneous dynamic power dissipation appears during on-off switching operation. Those power dissipation sources increases the internal temperature even beyond the surrounding temperature, which influence badly their performances. However, as reported in *table 2.1*, high-drift saturation velocity, thermal conductivity, high-breakdown electric field of WBG make them the optimal choice in this field.

Property	**Si**	**GaAs**	**4H-SiC**	**6H-SiC**	**2H-GaN**
Badgap @ RT [eV]	1.1	1.42	3.2	3.0	3.4
Dielectric constant (ϵ_r)	11.9	13.1	9.7	9.7	9.5
Breakdown electric field at $N_D = 10^{17}$cm [MV/cm^{-3}]	0.6	0.6	3	3.2	2-3
Intrinsic carrier concentration [cm^{-3}]	10^{10}	1.8×10^6	$\sim 10^{-7}$	$\sim 10^{-5}$	$\sim 10^{-10}$
Electron mobility at $N_D = 10^{16}$ [cm^2/V s]	1200	6500	800	$60 - 400$	900
Hole mobility at $N_D = 10^{16}$ [cm^2/V s]	420	320	115	90	200
Saturated electron velocity [10^7cm/s]	1.0	1.2	2	2	2.5
Thermal conductivity [W/mK]	150	55	400	480	130

Table 2.1: Examples of [3].

Figure performances Si SiC and GaN in all the importance FoM Despite of these common characteristics that these kind of semiconductors share, the material properties and structures

change also their electrical and thermal characteristic, therefore we are going to give particular attention only to the WBG of proper interest: ZnO and SiC.

2.1.1 Zinc Oxide (ZnO)

Zinc oxide (ZnO) belongs to the family of metal-oxide semiconductor and the anion respectively. As most of the group-II(A-B)-VI binary compound semiconductor (such as MgO or CdO), zinc oxide tends to form a covalent bond between the anion and cation configured in a sp^3 hybridization, with a residual ionic behaviour. In nature, it may be found with three different crystallographic structure: wurtzite, zinc blende, and rocksalt (NaCl), , but at RT and atmospheric pressure the most likely to form is the wurtzite one.

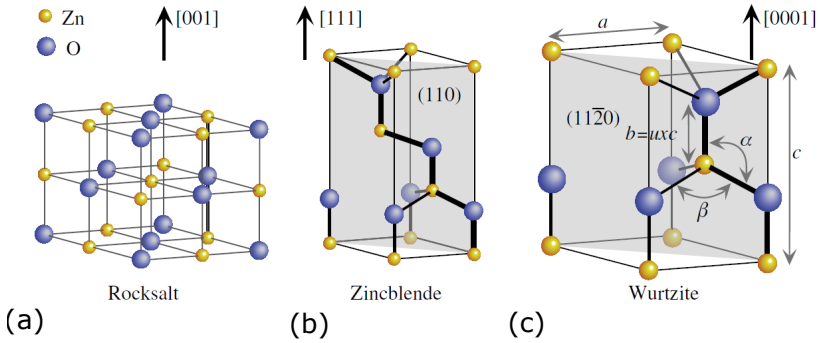

Figure 2.2: (a) cubic rocksalt,(b) cubic zinc blende (c) hexagonal wurtzite. [4].

The wurtzite configuration, *figure 2.2.c*, consist on an hexagonal self packed unit cell with two lattice parameters, a and c, for the in plane and out of plane axis, composed of two interpenetrating hexagonal-closed packed (hcp) sublattices, inside which each atom is surrounded by another one along the threefold c-axis. Within each sublattice there are four atoms per unit cell, each of one material (group VI) is bond to other four of the other one (group II-B), displaced at the edges of a tetrahedron and vice versa, whose arrangement remain stable also over the long-range polar interactions. At moderate hydrostatic pressure ZnO shows a substantial transformation from a wurtzite phase to a rocksalt structure, *figure 2.2.a*. This phenomena occurs at a pressure approximated four order of magnitude larger than the atmospheric pressure, for then remaining stable for long periods even at normal atmospheric pressure but above 100 °C, inducing also an evident decrease in the lattice constant value. This crystallographic consist of a cubic (cP) lattice where each atom at the edge of the cell is either Zn or O, with neighbouring atoms is O or Zn, respectively. The reason of the change is that the prevalence of a ionicity behaviour over the covalent in the coulombic interaction between the atoms. A further increase in pressure cause ZnO to rearrange its structure from a simple cubic phase (sixfold-coordinates) to the eightfold-coordinates (CsCl). The last phase is the zinc blende *figure 2.2.b*. Despite of the previous two configurations, it has been found to be metastable and forms on particular condition (heteroepitaxial growth on cubic structures for example ZnS). The unit cell is characterized by two interpenetrating face center cubic (fcc) sublattices shifted along the body diagonal by one-quarter of a body diagonal. As for wurtzite phase, four atoms per unit cell and every atom of one type (group II-B) is tetrahedrally coordinated with four atoms of the other type (group VI), and vice versa. The main differences between the latter mentioned is their stacking sequence, for which the

wurtzite structure consists of triangularly arranged alternating biatomic close-packed (0001) planes, while the zinc blende consists of triangularly arranged atoms in the closed-packed (111) planes along the $\langle 111 \rangle$ direction [5].
Concerning the main features of bulk and thin film zinc oxide, despite of several mechanical aspects, like hardness, stiffness, bulk moduli, piezoelectricity acquires most of the attention. The piezoelectric tensor, which fully describes this peculiar property, is composed of three independent components in hexagonal wurtzite phase, two of them measure the polarization induced along the *c*-axis at zero electric field by a uniform strain either along the *c*-axis itself or in the perpendicular plane, and one regarding the polarization induced by a shear strain. Only one, instead, is measured in the simple cubic-zinc blende phase. In its natural structure, that is wurtzite, zinc oxide shows remarkably high spontaneous piezoelectric tensor if compared to other similar types of tetrahedrally bonded compound, as for instance GaN. The main reason lies on the low symmetry arrangement of anion and cation which is given by two mainly contributions: "clamped ion" and "internal strain", due mostly on the internal relaxation of zinc and oxygen, whereas the high robustness and symmetry of the other two phase do not reveal this aspect. Various theoretical studies as well as experiments has been adopted to measure these piezoelectric tensors [5], and it has been verified that it is very sensitive to both temperature and external stress, changing by approximately 20% and $15\% - 30\%$ respectively in the range of [100, 400] K and [-1, 1] GPa [6].
Being an oxide, the thermal conductivity, κ, is fairly low, although is dependent on the imperfections on the crystal. Indeed, the main contributions arises form the lattice contributions (phonon-phonon scattering) and phonon scattering with impurities or point defect in he crystal. At relatively low temperature (like RT) the $\kappa_{lattice}$ is dominant, determined by the specific heat which is a quantitative parameter of the lattice vibrations and it is generally low [7]. Reaching higher temperature condition, $\kappa_{carriers}$ start playing a role in the thermal conductivity overcoming the lattice component due to increased phonon scattering from both the impurities and free carriers concentrations [5].
ZnO may be produced both as bulk or thin film. The growth of large-area and high quality ZnO crystal will be favorable for the creation of UV, blue light emitting diode devices, acting as satisfactory substrate for homoepitaxy, and also heteroepitaxial growth of GaN-based active layer. The main growth mechanism adopted for zinc monoxide are hydrothermal, vapor phase, and melt growth. According its high vapor pressure, development of ZnO when melt is troublesome, and development by vapor-phase is challenging to monitor. The aqueous development of the quartz crystal has been deeply grounded, being the most suitable among the mentioned. The aqueous technique utilizes ZnO single-crystal seeds (suspended by Pt wire), and sintered ZnO strings along with a KOH and LiOH fluid arrangement are utilized as a supplement. The seeds furthermore, the supplement are set into a Pt pot. This cauldron is fixed by welding and put in an autoclave. The autoclave is then positioned into a two-zone vertical heater. ZnO is moved from the supplement in the higher-temperature zone to the seeds in the lower-temperature zone. The produced material inevitably will incorporate alkali metals being and small quantity of metallic impurities due to the required procedure. Higher crystal quality bulk ZnO may be achieved through vapor transport. The reaction happens in an almost shut even tube. Pure ZnO powder utilized as source is put at the hot end of the cylinder which is kept at high temperature. The material is moved to the cooler finish of the cylinder by involving H_2 as a transporter gas. A transporter gas is essential since the vapour phase of O and Zn are very low with respect to the zinc oxide. At the cooler end, ZnO is formed by thermal reaction with vapour water and pure zinc split at the opposite

part of the chamber. Another method for producing bulk ZnO is that of melt. Relying, a compressed enlistment liquefying mechanical assembly. The dissolve is contained in a cooled pot. Zinc oxide powder is utilized as the beginning material. The intensity source utilized during the liquefying activity is radio recurrence RF energy, enlistment warming. The RF energy produces joule warming until the ZnO is liquid at about 1,900 °C. When the liquid state is accomplished, the cauldron is gradually brought down away from the warmed zone to let the material crystallize.
More experimental technique are implemented for the deposition and growth of thin film: molecular-beam epitaxy (MBE), pulsed-laser deposition (PLD), metal-organic chemical-vapor deposition (MOCVD), and hydride or halide vapor-phase epitaxy (HVPE).
Several substrate has been studied for ZnO deposition. Generally sapphire substrates are used for ZnO heteroepitaxial growth given the close matched lattice parameter, but has been also grown on Si, SiC, GaAs, CaF_2 through other experimental tool. The ZnO layers have been grown successfully on sapphire by using a variety of growth techniques, including PLD, MOCVD, and MBE. However to eliminate in-plane domain rotation, several lattice-matched substrates have been furhter studied such as $SCAlMgO_4$ substrates by laser-assisted MBE or $LiTaO_3$ and $LiNbO_3$ substrates by electron-cyclotron resonance-assisted MBE.
The most popular technique is sputtering (Dc sputtering, Rf magnetron sputtering, and reactive sputtering) owing to its ow cost, simplicity, and low operating temperature. ZnO films grow at a certain substrate temperature(ranging from 300 °C to 1,000 °C) by sputtering from a high-purity ZnO target using a Rf magnetron sputter system.
MBE offers, instead, a better control over the deposition parameters and *in situ* diagnostic capabilities. With the feedback from reflection high-energy electron diffraction (RHEED), the development of ZnO epilayers can be progressively surveyed. O_2 and high pure Zn metal are usually the source materials, where the latter is evaporated from an emission cell, whose temperature can be shifted to inspect the impact of the Zn motion on the development rate, meanwhile the oxygen radical shaft is guided on the film surface to get an high-oxidation quality (other gas precursor are also used such as H_2O_2, NO_2).
For large production and reasonably high purity chemical-vapor deposition (CVD) technology is of particular interest, called MOCVD, metal-organic vapor-phase epitaxy, when metal-organic precursors are used. ZnO deposition happens because of chemical reaction of a vapor-phase molecules on the substrate, which are conveyed into the development area by the transporter gas. The responses takes place in a reactor where a fundamental temperature profile is made in the gas stream direction. generally a solid ZnO target and H_2 are employed in CVD while metal alkyls, usually dimethyl zinc $(CH_3)_2Zn$ DMZn or diethyl zinc $(C_2H_5)_2Zn$ DEZn in combination with a separate source of oxygen and argon ion MOCVD. PLD, pulse laser deposition, method consists on the use of high-power laser pulses to evaporate material from a target surface, preserving its stoichiometry. The supersonic stream of particles (plume) is guided ordinary to the objective surface. The tuft extends away from the objective with a consistent forward-directed speed dissemination of various particles. The removed species gather on the substrate facing on top of the target. For ZnO growth, tipically UV excimer lasers KrF and ArF and Nd yttrium aluminum garnet YAG pulsed lasers ablate the zinc oxide target in oxygen environment, pure zinc metal is rarely adopted. The properties of the grown ZnO films depend mainly on the substrate temperature, ambient oxygen pressure, and laser intensity.
Other studies reports the possibilitiy to obtain small grains polycrystalline film through deposition of pure zinc metal followed by an annealing step, extremely effective for the

preparation of random lasers.[5]

2.1.1.1 Electronic properties

Main interests for the purpose of the study on ZnO are their electronic features. As aforementioned, it is a wide band gap material with theoretically high breakdown voltage, resistance at large electric field, low generation noise, high temperature and high power operation.

The electronic band structure is relevant to understand the conduction mechanism governing semiconductor. Several studies (based on DFT, LDA) and experimental techniques (X-ray, UV-absorption) has been carried out to analyse the band structure of bulk and thin film zinc oxide, in all the three different phases.No available experimental data on bulk or film layer ZnO but only qualitative analysis. When wurtzite ZnO is compressed and change the, it has been observed that the peak at the top of the upper valence band is slightly reduced in height and shifted down in energy, While transforming to the rock salt structure at the transition pressure p_{T1}, significant changes have been observed, the peak near the valence-band maximum is greatly reduced in height. it has been argued that the key features are a change in nearest-neighbour bond lengths as they affect overlaps and bandwidths and change in symmetry as they affect the orbital hybridization and band repulsion.

The assert the quality of the crystal and the transport mechanism, the mobility of free carriers (electrons in n-type and holes in a p-type semiconductor) is a crucial parameters.

$$\mu = \frac{q\langle\tau\rangle}{m^*}$$

with m^* the electron effective mass in the second order approximation, q the elementary charge and $\langle\tau\rangle$ the relaxation time. The latter entails the rate of change of electron momentum as it scatters in the crystal. Considering various scattering mechanism the total relaxation time may be expressed by $\frac{1}{\langle\tau\rangle} = \sum_i \frac{1}{\tau_i}$, where i denotes the scattering experienced by e^-. The major scattering in bulk or thin film crystalline ZnO are ionized impurity, polar LO-phonon, AO-phonon, piezoelectric, and dislocations or native point defect or crystal imperfection.[5, 8]. Through experimental and mathematical model the zinc oxide bulk mobility is *figure 2.3* as function of temperature and as function of doping concentration due to crystal imperfections in *figure 2.4*

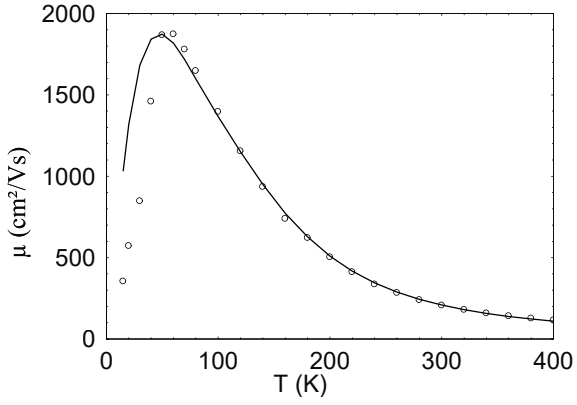

Figure 2.3: Theoretical evaluation and experimental data(•) of mobility vs T[8]

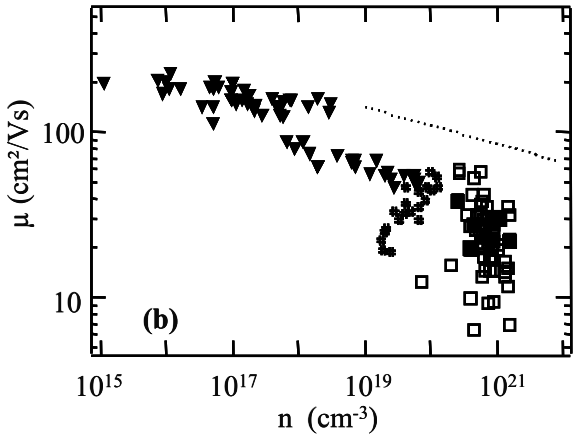

Figure 2.4: Mobility vs donor doping concentrations, ▲ ZnO crystal ■ high impurity thin film deposited trhough Rf magnetron sputtering, □ thin film deposited trhough Rf magnetron sputtering [8]

The peak is at very low temperature around 50 °K, showing a steep decrease at higher temperature, reaming approximately constant above 250 °K, and the measured mobility at different doping concentration remain in agreement with the other result.

Regardless of the shape of the energy band and the occupation energy according to the orbital configuration of zinc oxide, the amount of intrinsic carriers should be extremely low if compared to other low energy gap semiconductor, however this does not happen, and most of the growth technique produces highly n-type samples. The unintentionally doped zinc oxide is still under debate and several suggestions has been carried: the incorporation of external impurities during the growth process, the deviation from a perfect structure due to native point defect in the crystal.

Native point defects represent one of the major cause of the intrinsic carriers concentration (up to even $1 \times 10^{21}\,\mathrm{cm}^{-3}$). According to literature, there are still controversial argument regarding which impurity may cause the alteration of the conductivity. It has been attributed that the oxygen vacancies V_O and zinc interstitial Zn_i are the active shallow donor part, with the latter more dominant over the other potential contribution [9, 10, 11], which are also associated with the peak intensity in the green luminescence band [12]. On the other side, zinc interstitial and anitisites (a Zn atom occupying an O lattice or vice versa), and also oxygen interstitial, Zn_i, Zn_a, O_i, has been asserted as shallow donor for the first two and deep acceptor for the latter, but with relatively high formation energy which is improbably to form in the crystal, therefore it can not be attributed the shaping of n-type behaviour. Zinc vacancies V_{Zn} are deep acceptor which is negligible, a low formation energy under a n-type conditioning analysis, although they could be the real cause of green luminescence as mentioned above [13]. Therefore extrinsic impurities trapped in the crystal has been suggested as the main cause. Among these, the intentionally or unintentionally incorporation of hydrogen is one of the most plausible, indeed most of the technique used to deposit ZnO, or as active material (laser ablation [14], RF sputtering [15] or as part of precursor gas in specific growth mechanism (vapor-phase transport ([16]), chemical vapor deposition [17], hydrothermal growth. Indeed, hydrogen interstitial in the lattice, H_i, may play this role. Indeed, while in most of semiconductor, H_i act as an amphoteric impurity (counteract the dominant type of doping concentration) in zinc oxide it occurs on in a positive charge state, i.e. it only acts as a shallow donor [18, 19]. It has also been found that substitutional hydrogen

may also replace oxygen in one of the site in the wurtzite structure, forming a multicenter bond where one hydrogen atom is bonded to he four nearest zinc atoms, within which it act again as a shallow donor. Both of this impurities have low formation in ZnO crystal, which means that the possibility of high concentrations is significant.
Anyhow, it is possible to dope zinc oxide with other atom, like group III B, Ga, Al [20], but also Ti [21, 22]. Nevertheless the n-type state of zinc oxide is well stable and reproducible, making out a p-type zinc oxide is a real challenge. This difficulty may arise from different causes. The first is the presence of all the native imperfections as discussed previously that will screen the effect of extrinsic impurities that may be shallow acceptor. Low solubility of dopant in the crystal maybe a detrimental effect. Deep impurity level may counteract the effect of shallow acceptor state. Anyhow, the general known acceptor impurities are N, [23, 24], Li, Na, K (group I element), but also Cu [25] or Ag [26, 27].

2.1.1.2 Optical properties

The optical properties of a semiconductor are connected with both intrinsic and extrinsic effects. Firstly zinc oxide is direct semiconductor, that is when the valence band peak is in correspondence of the conduction band minimum in the reciprocal lattice, therefore the recombination of electron form CB to VB does not require an intermediate state (associated with a phonon creation) but experiences a direct transition. This would enable the possibility of creating high efficient LED, however the complexity arising from the formation of a p-type zinc oxide layer limit drastically the of this WBG in this application. These peculiar aspect may be extracted through intrinsic and extrinsic optical transition. This phenomenon is related to the correlation of the electrons in the conduction band and holes in the valence band, including excitonic impacts to Coulomb interaction. Excitons are grouped into free and bound excitons. In high-purity samples, the free exciton can likewise show energized states, notwithstanding their ground-state changes. Extrinsic properties are connected with dopants or native defects, which normally make discrete electronic states in the band gap, and accordingly impact both optical-absorption and emission. The electronic conditions of the bound excitons (BEs) rely unequivocally upon the semiconductor material, specifically, the band structure. In principle, excitons could be bound to impartial or charged donor and excepts. Undoped and doped ZnO shows also a large exciton binding energy even at RT, which inhibits thermal activation and enhance light emission, is due to the free exciton (transitions from the conduction band to three valence bands denoted as the heavy hole, the light hole also referred to as crystal-field split band)[28], while yellow or green photoluminescence peak are due to the dopants or defects, which usually create discrete electronic states in the band gap [5].

2.1.1.3 Schottky and Ohmic contact

The intentionally undoped zinc oxide material will have consequences on the different type of material built around them. Due to infeasibility of creation of a p-n homojunction, several analytical and experimental studies have been performed on the effect of metal-semiconductor interaction. Due to the peculiarity of this WBG the fabricated layer were undergone different treatment to develop reliable rectifying contacts. Firstly, different deposition technique has been exploited, as already discusse above, the crystal quality is extremely random, combined also with surface treatment before and after metalization. *Table 2.1*, *2.2* reports a table of

summary over time of the resulting schottky barrier Φ_{sb} behaviour, whereas *figure 2.3* reports a table of summary over time of the analysed ohmic contact behaviour.

Metal	$qU_{SB}{}^{n}$(eV)	Ideality Factor	Surface Treatment	Measurement Technique	Ref.
Pt (5.65)	0.75 nonpolar	—	Vac- cleave	IPS	23
Pt	0.42 (000$\bar{1}$)	3.45	HD, ROP1A	I-V	40
Pt	ohmic (000$\bar{1}$)	NA	LD, ATMA	I-V	40
Pt	0.39 (000$\bar{1}$)	1.00	LD, ROP1A	I-V	40
Pt	0.61 (0001)	1.70	PLD, AG	I-V	45
Pt	0.85, 0.73 (0001)	1.77	ATMA, LA	C-V, I-V	46
Pt	0.6 (0001)	3.1	OCA	I-V	47
Pt	0.70 (0001)	1.5	UVOA	I-V	53
Pt	0.93, 0.89 (0001)	1.15	HPA	C-V, I-V	56
Pt	0.55 (0001)	2.0	CCA	I-V	57
Pt	0.72, 0.68 (000$\bar{1}$)	1.2	CCA	C-V, I-V	57
PtO_x	1.20 (0001)	1.005–1.045	PLD, OCA	I-V	66
PtO_x	0.98 (000$\bar{1}$)	1.005–1.025	PLD, OCA	I-V	66
Ir (5.27)	0.65 (000$\bar{1}$)	2.62	HD, ROP1A	I-V	40
Ir	0.69 (000$\bar{1}$)	1.58	HD, ROP1A	I-V	38
Ir	0.54 (000$\bar{1}$)	1.66	LD, ATMA	I-V	40
Ir	0.64 (000$\bar{1}$)	1.36	LD, ROP1A	I-V	38
IrO_x	1.14 (0001)	1.01–1.03	PLD, OCA	I-V	66
IrO_x	0.88 (000$\bar{1}$)	1.005–1.03	PLD, OCA	I-V	66
Pd (5.12)	0.68 nonpolar	—	Vac- cleave	IPS	23
Pd	0.59,0.61,0.60	—	Acid etch	IPS, C-V, I-V	36
Pd	0.73, 0.53 (0001)	1.3	ROP2	C-V, I-V	31
Pd	0.68, 0.61 (000$\bar{1}$)	1.2	ROP2	C-V, I-V	31
Pd	1.14, 0.81 (0001)	1.49	PLD, AG	C-V, I-V	48
Pd	0.74 (0006 1)	2.0	Acetone, Acid etch	I-V	49
	0.60 (0006 1)	1.4		I-V	
Pd	0.83 (000$\bar{1}$)	1.03	HPA	I-V	50
Pd	1–1.2 (000$\bar{1}$)	1.8	HPA	C-V, I-V	52
Pd	0.55 (0001)	2.0	CCA	I-V	57
Pd	0.59, 0.59 (000$\bar{1}$)	1.2	CCA	I-V, C-V	57
Pd	0.6 (000$\bar{1}$)	1.6–2.1	HPA	I-V	61
PdO_x	1.10 (0001)	1.007–1.034	PLD, OCA	I-V	66
PdO_x	0.89 ((000$\bar{1}$)	1.018–1.035	PLD, OCA	I-V	66
Au (5.1)	0.65 nonpolar	—	Vac- cleave	IPS	23
Au	0.645,0.67,0.66 -	—	CCA	IPS, C-V, I-V	36
Au	0.67,0.60 (000$\bar{1}$)	1.86, 1.03	ROPHT,ROPRT	I-V	37
Au	0.71 (0001)	1.17	ROPHT,ROPRT	I-V	55
Au	ohmic (0001)	NA	LD, ATMA	I-V	23
Au	1.2, 0.81 (0001)	1.2	LD, ROP2	C-V, I-V	31
Au	1.07, 0.77 (000$\bar{1}$)	1.3	LD, ROP2	C-V, I-V	31
Au	0.48 (000$\bar{1}$)	1.30	LD, ROP1A	I-V	38
Au	ohmic (000$\bar{1}$)	NA	LD, ROP1, 650 C	I-V	39
Au	0.43 (000$\bar{1}$)	3.57	HD, ROP1A	I-V	38
Au	0.46 (000$\bar{1}$)	1.56	LD, ATMA	I-V	38
Au	0.48 (000$\bar{1}$)	1.30	LD, ROP1A	I-V	40
Au	Ohmic (0001)	NA	ATMA	MG, I-V	41
Au	0.63 (0001)	1.15	HPA	MG, I-V	41
Au	0.65 (0001)	—	ATMA	C-V	42
Au	0.66 (0001) ZnO:N	1.8	OCA	I-V	44
Au	0.37 (000$\bar{1}$) ZnO:N	3.5	OCA	I-V	44
Au	0.71, 0.70 (0001)	1.4	CCA	I-V, C-V	57
Au	0.70, 0.69 (000$\bar{1}$)	1.1	CCA	C-V, I-V	57
Au	0.61 (0001)	1.82	CVD, HPA	I-V	67
PEDOT:PSS(5.0)	0.9, 0.7 (0001)	1.2	HT, CCA	I-V, C-V	60
PEDOT:PSS	1.1 (0001)	1.02	HT, CCA	I-V, C-V	64
PEDOT:PSS	1.03–0.88 (000$\bar{1}$)	1.3–1.6	HT, CCA	I-V, C-V	65
Ti (4.33)	<0.3 nonpolar	—	Vac- cleave	I-V	23
Ti	ohmic (0001)	NA	OCA	I-V	53
Cu (4.65)	0.45 nonpolar	—	Vac- cleave	I-V	23
Al (4.28)	0.0 nonpolar	—	Vac- cleave	I-V	23

Table 2.1: Φ_{SB}, schottky barrier measurements by various techniques versus orientation and crystal quality for metals on ZnO surfaces prepared by different cleaning methods [29]

Metal	U_{SB}^{n}(eV)	Ideality Factor	Surface Treatment	Measurement Technique	Ref.
Ag (4.26)	0.68 nonpolar	—	Vac- cleave	IPS	23
Ag	0.92,0.89(1120)	1.33	AG	C-V, I-V	43
Ag	0.69 (0001)	—	ATMA	C-V	42
Ag	0.84 (1120)	1.5	O_2 plasma	I-V	54
Ag	0.80, 0.78 (0001)	1.2	CCA	C-V, I-V	57
Ag	1.11, 1.08 (0001)	1.08	CCA highest	I-V, C-V	58
Ag	0.80, 0.77 (000$\bar{1}$)	1.1	CCA	C-V, I-V	57
Ag	0.99, 0.97 (000$\bar{1}$)	1.06	CCA highest	I-V, C-V	58
Ag	1.0	1.6–3	PLD, H_3PO_4	I-V	68
Ag oxide (5.0)	1.20, 0.93 (0001)	1.03	HT, OCA, OPS	I-V, C-V	59
Ag oxide	0.99, 0.79 (000$\bar{1}$)	1.04	HT, OCA, OPS	I-V, C-V	59
Ag oxide	1.03 (0001)	1.14	MG, OCA,OPS	I-V	59
Ag oxide	0.98, 0.89 (000$\bar{1}$)	1.10	MG, OCA,OPS	I-V, C-V	59
Ag oxide	1.02 M-plane	1.10	MG, OCA,OPS	I-V	59
Ta (4.25)	ohmic (000$\bar{1}$)	NA	ROP 1A	I-V	39
Ta	blocking (000$\bar{1}$)	NA	LD,ROP 1A, 350 C	I-V	39
Ta	blocking (000$\bar{1}$)	NA	LD, ROP 1A, 550 C	I-V	39
Ta	ohmic (000$\bar{1}$)	NA	HD, ROP 1A	I-V	39
	Leaky (000$\bar{1}$)	NA	HD, ROP 1A, 550 C	I-V	39
In (4.12)	<0.3 nonpolar	—	Vac- cleave	I-V	23

[a] The metal column includes the corresponding work function (Ref. 69).

Table 2.2: *table 2.1* (Continued.)[29]

Metal Scheme	ZnO Carrier Concentration (cm^{-3})	Annealing Condition	Resistance (Ω-cm^2)	Ref.
In	(n)	Nonalloyed	7×10^{-1}	112
Ti/Au	2×10^{17} (n)	Nonalloyed	4.3×10^{-5}	113
Al/Au	1×10^{17} (n)	Nonalloyed	2.5×10^{-5}	118
Al/Au	3×10^{17} (n)	200 C/N_2/1 min	1.4×10^{-4}	131
Al/Pt	2×10^{18} (n)	Nonalloyed	1.5×10^{-5}	119
Al/Pt	(n)	Nonalloyed on ZnO Nanorods	1.2×10^{-5}	127
Ag, In, Sn	(n)	Nonalloyed on ZnO Nanorods	$1–6 \times 10^{-3}$	128
Ti/Au	2×10^{17} (n)	300 C/N_2/1 min	2×10^{-4}	110, 104
Ti/Al	1.7×10^{18} (n)	300 C/N_2/1 min	9.7×10^{-7}	132
Ta/Au	1×10^{17} (n)	300 C/N_2/30 sec	5.4×10^{-6}	133
Ti/Al/Au	(n)	non-alloyed	4.1×10^{-5}	114
Ti/Al/Pt/Au	(n)	non-alloyed	4.2×10^{-5}	114
Ti/Au	(n)	non-alloyed	4.2×10^{-5}	114
Ti/Pt/Au	(n)	non-alloyed	4.8×10^{-5}	114
Ti/Au	(n)	non-alloyed	3.0×10^{-4}	38
Ti/Au	1.9×10^{19} (n)	non-alloyed	2.4×10^{-7}	107
Ti/Au	1.9×10^{19} (n)	300 C/O_2/1 min	6×10^{-8}	107
Re/Ti/Au	2×10^{18} (n)	700 C/N_2/1 min	1.7×10^{-7}	136
Pt-Ga	(n)	non-alloyed	3.4×10^{-4}	108
Ti-Au	3×10^{18} (n)	non-alloyed	1.5×10^{-5}	109
Ru	3×10^{18} (n)	700 C/N_2/1 min	3.2×10^{-5}	129
Ni/Au	1.00×10^{18} (p)	600 C / N_2/1 min	1.72×10^{-4}	144
Au	1.42×10^{16} (p)	520 C/N_2/2min	3.15×10^{-3}	140
Ni/Au,Ti/Au,In/Au	4.00×10^{17} (p)	600 C/N_2/10 sec	2.70×10^{-4}	141
In/Zn	6×10^{17} (p)	550 C/Ar/2 min	2.4×10^{-6}	143
Pt/Ni/Au	5×10^{17} (p)	600 C/N_2/1 min	1.97×10^{-5}	151
Ni/Au	1.00×10^{16} (p)	600 C/air/1 min	2.50×10^{-5}	155, 142
Au/Ni/Au	1.00×10^{16} (p)	600 C/air/1 min	7.60×10^{-6}	155,142
Ni/Au	1.00×10^{19} (p)	800 C/N_2/60 sec	3.00×10^{-4}	152
Ni/Pt	8.00×10^{16} (p)	450 C/N_2/30–90 sec	3.81×10^{-6}	145
Ni/Pt	1.00×10^{17} (p)	550 C/N_2/60 sec	1.03×10^{-4}	146
Ni/Au	8.00×10^{16} (p)	450 C/N_2/60 sec	2.06×10^{-4}	147
Ni/Au	(p)	300 C/N_2/60 sec	5.2×10^{-4}	148

Table 2.3: Ohmic contacts to ZnO formed by various metallization schemes [29]

The extreme inconsistent in the results lay on various complex aspect. The electronic effect of crystal defects and impurities, morphology of the surface of ZnO film, polarity effects

(Zn-polar o O-polar), chemical effect such as metal dependence of interface chemistry, interface chemistry and defect formation caused by surface treatments; for a intense and exhaustive analysis please refer to [29].

2.1.2 Silicon Carbide (SiC)

The building piece of silicon carbide shows a tetrahedron structure, where a silicon/carbon atom bonds to four carbon/silicon atom, respectively. SiC is a polymorphic binary compound which exists in at least 250 polytypes according to their crystal structure, among them the more known and stable are the alpha (α-SiC) and beta (β-SiC) form. The first one has an hexagonal structure (similar to wurtzite), in the possible configuration of 4H-SiC and 6H-SiC, the latter instead a zinc blende crystal structure (similar to diamond) 3C-SiC, as shown in *figure 2.5*.
The 3C-SiC has a cubic unit cell in the form of ABC (where each letter indicates the different configurations of the simple tetrahedron structure), whereas 4H-SiC has ABCB unit cell, and 6H-SiC an ABCABC one[30].

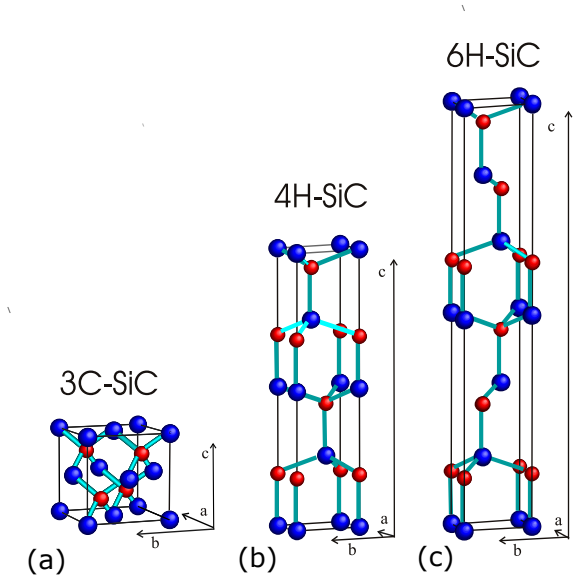

Figure 2.5: (a) cubic zinc-blende, (b) 4H hexagonal (c) 6H hexagonal. Blue and red ball representing Si and C respectively. [31]

As for ZnO, silicon carbide can be grown with different mechanism, starting from pure SiC ingot to homo-hetero epitaxial growth on selective substrate and in polycrystalline thin film via CVD or PECVD.

Material Parameters	4H-SiC	6H-SiC	3C-SiC	Si
Energy bandgag @ RT [eV]	3.27	3.03	2.3	1.12
Lattice constant @ RT [Å]	3.076	3.081	4.349	3.84
Breakdown electric field [MV/cm]	2.2	2.5	2	0.25
Saturated electron velocity [10^7cm/s]	2	2	2.5	1
Thermal conductivity [W/mK]	$300-380$	$300-380$	$300-400$	150
Intrinsic carrier concentration [cm^{-3}]	$\sim 10^{-7}$	$\sim 10^{-5}$	~ 10	$\sim 10^{10}$
Electron mobility at $N_D = 10^{16}$ [$cm^2/V\,s$] ($\parallel$ c-axis)	900	60	750	1400

Table 2.4: Comparison of Si vs SiC polytypes [32]

As reported in *table 2.4*, α phase has a larger band gap with respect to the β phase, making it more suitable for UV photodetection, for its intrinsic cutoff wavelength. Between these two, 4H-SiC polytypes has gained much more attention in different application fields in the meantime thanks to its improved electronic properties [33].

2.1.2.1 Electronic properties

The electronic band structure of 4H-SiC is shown in *figure* **??**. The valence band maximum and conduction band minimum are not located in the same point in BZ, due to the indirect band gap of SiC, as expected.

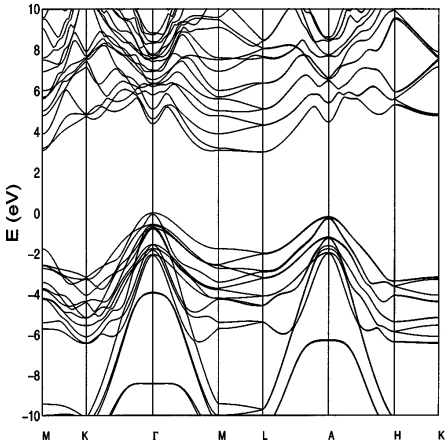

Figure 2.6: Band structure of bulk 4H-SiC in n-type condition through the adoption of empirical pseudo potential EPM [34]

As already outlined in *table 2.4*, the higher energy band gap, saturated electron velocity, as well as lowest intrinsic carrier concentrations of 4H-SiC among all silicon based semiconductor make it extremely effective and useful. Moreover, the relatively high thermal conductivity at RT, allow the use of 4H phase high temperature condition (500-900 °K) where thermal activation carriers may remain negligible [35]. Despite of the presence of intrinsic defects in

the crystal [], extrinsic impurities dope SiC both in a negative and positive type. Generally,a shallow donor is N and a shallow acceptor is Al. Obtaining both p- and n-type material smoothed the path of fabricating devices for lot of application such as p-n diode (also schottky diode), p-i-n , avalanche photodiode, MOSFET , BJT [36, 37]. Furthermore, having higher electron and hole mobility with respect to the other common polytypes justify even more the adoption of 4H-SiC for faster response speed and low parasitic resistances which traduces in low power dissipation. (*figure 2.7a* and *2.7b*)

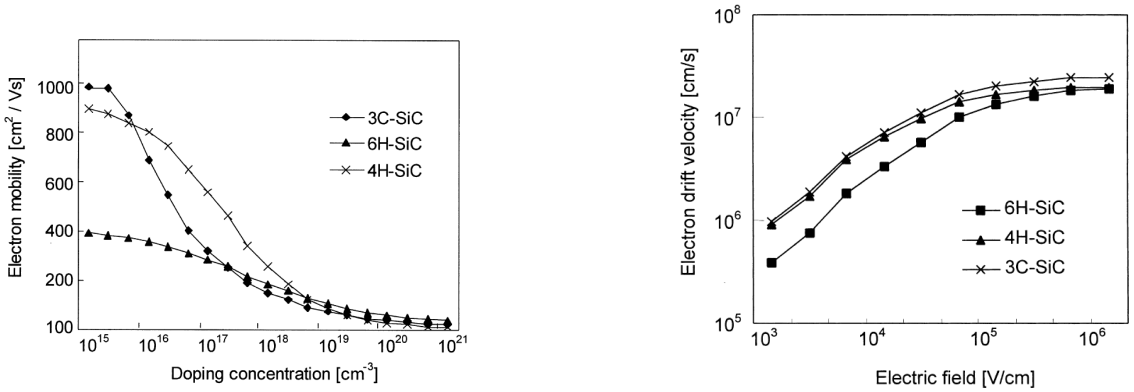

(a) Electron mobility vs doping level concentration

(b) Electron drift velocity vs applied electric field

Figure 2.7: Electronic characteristic of various SiC polytypes [38]

Although the aforementioned indirect band gap, above the UV spectrum, bulk and crystalline thin film 4H-SiC show nonlinear absorption coefficient and nonlinear refractive index coefficient in the VIS and NIR region, characterized by nonlinear two-photon(2PA) and three-photon absorption (3PA) coefficient, which reveal the potential of SiC for ultra-fast all-optical switching [39].

2.2 Photodetector

Photodetectors, PD's, is class of sensors which is able to convert light into another type of signal. They are classified depending on the kind of mechanism involved in the detection.

- Photons cause electrons to transition to mid-gap states then decay back to lower bands, inducing phonon generation and thus internal heat (bolometer, thermocouple and Pyroelectrict)
- Photoemission or photoelectric effect
- A change in the indices of refraction or other polarization effects can result from photon-induced changes in the polarization states of appropriate materials.
- Photons cause a chemical change in specific materials
- Secondary effects caused by photons include changes in gas pressure in Golay cells or photon drag detectors.

The above listed mechanism can be grouped in two main category, thermal and electrical, as shown in *figure 2.12*.

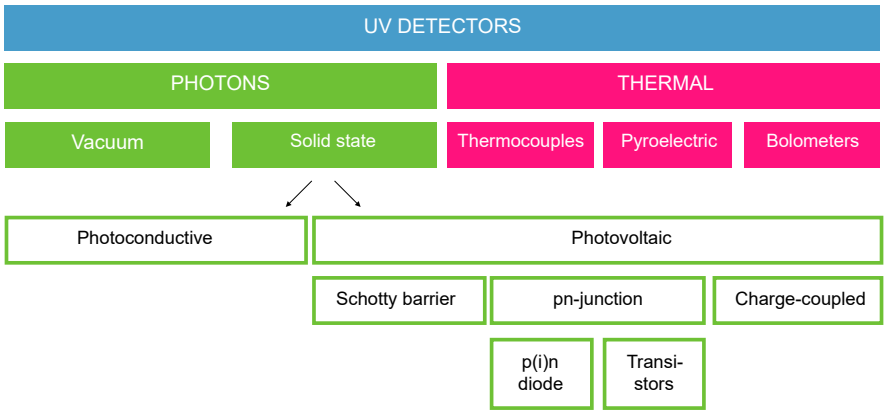

Figure 2.8: Diagram of PD categories

The type of mechanism that we are going to discuss, relevant to our purpose, consists on the conversion of optical signal into an electrical response. PD's based on semiconductor devices is a subcategory among all of this type of sensors, and they represent the most widely adopted devices in this field.
The reason is fairly simple, these PD's have low sizes and are lightweight. They have a general high response speed, relatively high detection efficiency, and well defined selectivity in light response (wavelength dependent).
In a simplified way, the physical process at the principle of detection, takes place when a photon with a sufficient energy impinges the surface of a semiconductor crystal will be eventually absorbed generating an electron-hole pair. This pair consists on a electron that leave an energy state to reach another one where it is entirely free to move along the crystal region an at the same time it leaves a vacancy in the original energy state, called hole, which can also move in the crystal. In the absence of any external electric field, the active generated carriers may recombined to their low energy state giving rise to other process, such as radiative recombination that generates a photon, or non-radiative recombination like an induce crystal thermal heat with the involvement of a phonon, or either an acoustical vibration in the crystal. On the other side, when an electric field is applied, a current will flow across the devices, whose response is dependent on the impinging photons a schematic is given in *figure 2.9*

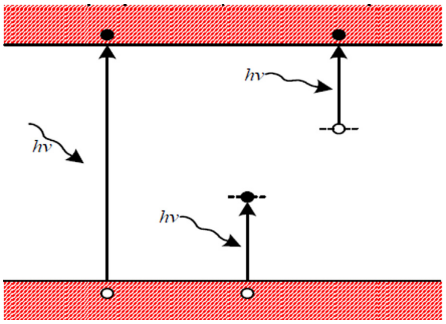

Figure 2.9: Representation of a photon absorbed by the crystal, donor and acceptor trap state laying in between the energy gap of the semiconductor [1]

A list of the most relevant feature of photodetectors is provided:

- **Cutoff wavelength**:
  It is closely related to the Nagy gap of a semiconductor, indeed an effective response can be detected only if the energy allow the electron to jump out the valence band to the conduction band (creation of an a e^-/h^+ pair) that is: E_{ph} ¿, E_g, i.e. $\frac{hc}{\lambda}$ ¿, E_g. The cutoff edge is thus defined as the longest wavelength with the lowest photon energy absorbed by a specific semiconductor: $\lambda_c = \frac{hc}{E_g} = \frac{1.24\,\mathrm{eV}}{E_g}$. where h, c, λ and λ_c are the Planck constant, light speed, incident light wavelength and cutoff wavelength. However, sometimes a photoresponse with photon energies lower than E_g may be perceived, known as the sub-band response, which is the response from carrier transitions relating to defect levels or band tails introduced by intrinsic defects or imperfections []

- **Responsivity**($\mathcal{R}$):
  it is defined as the ratio of photocurrent generated by unit illumination power at a specific wavelength:
  $$\mathcal{R}(\lambda) = \frac{I_{ph}(\lambda)}{P_{opt}(\lambda)} = \frac{I(\lambda) - I_{dark}}{P_{opt}(\lambda)} \tag{2.2}$$
  where $\mathcal{R}$, I_{ph}, I, I_{dark} and P_{opt} are responsivity, photocurrent, total current, dark current and illumination power, respectively. This parameter is correlate to the internal quantum efficiency of the PD, that is the effective ratio of generate pair with respect to the number of photon absorbed, and it entail the device performances:
  $$\mu_{int} = \frac{I_{ph}(\lambda)}{q}\Phi(\lambda) = \frac{I_{ph}(\lambda)\,hc}{q\lambda P_{opt}(\lambda)} = \frac{\mathcal{R}(\lambda)\,ch}{q\lambda}$$
  where $\Phi(\lambda)$ is the photon flux.

- **Response time**
  It represents the capability of a PD' to reach a stable signal under exposure or not, which restricts the maximum bandwidth of the total circuits. it is the time required for the photocurrent to decrease from its maximum to 10% (or increase from dark to 90%).

- **NEP**:
  It expresses the minimum detectable power per square root bandwidth of a given detector, that is, the weakest optical signal detectable by the device. The NEP is generally measured output power in 1 Hz bandwidth, at which the S/N ratio is equal to one.

- **Detectivity (D^*)**: It is a parameter in direct correlation to the NEP and is used in cases when the noise scales as the square root of the area, such as shot or flicker noise. the mathetical expression is $D^* = \frac{\sqrt{A_{opt}BW}}{NEP(\lambda)}$, where A_{opt} ids the effective optical area of the device.

- **S/N (signal to noise ratio)(or Gain)**
  it is intuitively expressed by the ratio of UV-to-dark responsivity of a semiconductor PD, namely the rejection ratio. i.e. $G = \frac{Iph}{I_{Dark}}$

depending on the type of structure that is adopted, it exists various typologies of semiconductor base photodetector.

2.2.1 Photodiode

The photodiode is a particular king of diode sensitive to a specific spectrum of electromagnetic wave. A diode comes out from the junction between a n-type and a p-type semiconductor (they may be of the same material, or different material called homojunction or heterojunction respectively), schematic in *figure 2.10b*. The contact between the opposite semiconductor induce a charge diffusion, form region with high concentration to regions with lower concentration, in order to reach an equilibrium condition. This result in a depletion area, named also space charge region (SCR), arises form the ionized dopants where a built-in electric field directed from the n-towards the p-junction, whereas the remaining part of the semiconductor are called quasi neutral region (QNR). A potential barrier between the two sides, will cause, then, a blockage of charge transfer. The energy band diagram, of an homojunction, obtained through Poisson equation across the whole region is depicted in *figure 2.10a*.

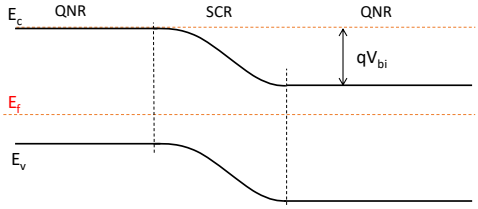

(a) Band diagram in normal condition

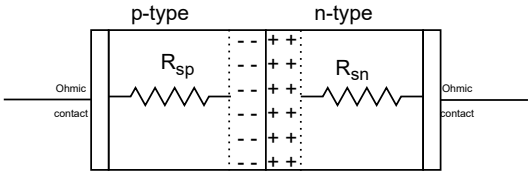

(b) Block diagram of a p-n junction

Figure 2.10

Applying an external voltage, V_A, we may represent the voltage across the diode as felt only along the space charge region, by a direct change in the behaviour of the device, where the energy band diagram experience the following change in *figure 2.11b* and *2.11a*.

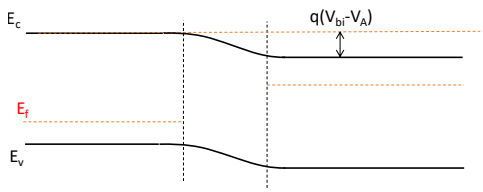

(a) Band bending under a positive applied voltage V_A

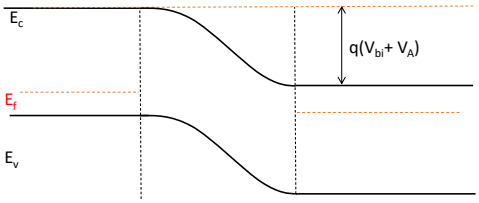

(b) Band bending under a negative voltage V_A

Figure 2.11

Where the width of the depleted region is modulated according to:

$$w_{DR} = \sqrt{\frac{2\epsilon_r(V_{bi}) + V_A}{q}\left(\frac{N_A + N_D}{N_A N_D}\right)}$$

where N_A and N_D are the doping concentration, ϵ_r the dielectric constant of the material, q the elementary charge. According to a drift-diffusion model and neglecting recombination effect cause by defect (Shockley-Read-Hall model or Auger mechanism, radiative recombination), we may express the current flowing across the device as follow.

$$I = AJ_R\left(e^{\left(\frac{V}{nV_t} - IR_s\right)} - 1\right)$$

where A is the effective area of the device, J_R is the current density under reverse condition, V_t is the thermal voltage (V_t=$\frac{k_b T}{q}$ with T tmeprature in kelvin, K_b the boltzman constant), R_s is the series resistance of the quasi neutral region and n is the ideality factor which entails non radiative recombination mechanism happening in the device (such band to band (low level injection) shockley-read-hall (SRH) or SRH, band to band (high level injection) or even Auger mechanism). The reverse current is defined as follow:

$$J_R = \frac{qD_p p_{no}}{L_p} + \frac{qD_n n_{po}}{L_n}$$

where D_n and D_p are the oping diffusion intensity, n_{p0} and p_{n0} are the minority carrier concentration are evaluated at the border between the QNR And SCR, and L_p ($L_p = \sqrt{D_p \tau_p}$) and L_n ($L_n = \sqrt{D_n \tau_n}$) are the diffusion length and lifetime of electrons and holes in the material.
A electrical model of the device, without taking into account noise sources, is given in *figure B.1*:

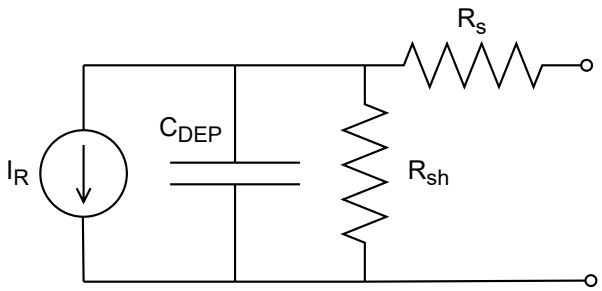

Figure 2.12: Equivalent circuit

Where the parallel capacitance is due to the depletion and diffusion capacitance of the diode , namely C_{DEP} and C_{DIFF}, but generllay $C_{DEP} \gg C_{DIFF}$, therefore we can state that parameter is only given by the SCR, which is:

$$C_{DEP} = \epsilon_r \frac{A}{w_{DR}} = A\sqrt{\frac{\epsilon_r q}{2\epsilon_r(V_{bi}+V_A)}\left(\frac{N_A N_D}{N_A+N_D}\right)}$$

R_s the series resistance is :

$$R_s = \frac{1}{q\mu_n N_D}\frac{L_{nD} - w_{DRn}}{A} + \frac{1}{q\mu_h N_A}\frac{L_{pA} - w_{DRp}}{A} \tag{2.3}$$

with μ_n and μ_h mobility of electrons and holes respectively, and L_{nD}, w_{DRn}, L_{pA}, L_{DRp} are the length of the semiconductor and width of the depleted region in the n and p side respectively. The parallel resistance is the shunt resistance R_{sh} and It is evaluated by taking the slope of the I-V curve of the diode at zero bias condition: $R_{sh} = \left(\frac{\partial I}{\partial V}\right)^{-1}\Big|_{V=0}$.
When the device is exposed to light,in case of high injection condition, it may absorb it(depending on the absorption coefficient). If the diode is properly biased, the arises generated carriers in the SCR (in the quasi neutral region the photogeneration is almost negligible or will have a low effect since it will be subjected to recombination) will be split by the internal electric field increasing the reverse current. By engineering this simple detector, an higher efficiency may be achieved.

2.2.1.1 p-i-n diode

By properly forming a intrinsic layer in between the n and p-side on the junction, a pin diodes can be created,a shown in *figure 2.13* By increasing the depleted layer, we have an higher absorption as well as an higher effective area where carriers are generated. The advantage of this solution are low noise, low dark current, low bias voltage, higher reverse breakdown voltage, high-speed response, lower depletion capacitance (inversely proportional to the depleted area), however less sensitivity, slower response time, high reverse recovery time due to power loss are significant have a down side in the device performance.

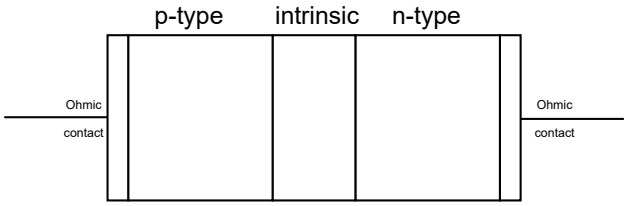

Figure 2.13: Block diagram of a pin junction

2.2.1.2 Avalanche photodiode

An avalanche photodiode (APD) present a slightly different structure with respect to a pin diode. A thin layer of p-type material is added in the conventional pin junction between the intrinsic and the n-type layers, resulting in a maximum of the electric field at the junction of the p and n+ type regions, as illustrated in *figure 2.14*. A reverse bias voltage near the breakdown voltage of the junction is applied, causing a high electric field close to the junction breakdown enabling impact ionization [40], a scenario usually avoided in normal photodiode operations

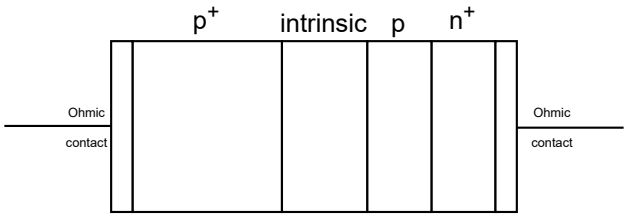

Figure 2.14: Block diagram of a APD, where the + symbol denote a heavily doped semiconductor

The operation principle of the APDs is different from the previously discussed photodiodes as a photon results into a cascade of moving carrier pairs. When a photon is absorbed, the generated e-h pair accelerates in the high electric field, gaining that high kinetic energy that they ionize the crystal lattice. The result of impact ionization is new e-h pairs able to be accelerated and further ionize the lattice repeating the process. The avalanche process gives some additional advantages to avalenche photodiode when compared with the pin or p-n junctions[41]. The resulting features are a greater level of sensitivity, high performance, fast response time, whereas the drawbacks are higher operating voltage required (the device has to work under reverse bias condition), higher level of noise, higher dark current.

2.2.2 MSM structures

The MSM consists on the junction metal-semiconductor-metal which depending on the type of contact between the semiconductor and the metal will be rectifying or not, according to Shockley theory. We are going to describe one by one all the known possibilities. whereas in a p-n diode the conduction mechanism is fully described by minority carriers, in case of MSM there are several transport mechanisms:

1. Thermionic emission (TE) of carriers over the top of the barrier;
2. Field emission (FE) i.e., carriers tunnel through across the full barrier width (preferred by ohmic contacts)
3. Carrier recombination in the depletion region, i.e., hopping transport through defect levels in the bandgap;
4. Thermionic field emission (TFE), i.e., carriers tunnel through near the top of the barrier

A schematic representation of the horizontal structure is in *figure 2.15*:

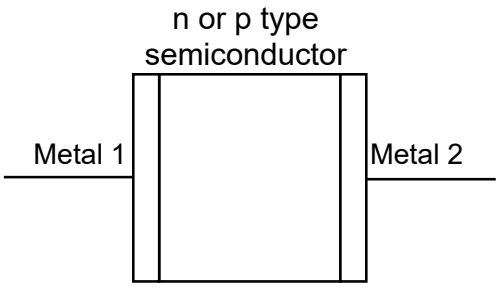

Figure 2.15: Block diagram of a MSM structure

According to schokley theory, depending if the semiconductor is an n- or p-type we have different possible configuration

Semiconductor Type	Schottky	Ohmic
n-type	$\Phi_M > \Phi_{SC}$	$\Phi_M < \Phi_{SC}$
p-type	$\Phi_M < \Phi_{SC}$	$\Phi_M > \Phi_{SC}$

Table 2.5: Φ_M is the metal work function and Φ_{SC} is the semiconductor work function

2.2.2.1 Double ohmic contact

When both metal does not show any rectifying behaviour, the device is a simple photoresistor. The characteristic electrical property is the contact resistivity ρ_c:

$$\rho_c = \left(\frac{\partial J}{\partial V}\right)\Bigg|_{V=0}$$

or

$$\rho_c = \lim_{A_c \to 0} R_c A_c$$

where R_c is the total contact resistance and A_c is the contact area. [29]. The preferred current transport that shows up this device is the field emission (FE) mechanism, since the formed depleted layer is thin enough carrier may tunnel through it. The resistance of the MSM structure may be formulated then a:

$$R = \frac{1}{q\left(\mu_n n + \mu_p p\right)} \frac{L}{A}$$

where n and p are the level of electrons and holes in the material, and L the spacing between the metal. In case of an extrinsic semiconductor , one of the two term will be dominant and the equation can be approximated. When the photoresistor is exposed to specific light, considering a full absorption, in case of an high injection condition $\Delta n_{ph} \gg n$ and $\Delta p_{ph} \gg p$,the carriers generated will be drift away by the external applied electric field, measuring the effective change of the resistance of the film. The photoconductive gain will then be:

$$G = \left(\mu_n n_{ph} + \mu_p p_{ph}\right) \frac{\tau V_A}{L^2} = \frac{\tau}{t_n + t_p}$$

where τ is the average carrier lifetime, $t_n = \frac{L^2}{V_A \mu_n}$ and $t_p = \frac{L^2}{V_A \mu_p}$, the transit time of electrons and holes from metal one to metal two.

2.2.2.2 Schottky-Ohmic contact

When one of the two metal reproduce a schottky contact, a depletion is formed at the interface between that metal and the semiconductor, where the carriers flow is mostly dominated by the aforementioned detailed mechanism. The same discussion as for the photodiode may be applied. However, due to the effect arising from interfaces between to different kind of material, the contact may be partially different from the ideal case. We have the energy band diagrams reported in *figure 2.16a* , where in *figure* we have the ideal case and in *figure* **??** interface effect such as surface state in narrow energy ranee that lay in the energy gap, whcih act as trapped centre for carriers.

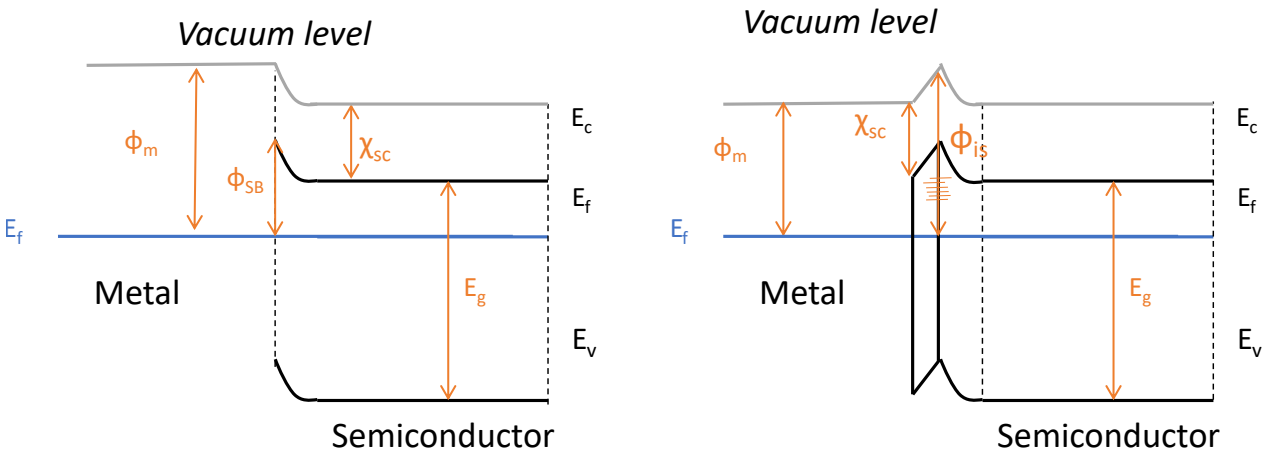

(a) Band diagram under normal condition in an ideal case

(b) Band diagram with surface state

Figure 2.16: [42]

The schottky barrier, $q\Phi_{SB}$ in the ideal case will be:

$$q\Phi^n_{SB} = q\Phi_M - \chi_{SC} \quad \text{and} \quad q\Phi^p_{SB} = E_g + \chi_{SC} - q\Phi_M$$

where $q\Phi^n_{SB}$ and $q\Phi^p_{SB}$ the SB heights for electron and hole injection, $q\Phi_M$ is the metal work function, χ_{SC} is the electron affinity. In the other situation the schottky barrier may be expressed by :

$$q\Phi^n_{SB} = Sq\Phi_M - \chi_{SC} + (1 - S)\,\Phi_{IS} \tag{2.4}$$

and Φ_{IS} is the interface dipole, with the schottky pinning factor $S = \dfrac{\partial\Phi^n_{SB}}{\partial\Phi_M}$ (a similar expression can be derived for a p-type device).In this case the ideality factor is related mostly to the schottky contact: $\frac{1}{n} = 1 \pm \frac{\partial\Phi_{SB}}{\partial qV}$ Anyway the current is expressed as:

$$I = AJ_{R-SC}\left(e^{\left(\frac{V}{nV_t} - IR_s\right)} - 1\right) \tag{2.5}$$

where this time J_{R-SC}, and R_s is only is set out by the semiconductor:

$$J_{R-SC} = AA^*T^2e^{-\dfrac{\Phi_{SB}}{V_t}}$$

where AA^* is the Richardson constant. The main features as PD, if compared to a diode, are High efficiency, Fast recovery time so it can be mostly used in the application of high-speed switching, Low junction capacitance, The low forward voltage drop, It can operate high frequency, Schottky diode produces less unwanted noise than common diode, High current density, Low power consumption. Rapid response to a change in bias, It has a negligible storage time, Low switching time, while more expensive. operate at low voltages compare to the P-N junction diode, These diodes can't withstand much higher voltage without break down, These diodes have relatively higher reverse current, It gets heated up quickly in practical.

2.2.2.3 Double schottky contact

When both metal does not show any rectifying behaviour, the device is a simple shows a non linear I-V behaviour, resulting an asymmetrical behaviour if the metal are different. The *figure 2.17* report a symbolic reperesentation representation.

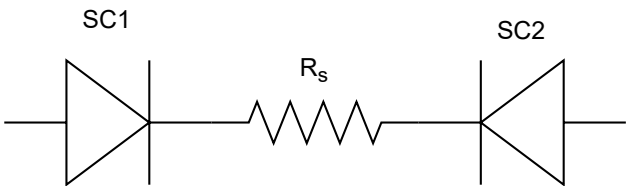

Figure 2.17: Block diagram of a a double schottky structure [43]

The *figure 2.18* reports a schematic of the energy bands, (neglecting the resistors to ease the discussion), at normal condition and under an external applied voltage.

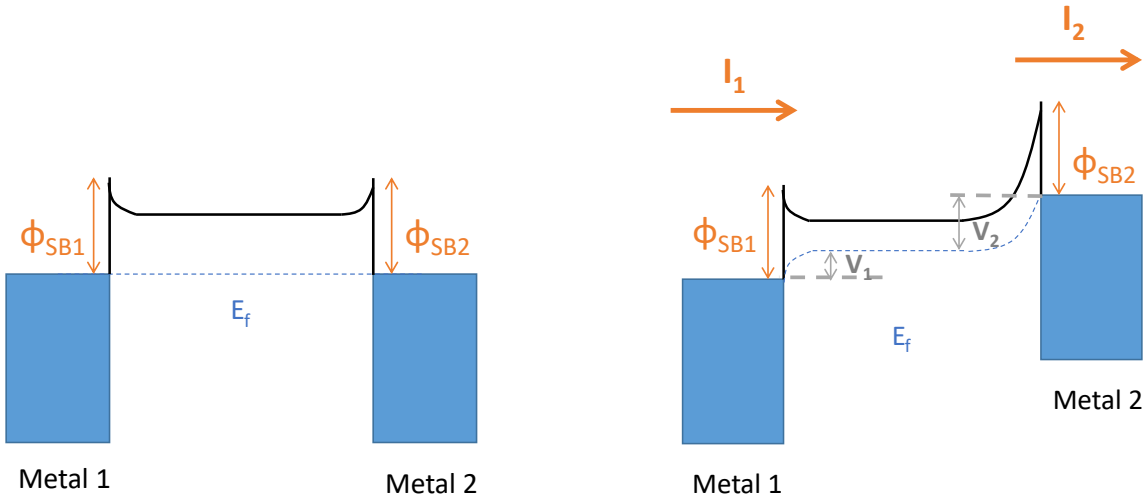

(a) Band bending under normal condition

(b) Band bending under an applied voltage, split in V_1 and V_2 that is the effective voltage perceived by the schottky diode, with $V = V_1 + V_2$

Figure 2.18: [42]

By taking into account the continuity of current across the device and the current in *equation 2.4* we end up with the following equation:

$$I = \frac{2I_{SC1}I_{SC2}\sinh\left(\frac{V}{V_t}\right)}{I_{SC1}e^{\left(\frac{V}{2V_t}\right)} + I_{SC2}e^{\left(-\frac{V}{2V_t}\right)}}$$

In the given equation both the the pinning state and the ideality factor may be inserted to properly define the correct behaviour by considering the voltage drop across each contact. for a detailed analysis [43, 42] The dark current will be then extremely low if compare to other devices, enhancing the minimum detectable capability, moreover high speed photodetection can be achieved thanks to the low junction capacitance and high bandwidth [41].

Chapter 3

Fabrication

The fabrication processes concerns only the ZnO UV PD's. It consists on several cleanroom process at wafer level, and a last step performed at die level which is carried out through the use of a tool which deposits nanoparticles on top of patterned electrodes. Due to the uncertainty of the contact type of the ZnO-metal contacts caused by the nanostructuring, different types of metal has been deposited and patterned in order to investigate which type contact the particles will form. The chosen metal have various work functions, starting from a very low one (TiN) to very high one (Pt). In addition two dissimilar substrates has been chosen for reasoning that will be clear during our discussion, see *appendix C*. The selected metal with relative substrate, and order of patterning, is itemized here:

1. Ti/TiN and Cr/Au on SiO_2/Si
2. Ti/TiN and Ta/Pt on SiO_2/Si
3. Cr/Au and Cr/Ag on SiO_2/Si
4. Ti/TiN and Cr/Au on Fused silica
5. Ti/TiN and Cr/Ag on Fused silica

The processes involve the use of two masks reported in *figure 3.1*. The first one on the left, *figure 3.1a*, is related to the metal with lower work function and the other one, *figure A.1d*, to the higher metal work function (with the exception of number 3 listed above where is the opposite). As can be appreciated, in the middle of the die there are two, long columns. The one on the left is characterized by two terminal contacts, where the first one has a circle shape surrounded by the second contact whose has a circular crown configuration. The label designed close to them express the radius of the circle and the spacing between the two metals in micrometer (an example is R75D20 means radius of 75 µm and distance of 20 µm). The other column is instead a three terminal contacts for a MESFET configuration where two terminal are the drain and source and the other one the gate. The label designed, defines the length and distance of drain and source and then the spacing between source and gate (symmetrically also drain and a gate), (an example is 200x25 D5 that is 200 µm long and 25 µm spacing a distance of 5 µm). The contacts at the edge of the die are always the same as the one in the left column, but a wider electrode has been designed for 4 point probe measurement and for wire bonding needed to route the device to a package for optical tests.

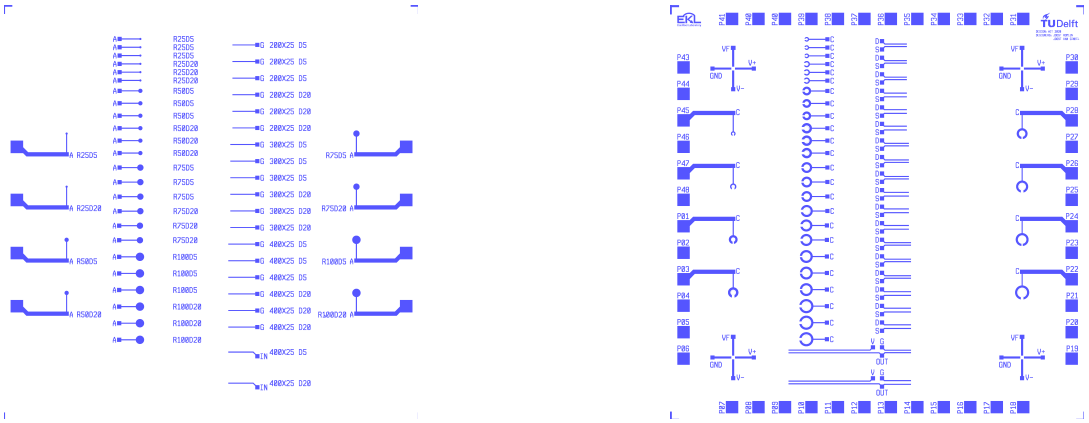

(a) Mask for first metal patterning

(b) Mask for second metal patterning

Figure 3.1: Die representation

3.1 Metal patterning

The raw materials are a single side polished Si wafer of (525 ± 20) µm p-type (100) crystallographic direction, and double side fused silica glass wafer of (500 ± 20) µm. Regardless of the type of substrate, a cleaning procedure has been carried put before each deposition and etching processes. Depending if the the wafer contained already patterned metal or not, they have undergone different treatment. For instance, wafers with only Si and all its derived compounds has been cleaned by dipping them in fuming nitric acid (Merck: HNO_3 99%) for 190 minutes at RT, then rinsed in deionized water until the resistivity of the bath reached 5 MΩ, followed by other 10 minutes in fuming nitric acid (Merck: HNO_3 65%) at 110 °C then rinsed in deionized water until the resistivity of the bath reached 5 MΩ to remove any left residues. On the other side, fused silica wafers and Si wafers with metal has been cleaned only by the first step described previously to prevent any contamination. The use of two substrates, anyhow, implied processes flow slightly different one from each other, which shared the main core for metal patterning.

A zero layer, that is a photolithographic process required for patterning the alignment marks, as shown in *figure 3.3a*, has been carried out on the Si wafers. A simplified schematic representation is depicted in *figure 3.2*. It consists of a manual treatment with HMDS (hexamethyldisilazane) vapor with nitrogen as a carrier gas for 10 minutes, then spin coating with Shipley SPR3012 positive photoresist to reach 1.4 µm thickness (first step spinning velocity 500 rpm of 10 s with a ramp of 1,000 rpm/s, and a second step with a spinning velocity 2,500 rpm of 30 s with a ramp of 2,500 rpm/s), and a soft bake at 95 °C for 90 s. Then, the wafers have been exposed through projection with 5:1 de-magnification thanks to an automatic waferstepppper with an energy of 130 mJ/cm^2. Afterwards, they have been submitted to a post-exposure bake at 115 °C for 90 s, followed by a development step using Shipley MF322 developer (double puddle process), and a hard bake at 110 °C for 90 s. A dry etching, through ICP-RIE, has been carried out to obtain the alignment marks by removing 120 nm into the silicon with the platen temperature hold at 20 °C, and then the remained photoresist as been removed in a oxygen plasma with an end-point detection mechanism plus 120 s overetching.

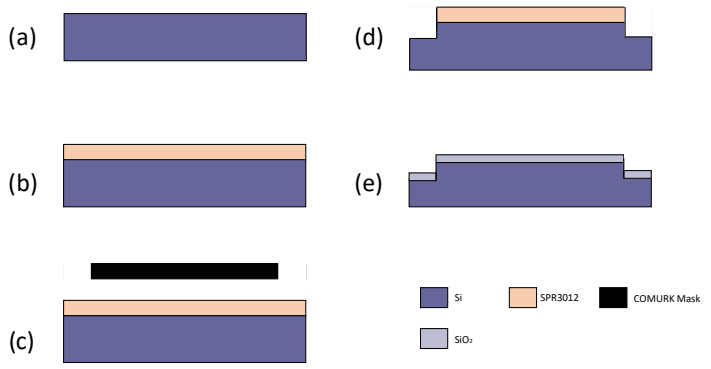

Figure 3.2: Schematic side view zero layer process

An oxide layer has been grown by thermal oxidation with the purpose of insulating electrically the substrate and the metal as well as the particles further deposited hampering any leakage and contribution from the silicon on the electrical performances of the devices. The *table 3.2* details of the steps to grow 300 nm of SiO_2, as schematically shown in *figure 3.2e*.

Process	**Temperature [°C]**	**Gas&Flow [l/min]**	**Time [min]**
Boat in	600	N_2 : 6	5
Stabilize	600	N_2 : 6	10
Anneal	600	N_2 : 6	15
Heat up	+10 °C/min	N_2 : 3 O_2 : 0.3	40
Stabilize	1000	N_2 : 3 O_2 : 0.3	2
Oxidation	1000	O_2 : 2.25 H_2 : 3.85	42
Cool down	-7 °C/min	O_2 : 2.25 O_2 : 3.85	60
Boat out	600	N_2 : 6	5

Table 3.1: Step for thermal oxidation

The thickness of the formed layer has been measured through a Woollam Ellipsometer.

	Thickness [nm]
Wafer 1	296 ± 7
Wafer 2	291 ± 6
Wafer 3	285 ± 8

Table 3.2: The numbered position is related to the distance with respect to the heating part of the ceramic furnaces, higher value entail higher distance

On the other side, handling fused silica wafer required other precautions.
At first, it has not been patterned with a zero layer and being already an insulator there was no need of depositing or growing another dielectric layer. However, as shown in *figure*

3.4b, a thin layer of aluminum has been deposited on one of the side of the wafer. The main reasons is related to the further process requirements. Indeed, the dry etching tool adopted to remove TiN detects the wafer through the help of optical sensor. Thus, every time a wafer has to be moved from one chamber to another one an infrared sensor detects its presence or not. Therefore, since glass is transparent to the VIS-infrared region of the electromagnetic spectrum, if no remaining metal would be left after etching, there would be the risk of wafer stuck inside one of the chambers, which has to be manually removed each time the process is performed.
The choice of aluminum as metal is mostly accomplished in order to differentiate in a clear way the front and back side of the wafers given that the first deposited metal is TiN(the color difference is noticeable with naked eye). To sum up, before the first photolithographic process, 200 nm of Al has been deposited through RF sputtering, through the help of carrier wafer to prevent wafer stuck in the tool for the same reasoning as before. This layer has been etched with a wet process in a bath of PES (Phosphoric Acid Etching Mixture) hold at 35 °C for 150 s, after the first mask has been properly patterned.

Despite the previous explained variation in the process flow, all the other phase are the same regardless of the substrate. In *figure 3.4* are depicted the main steps.
The first procedure is the coating of the front side with the stack Ti/TiN. It consists of RF sputtering 10 nm thick layer of Ti (thin layer used to improve the adhesion of titanium nitride), followed by RF reactively sputtering 100 nm thick layer of TiN (fairly good conductor needed to prevent titanium to oxidized easily), both carried out with the wafers hold at 350 °C, with the aim of improving the conductivity of the deposited layer. Moreover, between one process wafer and the following one, a dummy wafer has been added to clean the chamber and target material. Afterwards,the wafers has been treated with HMDS for 10 minutes, then spin coated with Shipley SPR3012 positive photoresist to reach 1.4 µm thickness, and a soft bake at 95° for 90 s, done by an automatic coater. Then, the wafers have been exposed through soft-contact alignment by a manual contact aligner with an energy of 130 mJ/cm^2. Afterwards, they have been submitted to a post-exposure bake at 115 °C for 90 s, followed by a development step using Shipley MF322 developer and a hard bake at 110 °C for 90 s. The metals has been etched via ICP -RIE dry tool, which took 63 s, and then the removal of the remained photoresist in a oxygen plasma with an end-point detection mechanism plus 120 s of overetching (the etching time depends on the thickness of the layer). Subsequently, the wafers has been again treated with HMDS for 10 minute, then spin coated with Shipley NLOF2020 negative photoresist to reach 3.5 µm thickness (first step spinning velocity 700 rpm of 10 s with a ramp of 1,000 rpm/s, and a second step with a spinning velocity 1,060 rpm of 30 s with a ramp of 1,060 rpm/s), and a soft bake at 95 °C for 90 s. Then, the wafers have been exposed, as before, with an energy of 140 mJ/cm^2. Afterwards, they have been submitted to the same development step. An e-beam evaporator has been employed to coat the wafers with 10 nm thick layer of Cr (adhesion layer) and 100 nm thick layer of Au, monitoring that the temperature chamber would not exceed 90 °C. A lift-off process has been performed to remove the Cr/Au from the areas it should be lifted off (it takes roughly 10 minutes). It has been accomplished using NMP(N-Methyl-2-pyrrolidone) bain-marie your contained would empty at 70 °C in an ultrasonic bath, rinse, next, in running deionized water for at least 5 minutes. As final step, the wafer has been diced in die. The final configuration of the alignment marks is reported in *figure 3.5*.

(a) Zero layer

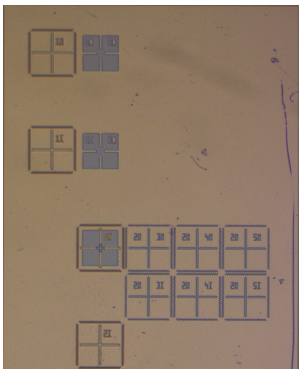

(b) First Layer

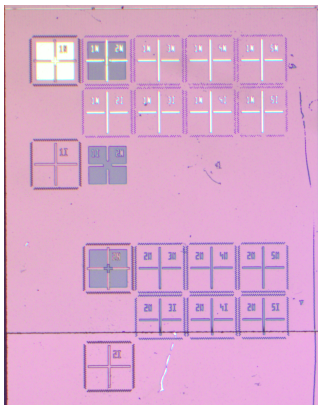

(c) Second Layer

Figure 3.3: First two alignment marks starting from first lithographic process to the last one on SiO_2/Si

Due to the extensive diversity of metals used, few shrewdness has been considered. The wafer prepared with the stack Ti/TiN and Ta/Pt on SiO_2/Si, number 2 in the list at the beginning of *chapter 3*, instead of having a total metal thickness of 110 nm (the sum of the effective metal and the adhesion layer) is 60 nm thick layer. Indeed, the evaporation of 100 nm of Pt would reach a temperature that may cause some damage to the photoresist such as thermal reflow, resulting in bad features. Moreover, the wafer, with the stack Cr/Au and Cr/Ag on SiO_2/Si, number 3 in the list at the beginning of *chapter 3*, have been obtained by following two lift off photolithographic process. For instance, the first lithographic step has been obtained, as already explained before for the negative photoresist, and the exact same procedure has been followed for the second lithographic process but instead of using an automatic coater-developer, the wafer has been coated and developed manually.

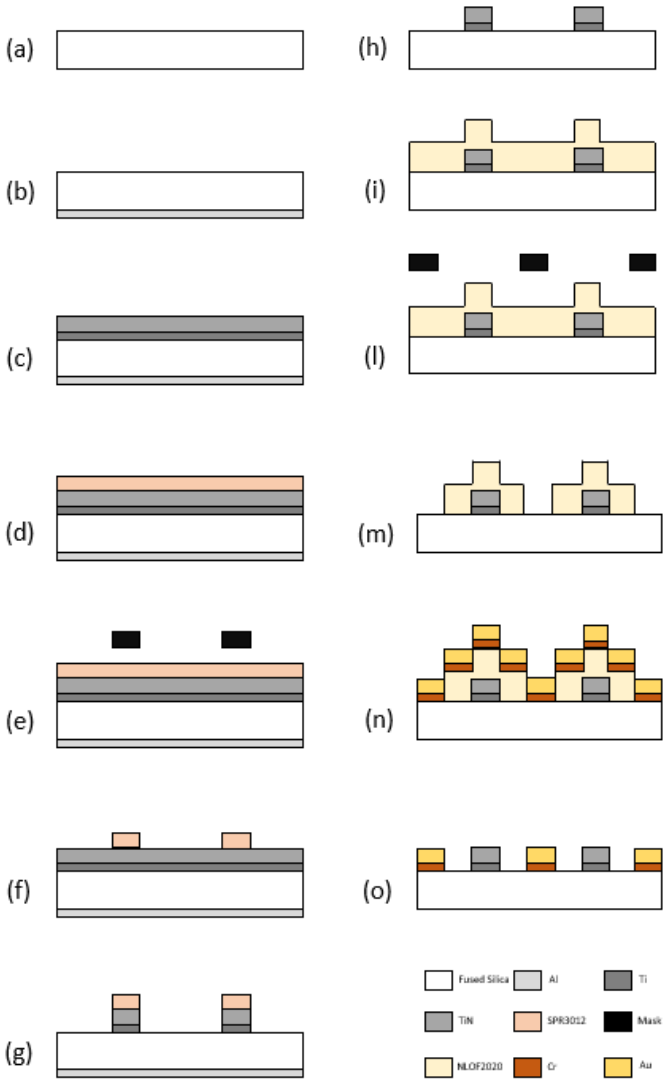

Figure 3.4: Schematic side view of process flow with fused silica as substrate and Ti/TiN and Cr/Au as metals

The final metal look like the ones illustrated in *figure B.1.*

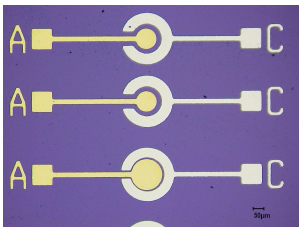

(a) Two terminals contacts

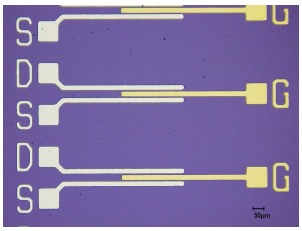

(b) Three terminals contacts

Figure 3.5: Example of patterned Cr/Au and Cr/Ag on SiO_2/Si

3.2 Nanoparticle deposition

As already mentioned in the previous chapter, the final fabrication process is the particle deposition to form the active devices. The process exploits the combination of spark ablation and impaction printing technology, through a method similar to PLD.

3.2.1 Spark Ablation

Spark ablation synthesis relies on the electrodes being ablated by spark dis charges that are induced between them, the production outcome is similar to those achieved by laser ablation [44]. In its initial form, the procedure used only the substance or combination of substances that were intended to make up the particles, with resulting very high purity in the film quality, in addition, in the aerosol form before being impacted on a substrate, the particles may experience reactive modification such as oxidation or size selection.
The physical process behind the ablation consists of rapid heating of very tiny spot on the electrodes, where the material is instantaneously brought to its boiling point, since the temperature reaches even 20,000 °K [45] or even higher [46].
After the spark is extinguished, the column of vapor formed by each spark, *figure 3.6a*, near the electrodes cools by adiabatic expansion and mixes with the gas flowing around it and condenses to form nanometer-sized particles or smaller. A slow vapour cooling would induce the formation of condensation nuclei, in which more vapor would condense and subsequently the particles formed would grow by collision, according to the classical process of vapor nucleation and condensation.By adjusting the concentration of the evaporated material in the initial phase of particle formation, the structure can be tuned from single atoms to nanocomposite agglomerates as in *figure 3.6b*. The reached formation state is achieved by a continuous flow arrangement. The energy per spark and the process gas flow rate through the spark areas determine the initial concentration of mass ablated.

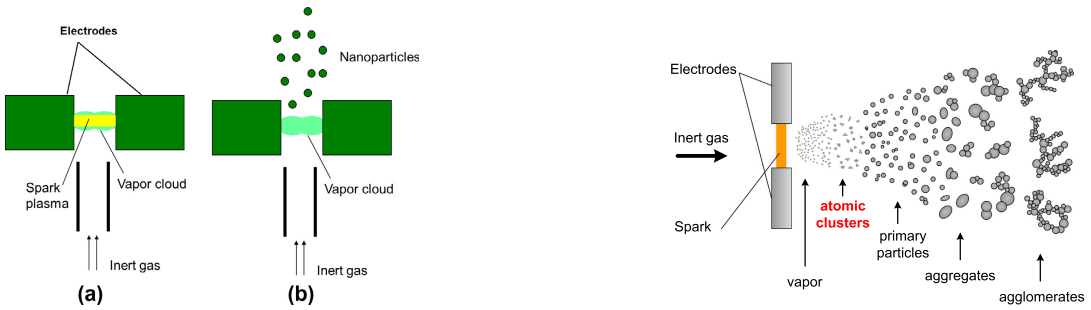

(a) The basic topology of a spark generator

(b) Change of particle state generated by spark discharge

Figure 3.6: [47]

Wide range of material classes may be created including pure metals, alloys, non-alloyed composites, semiconductors, oxides, hybrids, etch. At RT adhesion can be expected to be independent of material and most metal particles are solid and do not pass through a liquid phase upon condensation, implying the the forming particle are independent on the boiling or melting point of the material Therefore, the spark process has an the excellent mixing

capability if electrode ablated of different elements are initially placed and different solution may be implemented according to the requirements, as illustrated in *figure 3.7*.

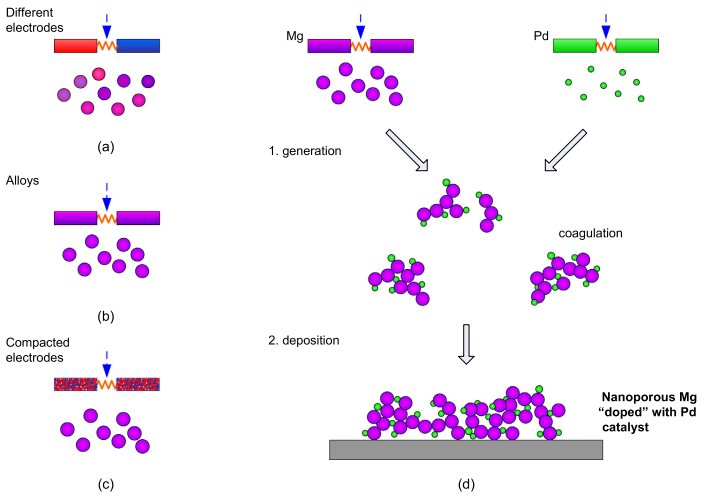

Figure 3.7: Different principles of spark mixing: atomic mixing (a)–(c) and nanomixing (d) [47]

In order to keep a constant ablation rate, a specific generation circuit must be implemented. *Figure 3.8a* represents the block diagram, where the continuous current source keep a background discharge, which not cause any ablation, avoid the pulse ignition and shut down of the spark every time. The pulse forming network instead superimpose and appropriate AC signal to set up the desired spark formation.

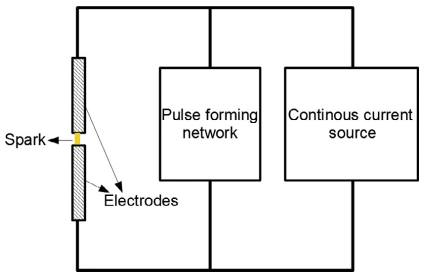

(a) Block diagram

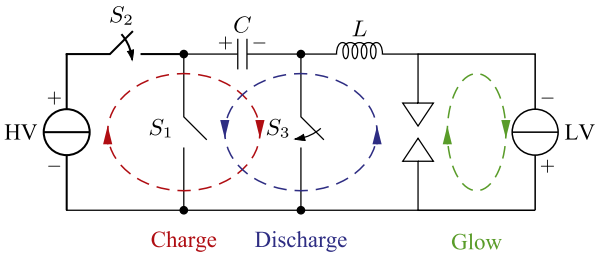

(b) Example adapted circuit

Figure 3.8: [47]

An effective circuit is shown in *figure 3.8b*.When S_1 is closed, the left-hand side of the capacitor is forced to 0 V, and a negative high voltage pulse hits the top electrode, resulting in the formation of a spark. With the purpose of keeping a sufficient space charge for stable spark ignition, a low-power glow current must be applied across the gap [47, 48].

3.2.2 Impaction Printing

Impaction printing relates to the process through which it possible to direct print particle or ink droplets in a non-contact mode (the substrate is in contact only with materials which

make up the device and this lowers the risks of damage and contamination). The non-contact patterning method also permits to obtain accurate alignment with already on the substrate which is an indispensable functionality to pattern multilayered devices. it is possible to easily build 3D structures additively by printing multiple layers of the same or different materials. By a proper collimated and isolated carrier gas, the aerosol material is carried by the flow streamlines and via a pressure difference between the gas and the substrate the carried particle will hit the surface by sticking onto it.
Aerosol jet printing is included as one of this technique [49, 50].

3.2.3 Nanomaterial printing setup

The tool, named VSparticle, employs an aerosol printing technique where the selected material is generated through spark ablation. It includes both the generator box and a dedicated hardware to interface the spark and the chamber. dis A schematic representation is depicted in *figure 3.9*. The carrier gas flow across a duct is inserted in between the spark generation area, then through a series of valves appropriately turned to reach the chamber. Inside the printing chamber there is a pitted fixed stage for samples displacement, and a movable stepping motor to whom are properly attached both the cable for the conduction of the carrier gas flow which are routed to the nozzle and an optical microscope, as illustrated in *figure 3.10*. The nozzle is, thus, free to move in the xyz direction. The chamber is kept under a constant soft vacuum (at least lower than 1 mbar), for a reasonable sealing from impurities and other contaminants. The carrier gas available are N_2 and Ar controlled by the VS-NMP1 nanoprinter and H_2 instead controlled by another flowmeter.
A dedicated user-friendly interface, enable the monitoring of the settings. where is reported a real time graph which show the flow rate, current and voltage of the spark generator. Indeed, it can be set the flow rate, and selected the desired voltage and current value, as well as the ignition of the spark. A prompt terminal for G-code allows the control of the nozzle movement.

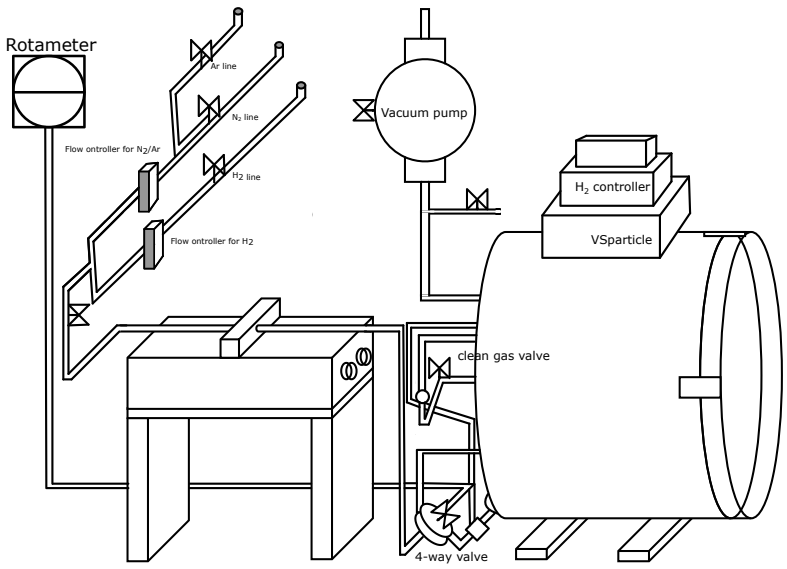

Figure 3.9: Schematic representation o the set up

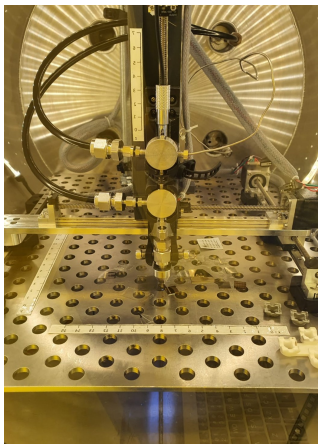

Figure 3.10: Stage and relative nozzle

The following detailed process describe accurately each step for the deposition. Firstly, all the valve are checked and closed to disconnect the chamber form the remaining load-bearing elements of the set-up. If the suitable electrode are already inserted, the main switch of generator is turned on manually (generally, even if anyone is not using, the system is powered up), otherwise a previously the electrodes are replaced (the previous electrode are cleaned by dipping in Acetone and IPA (isopropanol) a put in special containers). Then, the chamber is vent until the pressure rises up to at least 0.8 mbar meanwhile each die has been cleaned by dipping in Acetone and IPA (isopropanol) in case of the presence of Ag or in a fuming nitric acid HNO_3, rinsed then in deionized water in all the other cases and dry through a nitrogen gas (Ag is chemically reactive to nitric acid). After removing the lid of the chamber, the die are loaded via a double tape on the stage, and then closed pump down again. The valve a priory of the source are open and the flow is set via software to the desired flow. The rotameter which monitors the flow rate of N_2 and Ar is adjusted in order to higher value than the nozzle through flow.

Nozzle	N_2 **(Torr)**	Ar **(Torr)**
004	0.32	/
035	0.53-0.57	0.35-0.38
125	1.17	0.75

Table 3.3: Nozzle aperture are labeled 004, 035, 125:

The nozzle is then move far away from samples to limit unwanted particle deposition. The chamber is connect to the aerosol flow, opening the 4-way-valve and the valve (number and *figure* respectively) one right after another, in order to prevent blockage of all gas lines or even worse pressure build up may occur.
The current and voltage are set and the spark switched on. After waiting that the signal stabilized to the set point, the tool is ready to operate.
The next phase is the alignment of the nozzle with respect to the desire deposition area. Firstly the z alignment is achieved by moving in relative coordinate. The microscope is focused on the stage, the coordinates are reset and the z position is saved. Then the nozzle is lowered until it touches the surface (the touching point may be notice from the camera when the picture slides), then the distance between the touch and focal point is saved. Then, by

choosing the wanted printing distance between the sample and the nozzle, the stage is lower of an appropriate quantity ($q = d_{\text{focal-point}} - d_{\text{deposition}}$). Then an xy correction is carried out. Technically, the in plane distance of the nozzle and the camera are fixed ($x = 0.4\,\text{mm}$ and $y = 17\,\text{mm}$), however slightly misalignment may be expected depend on the precision of the previous step. After aligning on a sample in a specific point a dot is printed and after the deposition is finished and the camera is brought back to the original point, the xy direction is adjusted depending where it has been realized. After that, the tool is ready (the spark may stay on during all the time required). An example of the code is given below:

G90: *movement is set in absolute coordinate*
G92 X0 Y0 Z0: *set current position to (0,0,0)mm in absolute coordinate system*
G1 X0.6 Y18.25 F200: *G1 linear movement to end point (0.6,18.25) mm with maximum speed (*200 mm/min*)*
G1 Z-1.45: *the nozzle is move down of* 1.45 mm*, from the focal point (i.e.q)*
M9 G4 P60: *M9: the nozzle is open and start deposition, wait 60s*
M8 G4 P1: *M8 the nozzle is closed, and wait 1s*
G1 Z1: *the nozzle is move 1mm up*
G1 X0 Y0 Z0: *G1 linear movement original position*
G91: *movement is set in absolute coordinate*

Once finished, the spark is turned off, the gas flow controller is set to zero and all the valve are closed, the chamber is vent and the sample unloaded. Then is pump down and left for the next user.

3.2.3.1 Zn NP deposition

In case of Zn electrodes, the voltage and current were set to 1 kV and 3 mA respectively, since providing the best ablation rate. In addition, the optimal carrier gas is Ar/H_2 with respect to N_2, since the oxidation rate of zinc nanoparticle is lower, set to 1.5 L/min.
To guarantee an uniform deposition, the desired area has been printed multiple times with high speed printed (ranging from 18 to 30mm/min 60 times) generally creating rectangle for an appropriate coverage. The schematic in *figure 3.11* shows how the particle are landed, both filling the spacing between the metals and also partially covering it, he particle film formed.

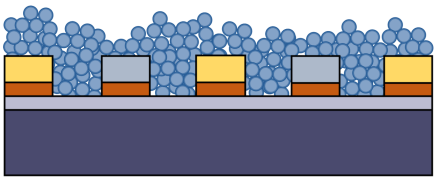

Figure 3.11: Schematic representation of Zinc nanoparticle on metal contact Au/Ag

After the deposition, an EDS analysis has been performed on top of a silver pad.
The only atoms detected are oxygen, silver and zinc in all the point shown, with different percentage, which means no other impurities are present and the deposition is sufficiently good. However, the atomic ratio between oxygen and zinc is not equal, therefore a thermal treatment is demanded, as also further described in *section 4.1*.

3.3 Other Equipment

For all the process in cleanroom, several tool has been used but we are just going to cite them wtih their respective function:

- EVG 120 coater-developer for photoresist coating and developing automatically.
- ASM PAS 5500/80 waferstepper
- SUSS MicroTec MA/BA8 mask aligner contact aligner
- Microscope Olympus for optical verification before and after each photolithographic step
- Trikon Omega 201 dry etcher
- Trikon Omega 204 dealer RF sputter coater
- Dektak 150 for mechanical profilometer
- Tepla plasma 300 for photoresist stripping
- CHA Solution Std. for metal evaporation
- Ceramic furnaces for wet oxidation
- Woollam ellipsometer for film thickness measurement

Optical microscope, SEM XL30 SFEG, EDS and AFM, has been employed to fully characterized the morphology and properties of ZnO before and after annealing as well as for verifying detrimental effect caused by temperature on some of the metals deposited.
The electrical characterization has been performed via a cascade four point probe station in 2 or 4 point contact configuration depending on area available in the metal pad of the DUT (only the pads at edge of the dies have sufficient areas to displace all the needles). Four UV's LED 5 mW at 265 nm have been correctly attached on the ring of the cascade system all the way around the optical microscope in order to perform an analysis of the I-V curve under UVC exposure. The response time has been measured thanks to another same LED and Keythley 2450 Sourcemeter, in a enclosed box to guarantee a sufficient dark environment.
For the evaluation of PDs optical response, an home built set-up has been employed. A schematic representation is depicted in *figure 3.13*. The ILD-D2-QH Deuterium-Halogen Source, [51], from Bentham with 706 Deuterium Lamp Power Supply from the same company were selected, and another power supply was chosen for the halogen bulb. An electrical switch select the light source collimated in the monochromator. All the measurements has been done with the deuterium bulb because it has a higher intensity in the spectral range of interest (graphs reported in [51]). The polychromatic light has been split in each wavelength through the use of iHR320 from Horiba monochromator, which is a mid-focal length imaging spectrometer with a 320 nm focal length. By controlling the incidence and diffraction angles, the desired spectrum of the diffracted beam goes out the monochromator through the output slit. A key aspect to understand is that the polychromatic light is split with different orders. This means that second or higher order components of smaller wavelength can be present together with the desired wavelength, as illustrated in *figure 3.12*.

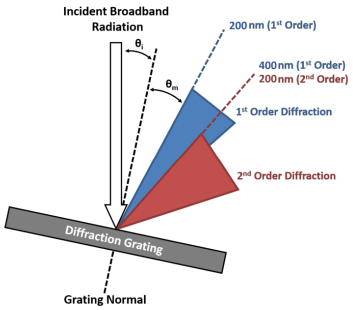

Figure 3.12: Schematic representation of reflected light in a diffraction grating

Since there is no optical filter properly inserted in the system, high diffraction orders may be present above 400 nm inducing change in the DUT response. The beam coming out from the monochromator is modulated mechanically by an optical chopper system.
The MC2000 optical chopper system from Thorlabs is composed of a chopper control console, a chopper wheel and a motor head assembly. The chopper frequency was set in order to respect the operating limitations of the controller and the wheel, and also to reduce known noise sources such as the line voltage frequency, low frequencies where flicker noise dominates. Hence, 123 Hz has been selected. The chopper frequency was also provided through to the lock-in amplifier via a BNC cable in order to demodulate the output signal of the device under test.
A 7225 Dual Phase DSP Lock-in Amplifier from AMETEK has been used in the setup for AC(that is when the chopper was activate and the light was as pulse form) measurement and the instrument performs all of the normal measurements of a dual phase lock-in amplifier, measuring the in-phase and quadrature components, vector magnitude, phase angle and noise of the input signal, In DC mode, that is when the chopper was lswithed off, a Keithley 2450 Sourcemeter has been employed.
The concave mirror used is the CM750-200-F01 from Thorlabs with UV-Enhanced aluminum coating for a range from 250 nm to 450 nm and focal length of 200 mm, for reflectivity graph [52]. A LabVIEW code allows to properly interface all the components through software, enabling data collection, processing and the whole system integration.
All the measurements has been carried out starting from a wavelength up to an higher one (no results difference has been noticed by proceeding in an opposite way). The selected spectral range is in between the minimum reachable value 200 nm and 400 nm.

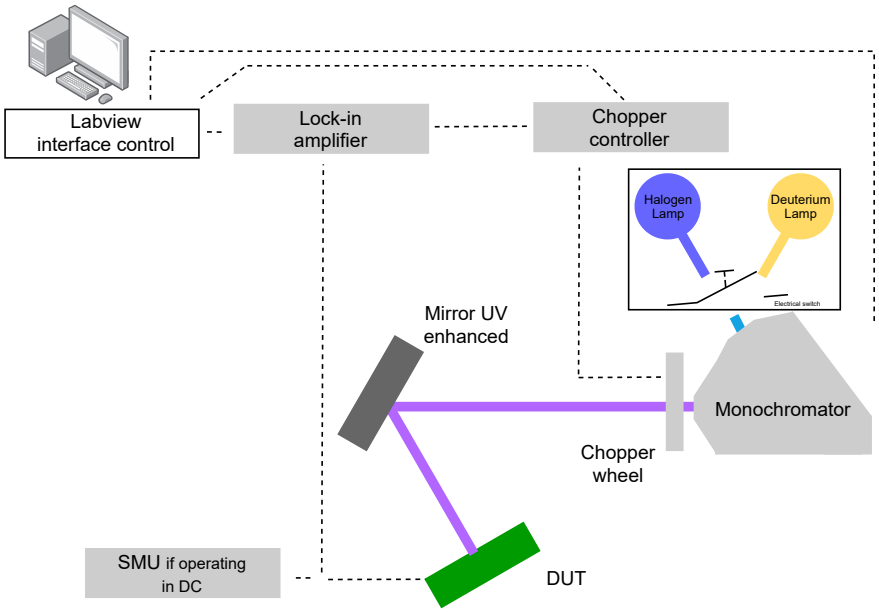

Figure 3.13: Set up adopted for measuring the responsivity of DUT only in the UV range above 200 nm

An UV-VIS-NIR Perkin lambda 1050+ spectrometer has been used in order to measure the total UV-VIS transmittance of ZnO. The measures starts from an high wavelength down to a lower one. A schematic representation, which exactly reproduces the optical path of the tool, in *figure 3.14* depicts how the light is focused on the target. For the total transmittance measurements performed, both lamps available has been selected, where the halogen-tungsten is set for the data extracted until 320 nm and then automatically is switched to the other lamp for the lowest wavelength (down to 225 nm). The beam, before reaching the DUT, is split in two half for a double measurement simultaneously (one for the device to analyse and the other one for a reference), however this option has not been adopted. Indeed, each time, only the transparent substrate has been computed and afterwards, the substrate with the material of interest on top. An integrating sphere, coated with an highly diffusive reflective material, reflects the light ,which has travelled through the DUT, until it gets to the InGaAs photodetector and a PMT as illustrated in *figure 3.15*

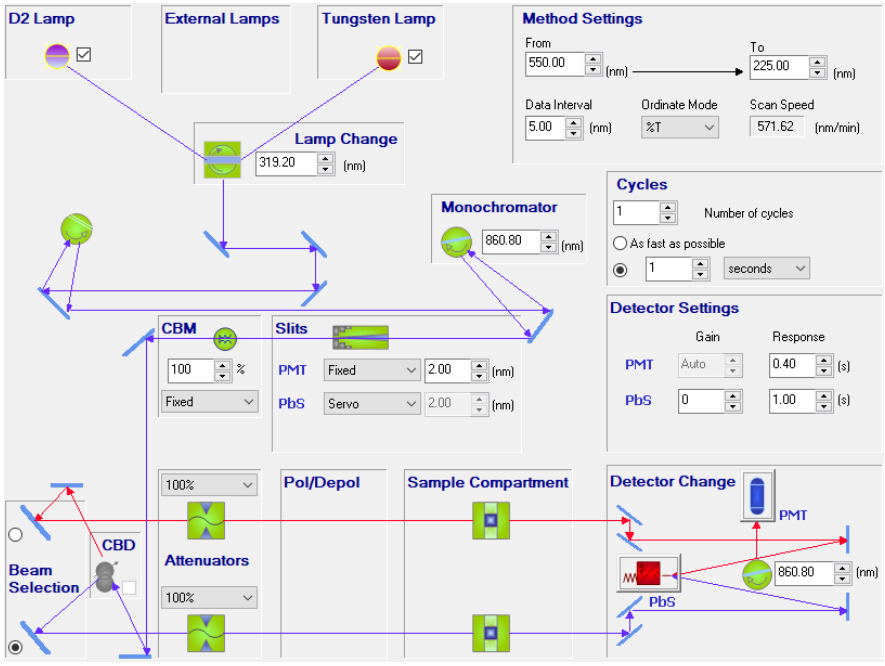

Figure 3.14: Optical path from source to DUT

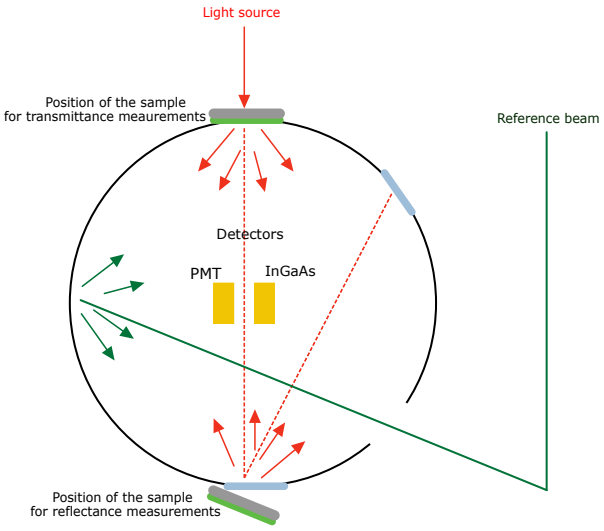

Figure 3.15: Integration sphere schematic

Chapter 4

Results and Discussion

4.1 Structural characterization

A structural analysis of the nanostructure zinc oxide device have been performed after deposition and annealing.
Previous studies on photoresistors, formed with the MSM structure, Au-ZnO-Au, gave the results reported in *figure 4.1*, where the carrier gas for the deposition and annealing has been properly examined.

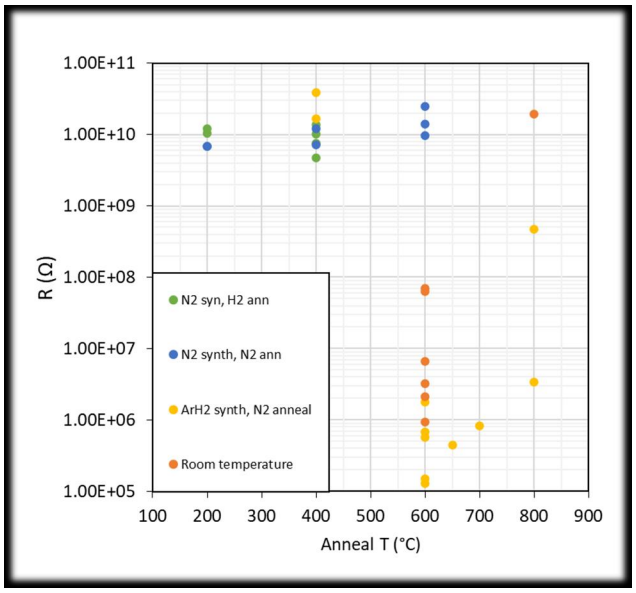

Figure 4.1: Resistance according to different settings

The best setting are N_2 oven for at 600 °C for at least 6 hours. Therefore, the starting point was using these parameters for the new samples. However, the presence of other different material, mainly TiN and Ag required utmost care especially with the annealing condition. It is well known that TiN is a fairly good conductor quite resistant to oxygen at ambient temperature, however depending on the combination of time and temperature it may experience oxidation forming TiO_2 or even further TiN_xO_y as also described in detail in [53]. On the other side, Ag, is very oxidation resistant and can withstand high temperature, may

experience dewetting, as happened, as discussed in with more accuracy in *appendix A*. The final parameters were defined trying to have the highest temperature and longest baking time to obtain the best electrical performances (improve conductivity). Therefore, the optimal annealing condition were 400 °C for 2 hours in case of samples with Ag and 400 °C for 5 hours for all the other remaining samples, where the previous detrimental effect were not verified.

Of course, the need of an annealing step is necessary to have full oxidation of the zinc oxide film, since RT environment would not be sufficient, *figure B.1*. Indeed, an analysis on the material composition with their atomic percentage has been performed on different samples taking directly out from the chamber of the nanoprinter tool (no temperature treatment) and after a tempering process. A dot on top of a Au or Ag pad on two different dies, obtained by sparking for 5 minutes on the same spot, was produce to have sufficient thick layer so that that the substrate would not affect EDS analysis. The resulted reported in *figure 4.2* where the one in Au has undergone a thermal treatment and the other not.

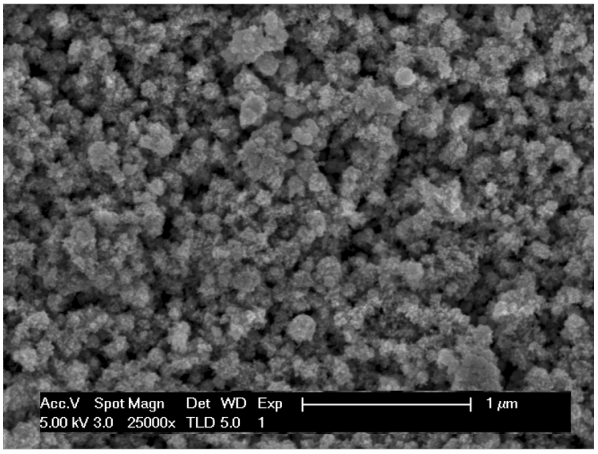

(a) Dot on a Ag pad on SiO_2/Si at the edge of a die

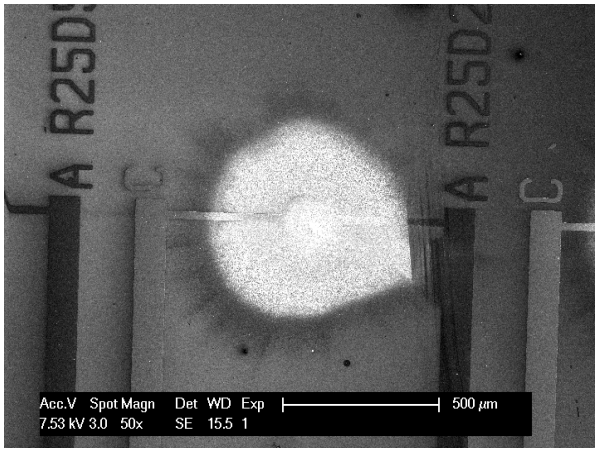

(b) Dot in between Au/TiN electrodes on SiO_2/Si

Figure 4.2: SEM picture of the area used for EDS analysis

The EDS analysis performed on the sites reported resulted in the following *figure* **??**:

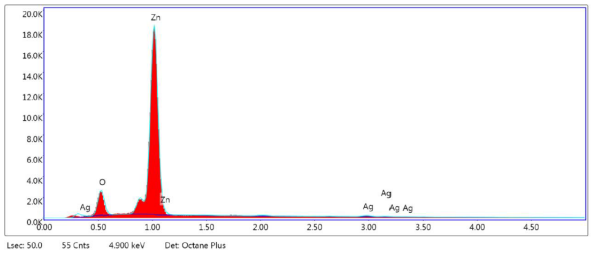

(a) Sample taken out the chamber as not annealed on Ag electrode

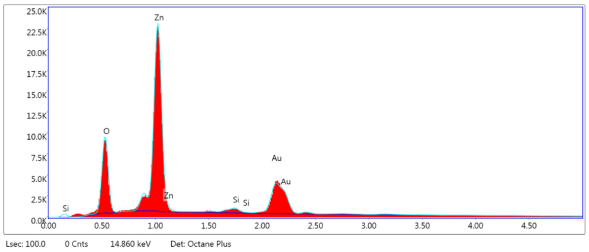

(b) Sample Annealed for 400°C for 5 hours on Au electrode

Figure 4.3: SEM pictures before and after annealing on different spot with accelerate electron beam

and their relative percentage are in the following tables:

Element	Weight%	Atomic%	Net Int.	Kratio	Z	A	F
O K	7.39	24.81	356.86	0.0692	1.2089	0.7746	1.0000
Zn L	89.74	73.76	2338.75	0.7884	0.8563	1.0261	0.9999
Ag L	2.88	1.43	23.23	0.0221	.7680	1.0010	1.0005

Table 4.1

Element	Weight%	Atomic%	Net Int.	Kratio	Z	A	F
O K	13.97	45.45	669.60	0.1328	1.2573	0.7565	1.0000
Zn L	56.01	44.60	1431.62	0.4938	0.8906	0.9904	0.9996
Si K	1.27	2.35	51.06	0.0129	1.1431	0.8902	1.0006
Au M	28.75	7.60	7.60	0.1947	0.6534	1.0381	0.9981

Table 4.2

In *figure 4.3a* and as also reported in the evaluated atomic ratio *table 4.1*, the ratio of oxygen and zinc is not 1:1 as it would be expected in case of a complete oxidation. The oxygen bond to the zinc is not sufficient, probably because the energy required to fully penetrate in the porous layer was not be sufficient and zinc is still in its metallic phase. Anyhow, the absence of detected Si certify that the oxygen comes only from the zinc-oxide layer and not from the SiO_2 underneath, whereas only few e- counts identify the presence of Ag.
On the contrary, from *figure 4.3a* is clear that electron counts of oxygen emission is higher with respect to previous case. Moreover, as written in *table 4.2*, the atomic ratio is about the same, although a partial contribution may be given by the substrate since there is also a very few percentage coming from Si. An x-ray diffraction analysis on the annealed sample would have been useful to have a more solid view. Relying on the analyses performed after annealing of 600 °C for 6 hours, depicted in *figure 4* of *appendix D*, only a zincite phase and no pure Zn crystalline is present which did also happen at 400 °C. Indeed above a certain threshold temperature, the zinc oxidizes easily and the effect of a longer annealing ensures better electrically performances most of all, while the morphology remain unaffected unless there is huge particles migration.
The topological composition is not affected by temperature, indeed as illustrated in *figure B.1*, indeed the porosity as well the structural arrangement is mostly the same, no crystalline site is present, but only agglomeration of particles with different dimensions, resulting in a very irregular and uneven film. Through the help AFM, analysing a spot on top of a samples with metal layers, we were able to assert the roughness of the surface as well as other important parameters. For instance, the S_q = 92.5 nm (RMS roughness), the means roughness, S_a = 73 nm, the Skew, S_{sk} = 0.888,781 nm in a 50x50 µm^2 square are large values if considering the small area analysed, a good smooth surface would have few nanometers. The 2D and 3D picture are in *figure 4.5*.

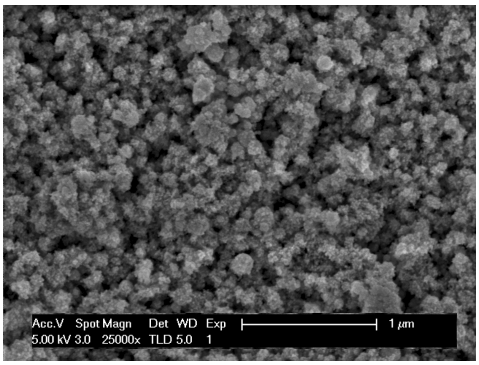

(a) Sample as deposited

(b) After a thermal treatment at 400°C for 5 hour

Figure 4.4: SEM pictures of zinc nanoparticle before and after annealing on the Ag pad

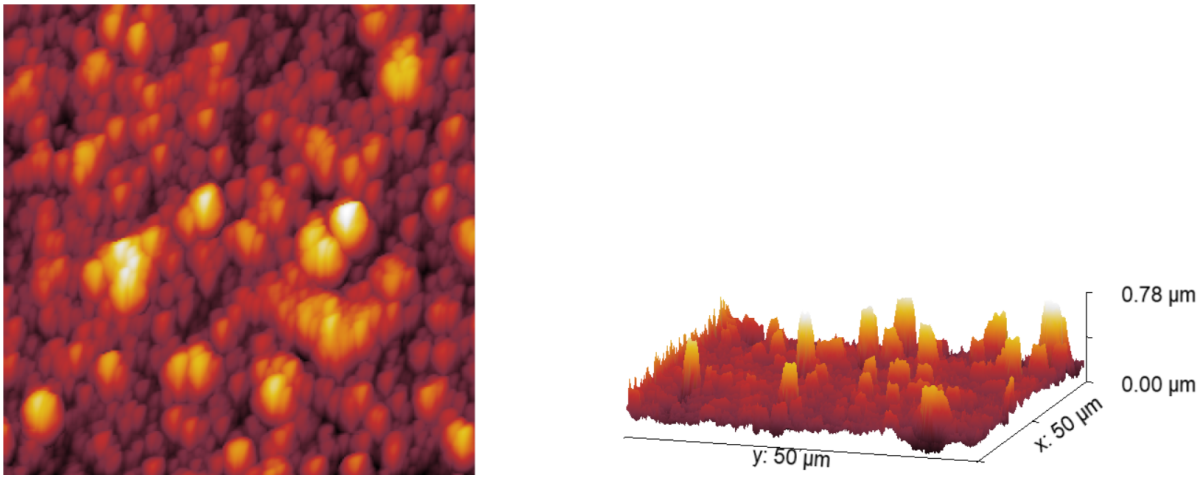

(a) 2D view

(b) 3D view

Figure 4.5: AFM

An example of the fabricated device on a die with Ti/TiN and Ta/Pt on SiO_2/Si is illustrated here:

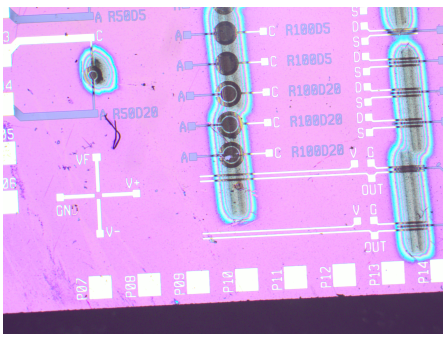

Figure 4.6: Example of printed particle and after annealing

4.2 Electrical characterization

4.2.1 SiC

The 4H-SiC PD's are 80x80 µm^2 square vertical photodiode with different characteristic. Relying on Frahunhofer IISB technology, the three different diodes lay down in a n-type layer epitaxially growth on top of a 4H-SiC. Two of them fall inside an n-well (NW) and a p-well (PW) obtained through ion implantation of nitrogen and aluminum for the NW and PW respectively. The other diode is directly created with the substrate which is technically connected to the body of the structure. An illustration is shown in *figure 4.7*. Highly doped active region has also been implanted to establish the electrical contact for metal and the cathode or anode of the diode.

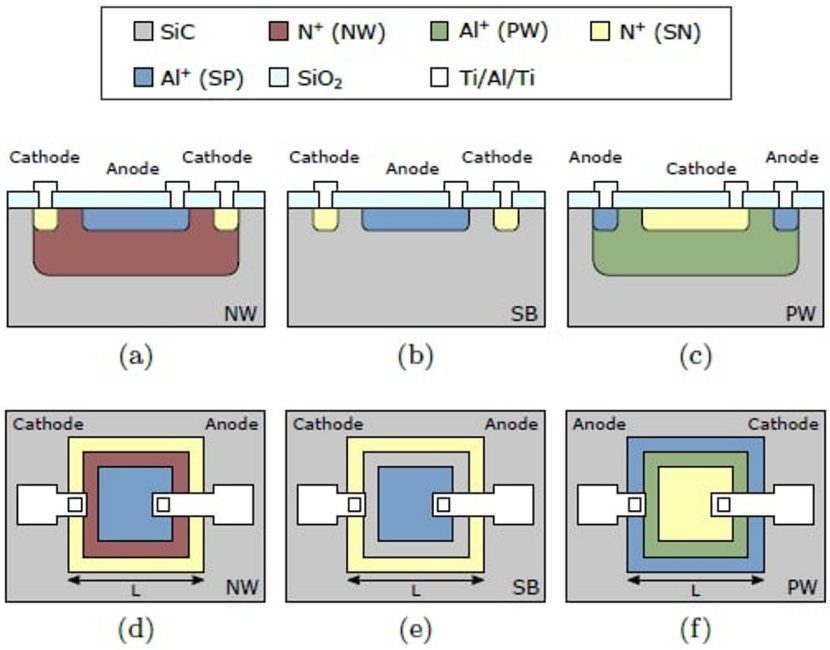

Figure 4.7: Schematic representation of the three different vertical photodiodes in the Frahunhofer IISB technology, using n-well (NW), p-well (PW), and substrate (SB). `FOR CONFIDENTIALITY REASON THIS IS A PICTURE OF A PAPER UNDER REVISION, DO NOT DIFFUSE`

The I-V curve of the photodiode is illustrated in *figure 4.7* both in dark. The voltage is applied to the anode of the diode which corresponds to the p-side, whereas the cathode is always connected to ground. The current in reverse bias is very low (the measurements been performed when the devices have been already bonded to a dual in package (DIP) for optical measurement, therefore deviation from the ideal behaviour may be taken into consideration especially in reverse bias condition where leakage current may affect the measurement), and it is mostly constant ranging from 0 to -20 V. The different doping concentration given by the well slightly cause the different switching voltage and at the same time the intensity of current flowing may vary, anyway the threshold voltage form on-off state is comparable with other 4H-SiC in literature [25].

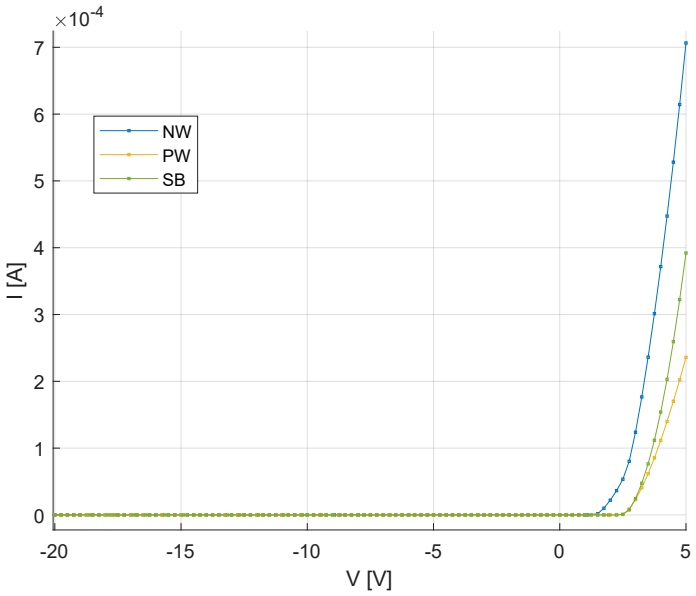

Figure 4.8: I-V curve in linear scale of the different configuration in dark condition

Moreover, a measurement when the diodes are exposed to an UVC LED 265 nm 5 mW (correctly place as close as possible to them) has been carried out. The results is that the photogenerated current under reverse bias condition is effective only when the diodes are in the off state, but when they start conducting, the current flowing is only coming from the injected carrier due to barrier lowering. The amount of light absorbed thus, the photocurrent should be approximately the same, however deviation from that are expected to happen because the light beam is not properly focused and optical power is not uniform all over the light beam angle of the LED.

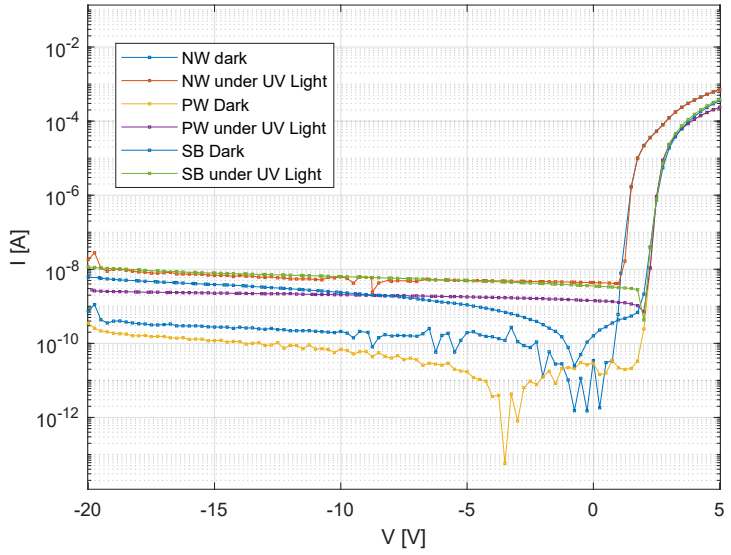

Figure 4.9: I-V curve in semilogaritmic scale of the different configuration in dark and UVC condition

4.2.2 ZnO

ZnO has been more extensively characterized starting from old samples fabricated on other types of substrates to the one described in *section 3.1* and the new ones. The mask adopted for metal patterning for old samples is illustrated in *figure 4.10*, where a simple lift off process has been executed to obtain a single metal layer based on Au. A single row has been printed on top of the ELM metal line where four point contact, repeated five times, are present, covering all of them. The electrical characterization is described in *appendix D*. A relevant aspect to appreciate is that the forming contact between gold and zinc oxide particle is ohmic while in most of the cases analysed it should be schottky [29].

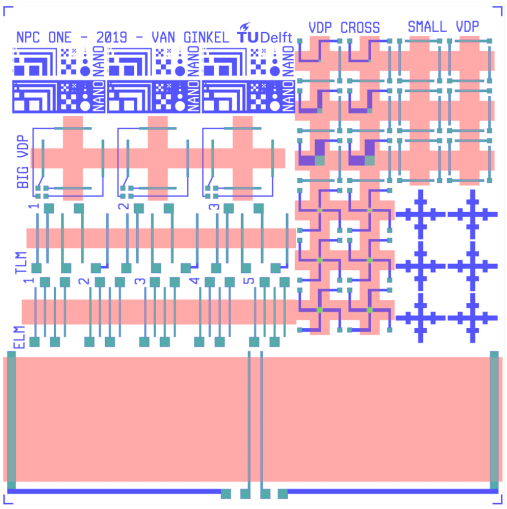

Figure 4.10: Mask for old sample devices at die level

The devices made out on the new available substrate have found to have different behavior but way far from what expected from thin film zinc oxide and what other studies report.
Indeed, after finding the right parameters to have reasonably conductive devices, a batch of samples using all the substrates available has been prepared. According to literature [13, 29], and as already aforementioned undoped zinc oxide results in intentionally n-type conductivity, therefore referring a classical schottky model an high work function metal (like Au or Pt) should form a schottky contact more than ohmic, and the opposite for a low work function metal (like TiN or Ag).
However, all the forming contact between particles and metal, properly measured through I-V curves, are unpredictable and may be different to one another, despite of the same, metals, substrate, deposition and annealing settings. There might be various reason for this. The interface depends extremely on how the particles notch the metal, thus on which atom is actually in contact with it (oxygen, zinc or other impurities),as well as barrier lowering on the interface between clusters or not. The possible presence of filament between zinc particles that creates a conductive path across the metal altering the device characteristic. The particle migration inside the film which rearrange the contact during annealing may also explain this unpredictability.
A more intense investigation must be performed to understand in a much clearer way how to have reliable and reproducible contact. Hence, the three terminal devices and more complex one (possible inverter configuration) has been abandoned, focusing only on analysing the

printed particles on two terminal device, by using the pads at the edge of each die for a better measurement (4-point probe).
An example of this inconsistency is reported in *figure 4.11*. Assuming the intrinsic negative type nature of zinc oxide, the formation of a schottky contact with TiN is practically unfeasible, or the fact that in case of MSM with TiN/Pt an ohmic behaviour shows up.

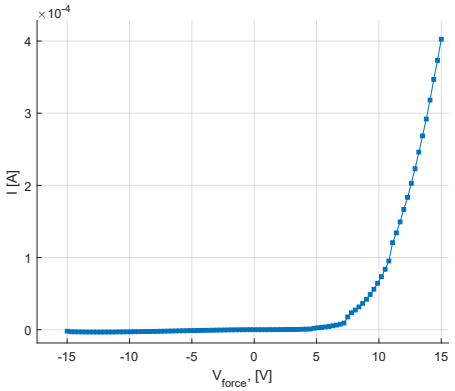

(a) Single schottky contact on TiN/Au on a fused silica

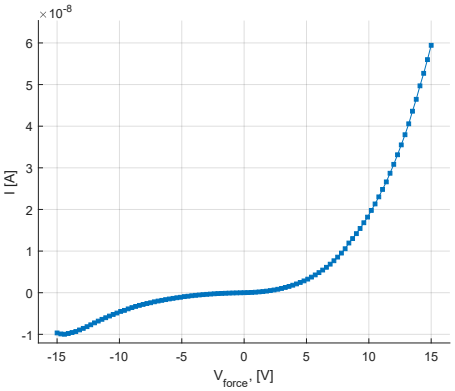

(b) Double asymmetric schottky contact on TiN/Au on a fused silica

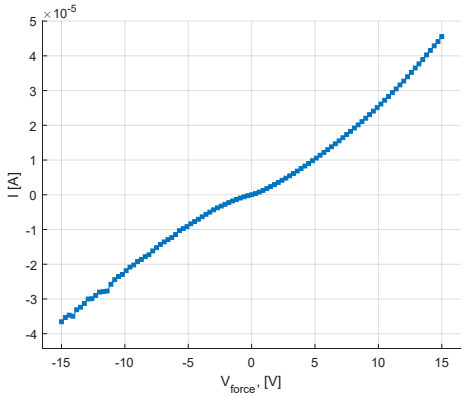

(c) Ohmic behaviour on TiN/Pt on SiO_2/Si

Figure 4.11

Despite this inconvenience, few devices on all the dies has been selected for some measurements under different external condition, for instance at 100 °C and 200 °C, with and without irradiation with visible light and ultraviolet LED at a specific wavelength. For simplicity of the analysis and discussion, photoresistors have been measured. Firstly, the measurements in dark mode with and without light has been carried out, whose data are given in *figure* **??**. In both pictures, the MSM is practically blind to visible light and decrease its resistance by at least three order of magnitude when fully charge by the UVC LED.

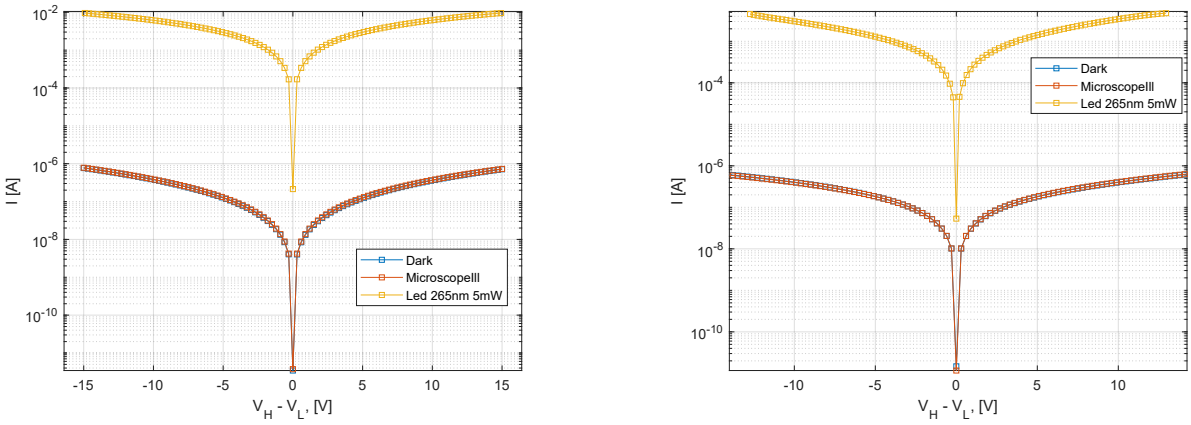

(a) MSM with Au/Ag

(b) MSM TiN/Ag

Figure 4.12: MSM devices formed in different die with different metal in semilogaritmic scale, in 4-point probe measurement, applied voltage always in metal with lowest work function, with and without light

Afterwards, the analysis in dark mode at the different temperature is given in *figure 4.13*. In this case, there are two different response. The one in *figure 4.13b*, represent behaviour of the photoresistor as also shown in all the other dies except for the one with Au/Ag on SiO_2/Si. Temperature lowers the energy gap of the zinc oxide inducing thermal carrier generation inside the semiconductor that are split by the applied electric field, before recombining. Higher temperature implies higher carrier excitation and hence a decrease in the resistance of the device. On *figure 4.13a*, however, while there is an improvement in conductivity, the resistance of the measured photodetector is lower when it is hold at 100 °C with respect to when it is hold at 200 °C, which is not consistent with the other results. A possible cause may be that, while electrons jump from valence to conduction band, at the same the lattice vibration generated by thermal heating, increase the scattering in the structure reducing then the electron and on hole mobility, an thus contribute to increase the resistivity. Anyway, if that would be the case then this would also happen in the the other devices. No clear reason is therefore conferring a reasonable explanation to this phenomenon, which is even more noticeable by looking at the resistance values reported in *figure 4.14*. The same characteristic curves is given under illumination condition, only the effectively current intensity depending if the zinc oxide absorbs is or is not under irradiation.

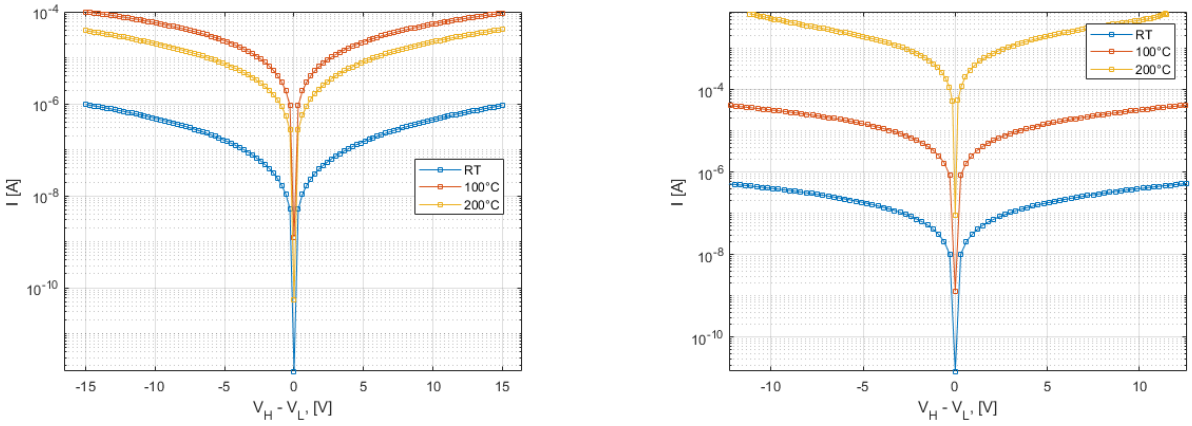

(a) MSM with Au/Ag **(b)** MSM with TiN/Ag

Figure 4.13: Devices coming out from same electrodes in different die with different metal in semilogaritmic scale, in 4-point probe measurement, applied voltage always in metal with lowest work function

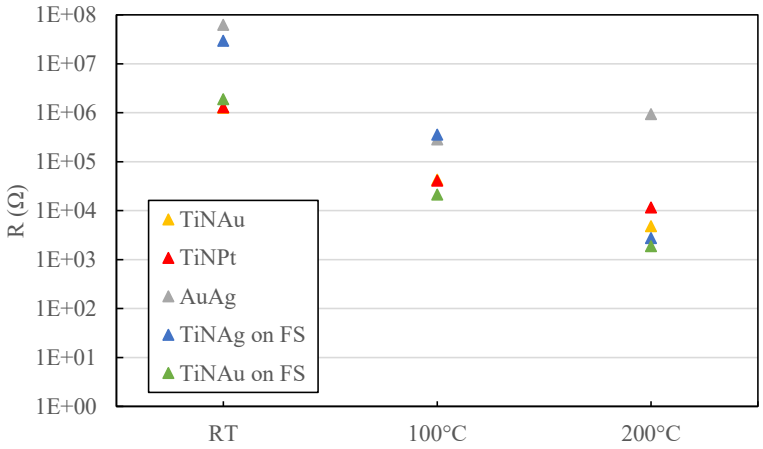

Figure 4.14: Resistance of R75D20 metal semiconductor metal

Performing both the described previously analysis in simultaneously on the MSM created in correspondence of the R75D20 device, we obtained the data in *figure 4.15*, *4.16* and *4.17*. We may state that all device may be functional for their purpose also at 100 °C where the gain due to photogeneration with respect thermal generation is still effective and at least one order of magnitude. At higher temperature, however, such as at 200 °C, the role of the fabricated PD's is not more accomplished since the difference resistance values both in dark and UVC exposure is negligible. This means that the thermally generated charge carriers are saturating in the film. As last, all the I-V curves in all the situation is illustrated in *figure 4.33*

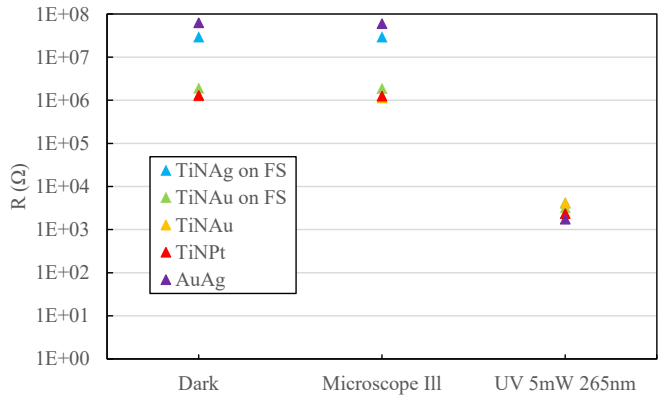

Figure 4.15: Resistance of MSM device at RT

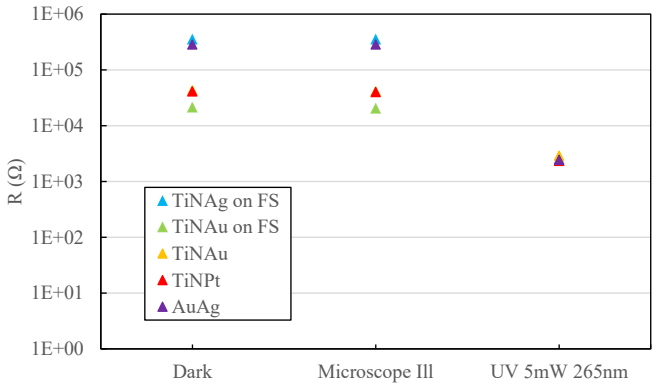

Figure 4.16: Resistance of MSM device at 100 °C

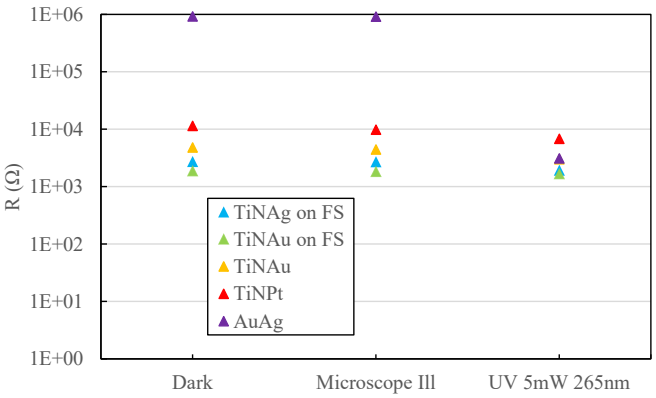

Figure 4.17: Resistance of MSM device at 200 °C

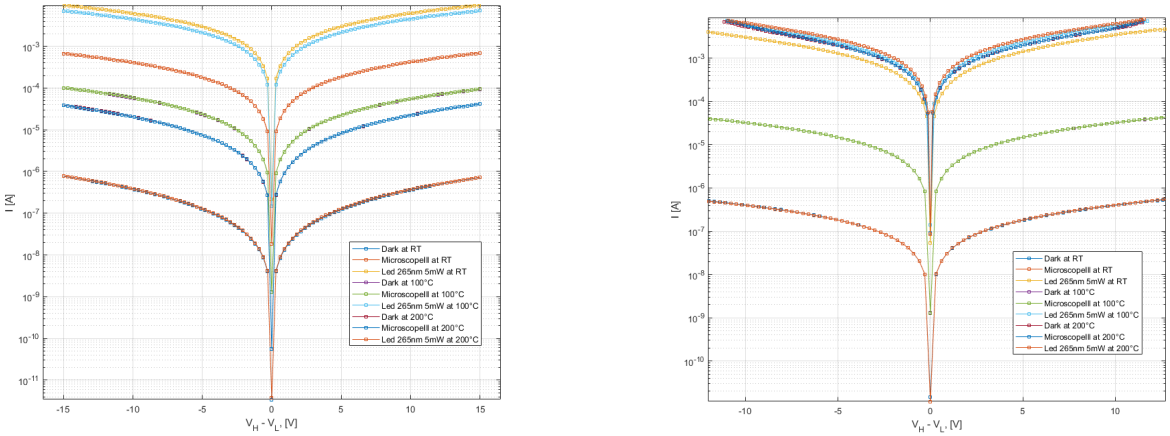

(a) MSM Au/Ag **(b)** MSM TiN/Ag

Figure 4.18: Devices coming out from same electrodes in different die with different metal in semilogaritmic scale, in 4-point probe measurement, applied voltage always in metal with lowest work function

4.3 Optical characterization

The optical characterization consists mostly on the evaluation of two main features: the response time and the responsivity $\mathcal{R}(\lambda)$, which is related to the quantum efficiency of the sample. As already described in *section 2.2*, the responsivity is defined as the ratio between the photocurrent and the optical power reaching the surface of the DUT. With the set-up used, depicted in *figure 3.13*, the only measured value is the wavelength dependent output voltage appropriately converted in current through the circuit described in *appendix B*. Therefore, a PD with well known responsivity has to be measured so that after extracting the output voltage we retrieve the optical power by the inverse formula, so that the given result is used as for all the other detector. Careful consideration was done to choose the best reference photodetector. Three photodiodes were available: Si PDA10A2 from Thorlabs [54], a SiC from Frahunhofer [55] and SiC SG01M from sglux [56]. The responsivity provided by the part are shown below:

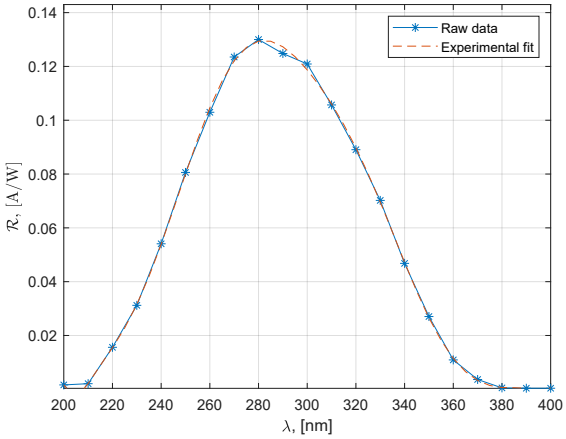

Figure 4.19: SiC FRH, each data point taken out through related paper point by point [57]

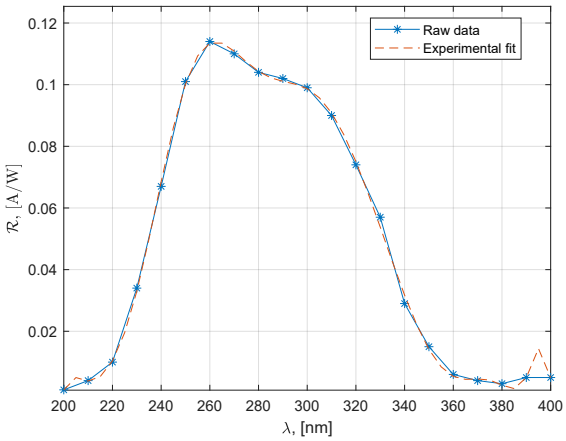

Figure 4.20: SiC SG01M, each data point taken out through the datasheet point by point

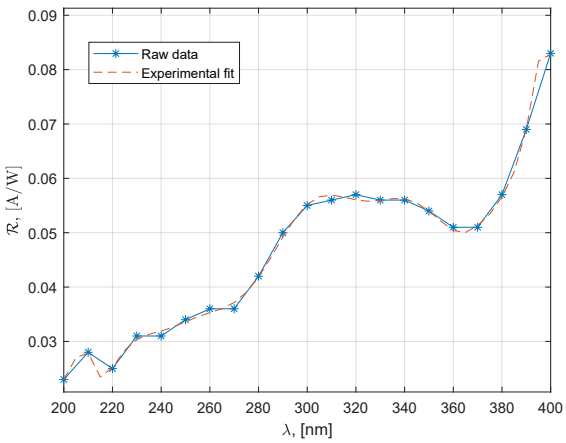

Figure 4.21: Si PDA10A2, raw data provided by the company

The Si-PD was already mounted in a solid package with a proper read out circuit incorporated despite the other two detector. The output voltage measured with relative standard deviation is given in *figure 4.22*:

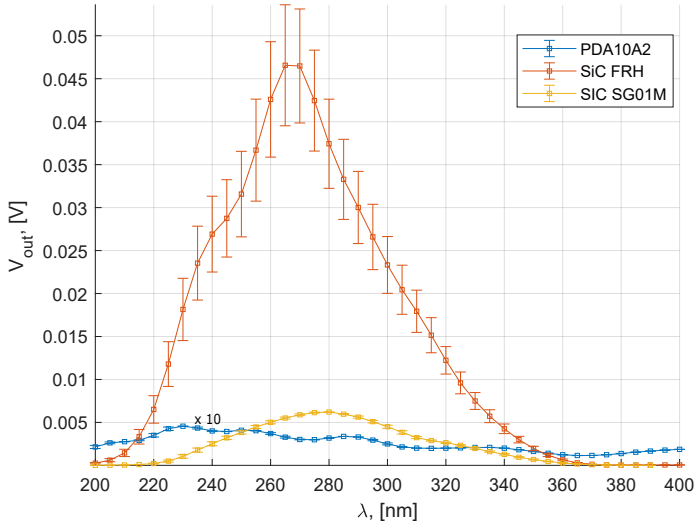

Figure 4.22

therefore the relative optical power may be expressed:

$$P_{\text{out}}(\lambda) = \frac{V_{\text{out}}(\lambda)}{R_f \mathcal{R}(\lambda)} \frac{A_{\text{Ref}}}{A_{\text{DUT}}} \tag{4.1}$$

where R_f is the feedback resistor of the transimpedance amplifier, A_{Ref} and A_{DUT} are the active area of the reference detector and device respectively. The area of the PD's given are $0.8\,\text{mm}^2$, $1.6\,\text{mm}^2$ and $0.2\,\text{mm}$ for the Si PDA10A2, SiC FRH, SiC SG01M respectively. The $R_f = 10\,\text{k}\Omega$ and $R_f = 1\,\text{M}\Omega$ for the Si PDA10A2 and the others remaining two respectively, with a reversed bias condition of $5\,\text{V}$.The derived optical power normalized with respect to the silicon photodetector is then:

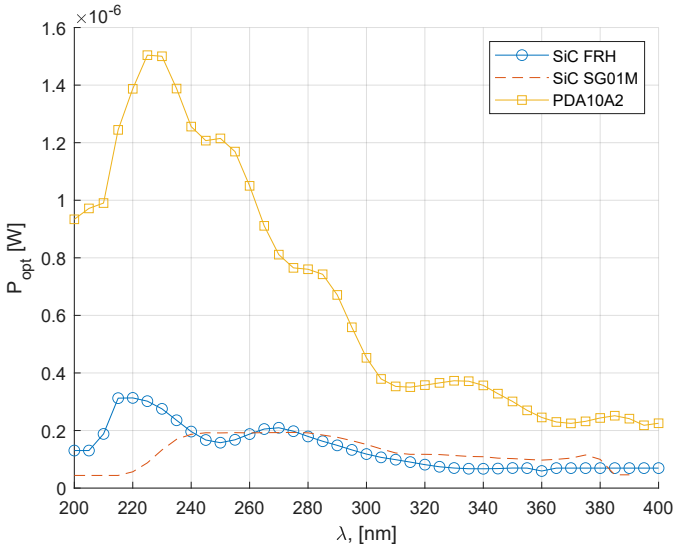

Figure 4.23: Optical power

It would be expected that the optical power is sample independent however the intensity is not coherent. The first thing to observe is that fact that all of them follows has the same behaviour as the intensity of the deuterium lamp used, where slightly change in behaviour are given to the loss of the mirror which has a wavelength dependent reflectivity. However, the inaccuracy of the raw data extracted by hand of the SiC SG01M also because the effective response is within the range [215,385] nm and will not be sufficient for the spectral range of interest. It has been discarded then.
The SiC FRH although may be chosen among the remaining two, has been also rejected. The reason is that the reference responsivity data referees to a SiC photodiode coated with 360 nm SiO_2 layer whereas the one measured has 700 nm SiO_2 thick passivation layer. Through the reflectivity effect of an ARC as discussed in *appendix C*, the different reflectivity, as shown in *figure 4.24* may partially deviate the expected output response.

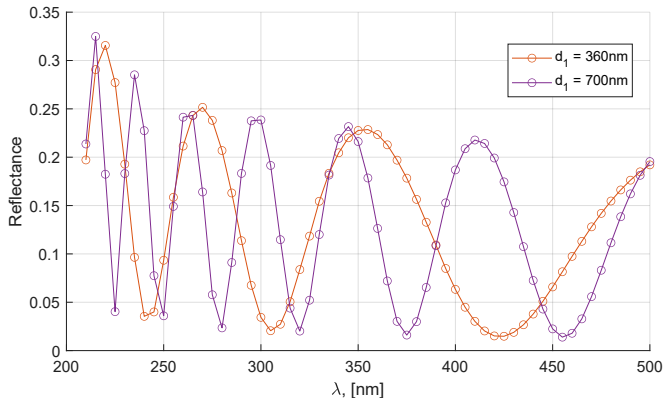

Figure 4.24: Theoretical behaviour of light across 3 layer stack

Hence, the optical power is given by the Si PDA10A2.

4.3.1 SiC

The responsivity curves of the SIC photodiodes are illustrated in *figure 4.31*. All the measured diodes were done in reverse bias condition with the cathode at 5 V and a feedback resistance of 1 MΩ. In case of a diode in a p-well, the substrate has been also biased at 20 V.

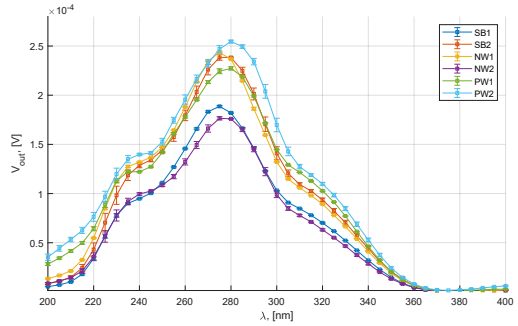

(a) Output voltage versus wavelength

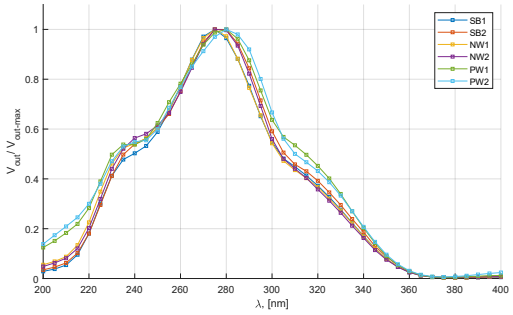

(b) Normalized measured output voltage

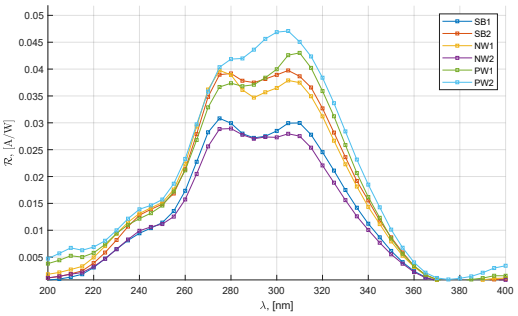

(c) responsivity of the

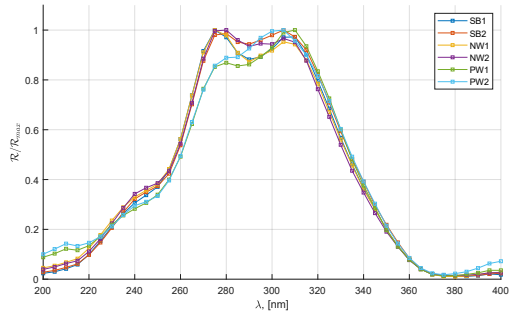

(d)

Figure 4.25: Response of NW, PW and SB where the label indicate devices attache to different packages

figure 4.25a and *4.25b* illustrate the intensity output signal and the normalized curve with respect to the maximum measured value. *figure 4.25c* and **??** reports the respective responsivity and the normalized curve, according to the inverse of *equation 4.1*

$$\mathcal{R}(\lambda) = \frac{V_{\text{out}}(\lambda)}{R_f P_{\text{out}}(\lambda)} \frac{A_{\text{Ref}}}{A_{\text{DUT}}} \tag{4.2}$$

Despite the photodiode share similar electrical characteristic, the responsivity values are inconsistent even for the exact same diode place in the different packages. The reason is that the collimated beam covers an area which is way larger then the device itself, with an optical intensity that follows a Gaussian distribution all over the selected area, this would be the main drawback for all the responsivity curves reported. Hence, the real intensity is unknown, and also their correlated effective quantum efficiency. Other important aspects still be appreciated. All the curves follows the same behaviour, where a peak around 275 and 285 nm may be present, around which the signal remain almost constant.
Mostly the n-well and substrate share a common response while the p-well has a slightly different shep with a peak towards higher wavelength.
The selected spectral range represent also the range in which the photodiode will have an

effective response, as well as in agreement with the cutoff wavelength of bulk SiC, arises from the given by the energy gap in *table 2.4*.

4.3.2 ZnO

4.3.2.1 **Energy gap** ZnO

A total transmittance analysis has been performed in order to derive the cutoff wavelength and justify the choice of measuring the spectral response in the selected range. One die (2.2x2.2 mm boro-aluminosilicate glass, Corning) has been fully covered by Zn particles, during a long deposition process to reach the highest film uniformity, and then annealed at 400 °C for 5 hour for a full oxidation. The thickness of the given layer is approximately, t=200 nm, as also reported by *figure 4.26*, of course the accuracy is rather feeble given the surface roughness.

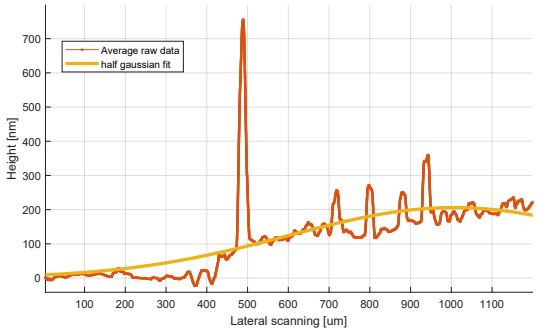

Figure 4.26: Profile of ZnO on top of corning glass

The transmission result is given in *figure 4.27*. There is an explicit difference between a reference die and the on with ZnO coated. Light start being absorbed in the expected range remaining stable until at lower wavelength also the substrate start playing a role in absorption in deep UV. It would be expected an higher absorption percentage dropping to lower transmission values. However, owing to the porosity of the particle layer and the thickness, the results are still acceptable.
Due to the wide spectral range and low number of the data point measured it is difficult to retrieve an approximated energy gap of particle based zinc oxide. Another measurement with a reduced spectral range, where there is a clear difference between the substrate and the active layer but with highest sampling rate has been performed to improve accuracy.

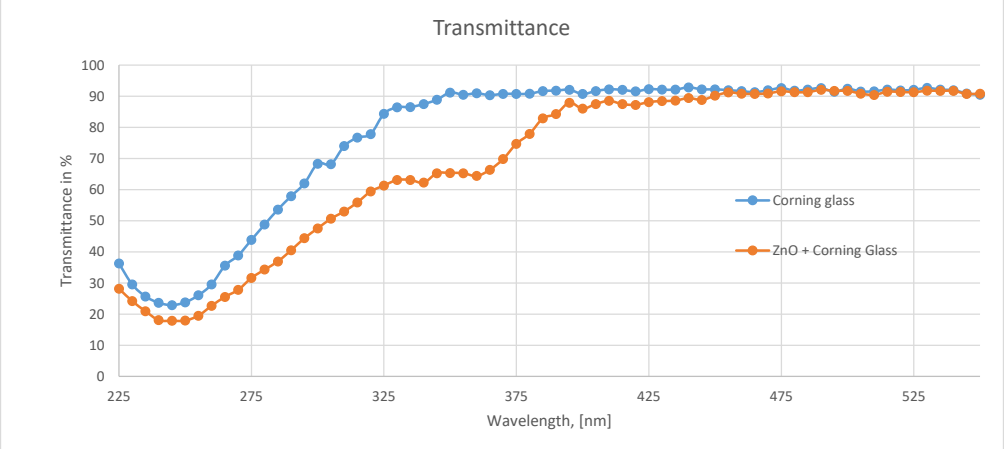

Figure 4.27: Transmittance in the range [225,550] nm (the minimum point is given by the limit of the tool)

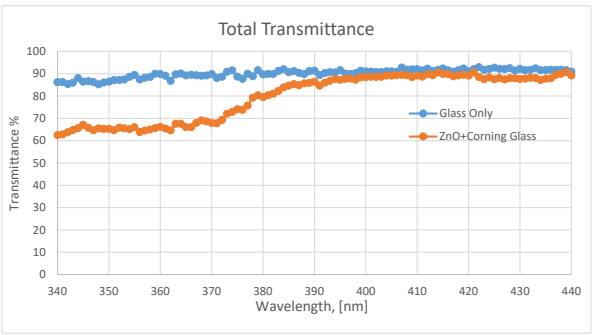

(a) Transmittance in the range [340,440] nm

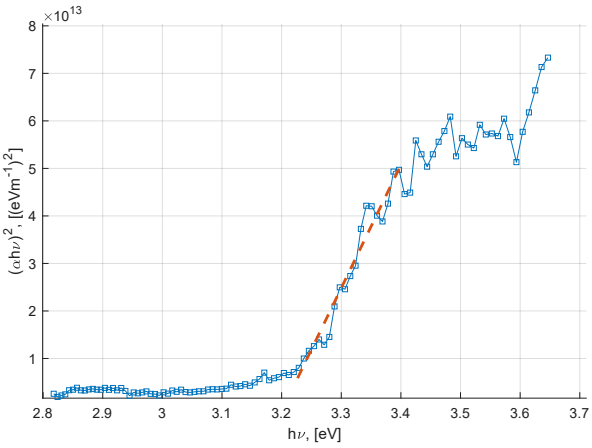

(b) Absorption coefficient vs photon energy, with a linear fitting curve in dashed line

From the data, plotted in *figure 4.28a*, it is possible to derive the absorption coefficient, following a straightforward procedure [58, 59] Treating our layer as a polycrystalline film, this is evaluated through:

$$\alpha = \frac{1}{t} \ln \left(\frac{100}{T(\lambda)} \right) \tag{4.3}$$

We can then retrieve the absorption spectrum as illustrated in *figure 4.28b*. The plot can be correlated to the E_g of the material under examination using

$$(\alpha h\nu)^2 \propto \sqrt{h\nu - E_g} \tag{4.4}$$

We may assess the value of the energy gap with at the sharp edge absorption using linear approximation ($y = a_1(h\nu) + a_2$) and finding the point where the fitting curve intersect the energy axis.

$$E_{g-\mathrm{ZnO}} = -\frac{a_2}{a_1} \tag{4.5}$$

obtaining that the energy gap at RT is approximately $E_g = 3.21\,\text{eV}$. This results is partially in agreement to what expected. Bulk or monocrystalline thin film show an energy gap around 3.37 eV, which is fairly close to the one derived. It would expected an higher value because nanoparticle material, due to the reduction in size entail an high energy gap [60, 61]. Maybe due to the presence of deep donor or acceptor state trapped in the energy gap consequences the a narrowing of the band gap but more experimental investigations are required for a better comprehension. Anyhow, this result verify the complete VIS blindness of the porous ZnO PD.

4.3.3 Old Samples

While SiC photodiode have intrinsically extremely high response speed, the charging and the discharging time of zinc oxide PD under UVC exposure is huge. The response time of the MSM photoresistor of the MSM photoresistor is illustrated in Figure 6 in *appendix D*. The t_r and t_f, reported still in *appendix D* has been properly extracted as shown in *figure 4.29a* and *4.30b*, respectively.

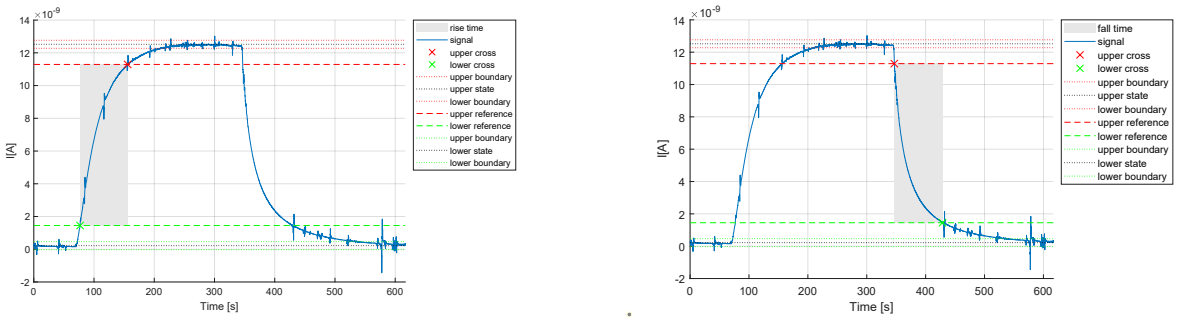

(a) rise time model **(b)** fall time model

The given operational bandwidth is then $BW = \frac{0.35}{t_r} = 4.4 \times 10^{-3}\,\text{Hz}$, which means that the only mode of operation is in direct contact. Although the electron and hole movement in the ZnO may experience several scattering mechanism such as scattering grain (grain) μ_g, scattering lattice μ_l, and (at low temperatures), as onized impurity scattering μ_{ii} [59], with a consequent high mobility degradation, likewise reported in more detailed in *subsection 2.1.1.1*, it is not sufficient to explain these long process *section 2*. The most probable phenomenon happening is that the surface conduction mechanism is affected by the absorption or desorption of chemisorbed oxygen [59], especially due to the porosity of film, the oxygen absorption whcih may also migrate in the crystal [62], enhancing this side effect.

Given the low bandwidth of operation, the responsivity measurement were performed in DC mode instead of AC, with a long waiting time between the switch between one wavelength and the following one (at least a minute to fully charge the MSM structure). A comparison of a fast and slow responsivity measurement in DC is shown in *figure 4.30*.

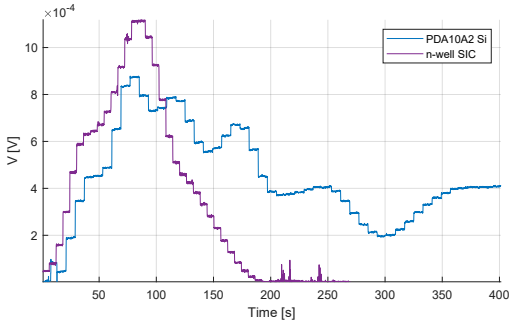

(a) Fast response time of Si and SiC photodiode

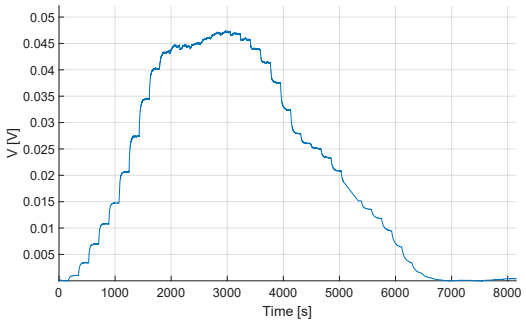

(b) Slow response time of ZnO photoresistor

Figure 4.30

While for the first picture the signal follows a piecewise step function where at each wavelength change the signal goes suddenly to the new state, in *figure 4.30a*. For instance the, carrier lifetime in the SiC is low, due to the high crytal purity. The other follow an RC step function with a very slow time constant. Given the mode of operation, to evaluate only the effective response of light, the voltage in dark mode has been subtracted to the voltage dependent behaviour ($V_{out-eff}(\lambda) = V_{out}(\lambda) - V_{Dark}$). The responsivity of three PD, where the only difference is the spacing between electrode, which is increased firstly twice and then three times, is then shown below. The circuit is biased at 5 V and the bias resistor at 10 MΩ.

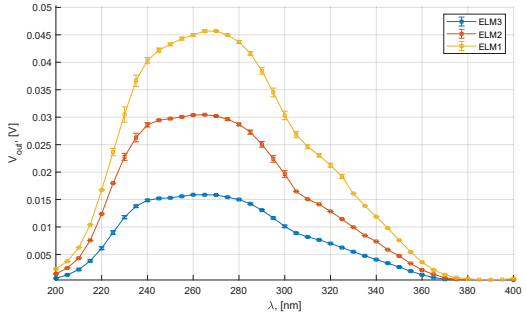

(a) Output voltage versus wavelength

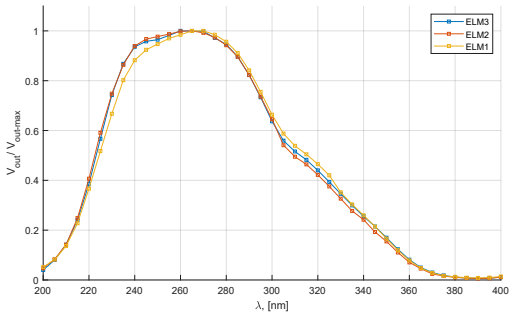

(b) Normalized measured output voltage

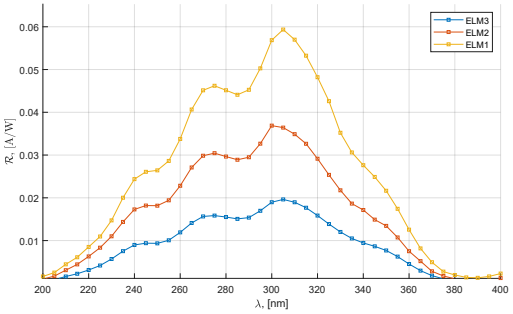

(c) Responsivity

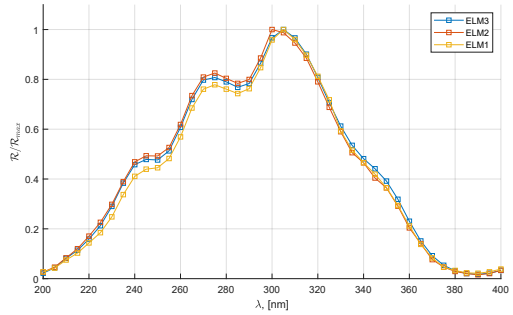

(d) Normalized responsivity

Figure 4.31: Response of ELM multiple photoresistor, where ELM1, ELM2, ELM3 is the one with lower, middle and higher electrode distance respectively

The same consideration done in *section 4.3.1* may be asserted. For instance the given

intensity is not effective one, but give an interesting information about the uniformity of the film in the given range of analysis. Indeed, the intensity decreasing as the spacing inter-electrodes, L increase with same ratio (when the L double also the output voltage becomes the half) (since the $R_{opt} \propto L$, and drop in output voltage $V_{\text{out}} = \frac{R_b}{R_b+R_{\text{opt}}(\lambda)}V_b$). The photoconductor respond i different way to light all over the UVB and UVA region. The effective shape of the curve, above 300 nm might not be accurate enough since all the contribution in light reflection given by the substrate will have a bigger role as pointed out in *appendix C*.

4.3.4 New Samples

Th fabricated sample on fused silica has been investigated for the reasoning reported in *appendix C*. As for the previous cases the response time is huge regardless of the of resulting devices. Therefore, the same methodology has been carried out.
Moreover, it has been noticed that highly conductive photoconductor (low resistance device) on the MSM structure both with TiN/Au or TiN/Ag electrodes results in bad photodetection properties. Indeed, the response time is immeasurable beacuse once the sample is exposed to ultraviolet light, it will require more than 1 hour to charge. There are no physical explanation so far understood for this aspect. Moreover the photo-conduction gain is extremely low if compared to devices with an highly resistive state. the responsivity also does not have any physical meaning or the result are extremely incoherent.
An example of these phenomenon, on a MSM photoconductor on TiN/ Ag is reported in *figure 4.32*, where the bias resistor has been set to 10 Ω in order to be at least 1 order of magnitude lower than the photoresistor:

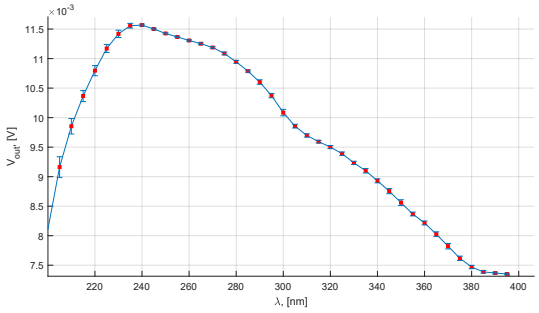

Figure 4.32: Voltage response vs wavelength where V_{Dark} has already been subtracted

As may be appreciated, there is a variation with respect to the impinging light, but after reaching a certain value, it slowly decays over wavelength without falling down to its original state as it should be since the zinc oxide is insensitive to wavelength above 380 nm. Moreover the internal gain should higher according also to the other ELM MSM photoconductor. All the devices showing this behaviour has been discarded, and other analysis are required for finding out what it is going on in the device. The only working device which shows a reasonable a comparable to the other kind of photodetector is a schottky diode TiN/Au as contact electrode. The I-V curve is shown below:

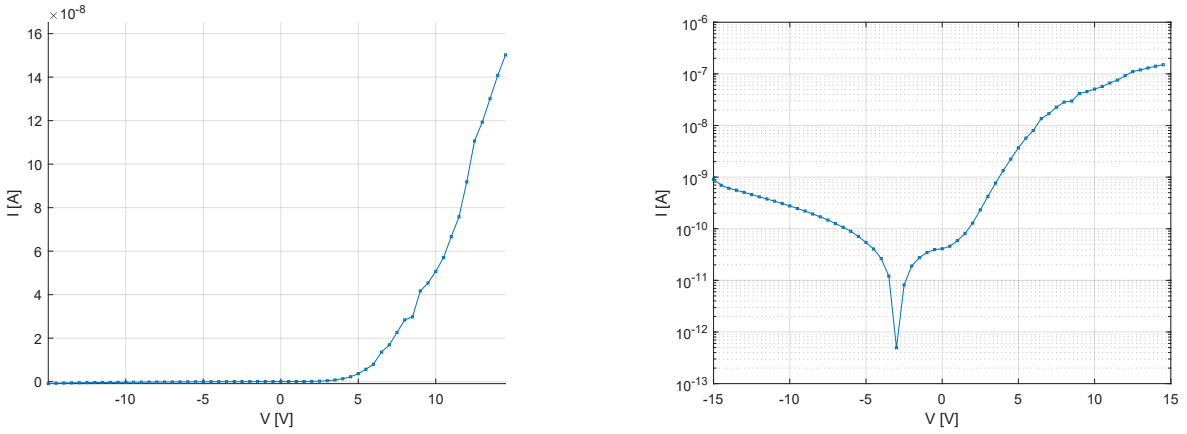

(a) **(b)**

Figure 4.33: Schottky diode on R25D5 with 4-point probe measurement, applied voltage always in metal with lowest work function

the resulting responsivity is calculated with a $R_f = 1\,\mathrm{M}\Omega$ though a transimpedance amplifier, illustrated in *figure 4.34*

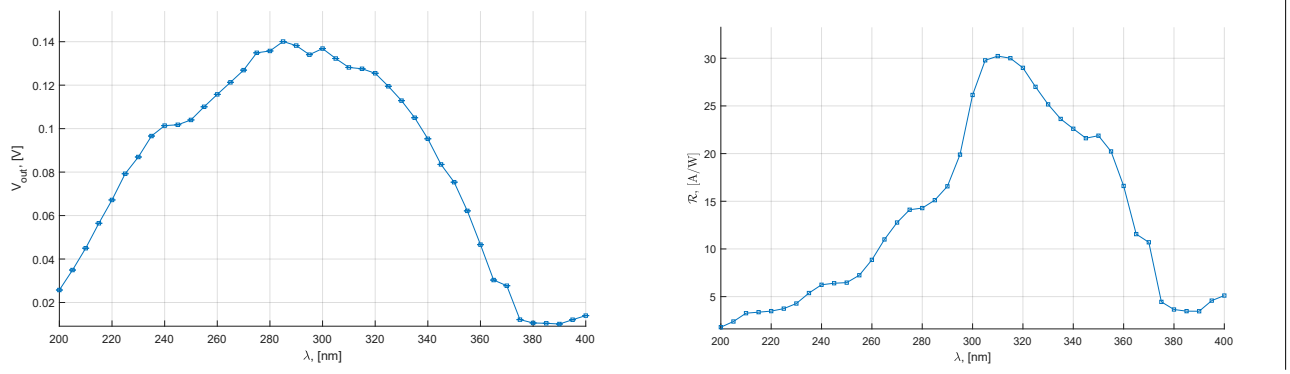

(a) Output voltage versus wavelength **(b)** Responsivity

Figure 4.34

It showed high response in the UVB-UVA region but a steep decrease is appreciable close to absorption edge of ZnO. The shape mostly depend on the intrinsic characteristic of the device, on the energy state and how electrons excited decay. The intensity may vary from the one reported depending on the intensity of the collimated beam, however it is way higher that in case of an ohmic MSM structure.

Chapter 5

Conclusion

To sum up, it has been achieved a full electrical and optical characterization on 4H-SIC photodiode and on ZnO MSM. Regarding, the first device typology, we have successfully derived the spectral range, shape and approximated intensity light response. A longer and more sophisticated analysis has been carried out for the other device. The complexity of the structure and poor crystallinity hamper any simple understanding of both conduction and optical response. The investigation on the effect of various metal and substrate was not sufficient for a clear statement on the behaviour of the zinc monoxide particles. We, although, demonstrate that, according to the simple fabrication process required, the photoconductive gain under UVC exposure is at least three order of magnitude, the device are blind to all the wavelength above 400 nm, with a reasonable response in the spectral region analysed, comparable to other device. Moreover, they may operate still correctly even in high temperature 100 °C The only detrimental effect would and remain the slow response speed, which circumvent the use of this kind of PD in many application.
For future analysis, It would be useful understanding the deposition and temperature effect on the fabricated device, for creating three terminal device or even other structure, with aim of a reproducible and reliable procedure for ultraviolet photodetector. Moreover, improvement in the tool would be necessary to circumvent the problem found during the characterization such as the effective quantum efficiency and related parameters (NEP, D^*).

Appendix A

Silver dewetting

The effect temperature on the metal revealed various drawbacks for ZnO tempering. Firstly, 100 nm thickTiN starts oxidizing above 500 °C regardless the amount of annealing in a N_2 environment and at the same time even a long tempering at 400 °C in the exact same condition results in a partial or complete oxidation. Indeed above 5 hours the oxidation results a complete or at least total film coverage (the TiN become from a brownish color to a greenish/bluish one). 5 hours would be the maximum allowable time that that results in a very thin oxide layer, while the inner part remain unaffected. The oxidation rate at 400 °C is way lower then at 500 °C, acting as temperature threshold for the preservation of the film.

Another very particular and rare effect is the dewetting of thin silver film. On very tiny layer, depending on the substrate, silver atoms experience a migration under different temperature and time setting. The basic physical relies on the surface minimization of the layer, condensing with different shapes (such nanorods, nanovalleys) [63]. During annealing it has been noticed that substrate hold at 400 °C for more than 5 hours, undergo this process followed by a drastic decrease in conductivity, since the forming structure are no longer forming an uniform structure. The same phenomenon results when the substrate even at 500 °C for more than 1 hour. The resulting structural morphology, formation of microball all over the film, is depicted in *figure A.1*, under two different condition:

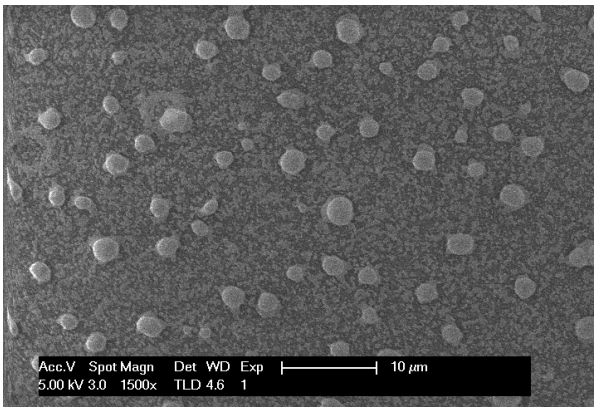

(a) Annealing at 400 °C for 5 hour

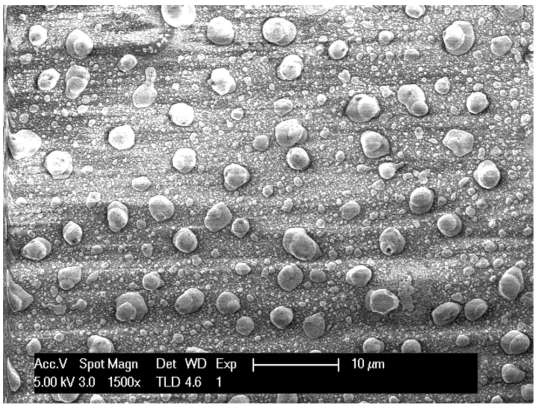

(b) Annealing at 500 °C for 1 hour

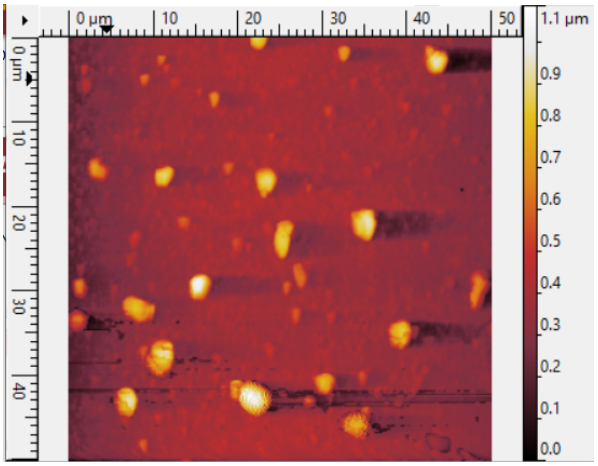

(c) Annealing at 400 °C for 5 hour

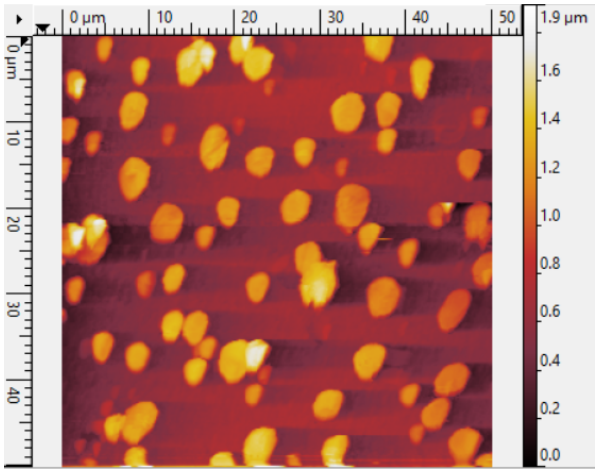

(d) Annealing at 500 °C for 1 hour

Figure A.1: AFM and SEM pictures on glass substrate, where on the latter wobbling due to charge up effect shows very wavy feature in correspondence of the micro ball

Appendix B

PCB Design

The setup, described in *section 3.3* and schematically illustrated in *figure 3.13*, requires an optimal read out circuit to convert the photogenerated current in voltage. Beneficial to accomplish this task, a dedicated PCB has been designed and produced to have a stable component for the measurements which eases the measuring process. Indeed this choice guarantees lower noise contributing from connection and a more robust signal routing, as well as avoiding that the external jumper deflects or partially covers the light beam properly focused on the DUT.

B.1 Read out mechanism

Depending on the type of devices to be measured different circuit can be used. We are going to give an hint of the possible read out circuits.

B.1.1 Photoconductor

The photoresponse of photoresistor is generally accomplished by implementing a voltage divider, in the less complex way, or a wheatstone bridge configuration. In the first case, as shown *figure B.1a*, the device is connected in series with an appropriate resistor, selective chosen so that $R_\lambda \gg R_b$. The voltage is measured across the fix resistor, and the change in conductivity of the PD will induce a increase in the output voltage. Anyhow, the environment condition will affect the measurement, so that the accuracy may not be the most reasonable one. The wheatstone bridge circuit, reported in *figure B.1b* is an electrical bridge consisting of two branches of a parallel circuit connected to the inverting and not inverting input of an operational amplifier and used for determining the value of an unknown resistance in one of the branches. Therefore, it exploit the basic principle of a voltage divider, but in this case, three other specific resistor are selected to have a null detection, i.e. the ratio of the resistors are equal and no current flows through it, and to properly get rid of noise and other parasitic effect, allowing the user to independently set the output offset level.

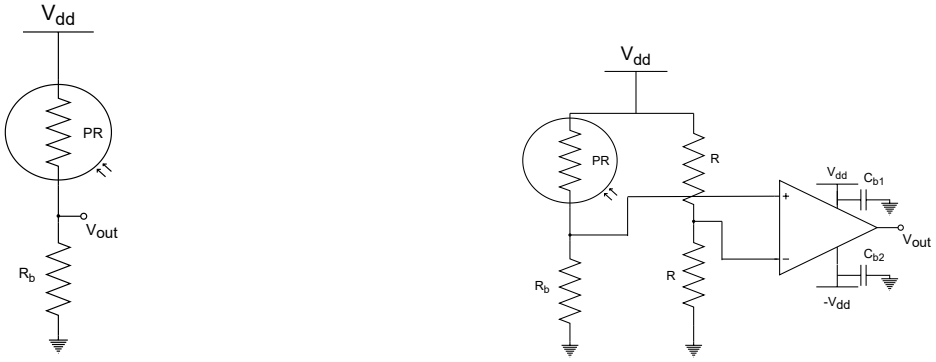

(a) PD in a voltage divider

(b) PD in a wheatstone bridge

Figure B.1

B.1.2 Photodiode

All the p-n junction and related devices (avalanche photodiode, schotty diode, pin junction...) require the use of a transimpedance configuration. The photodiode can be operated with or without an applied reverse bias, positive voltage on the n side of the junction depending on the application specific requirements. Biased or unbiased are referred as photoconductive or photovoltaic mode respectively.

B.1.2.1 Photovoltaic

The most simple circuit is shown in *figure B.2*. The n-side (cathode) of the junction is connected to ground, so that the device is dark condition, and an appropriate resistor is placed in parallel to it. The carrier generated by photogeneration, split by the built-in electric field, flows across R_p causing an opposite voltage across the diode.It may be adopted when $R_p \gg R_{sh}$, shunt resistance of the diode. This implementation does not imply any complexity however the resulting output voltage is extremely dependent on the temperature condition, on the parasitic components of the diode (shunt and series resistance, depletion and diffusion capacitance), and on the operating bandwidth.

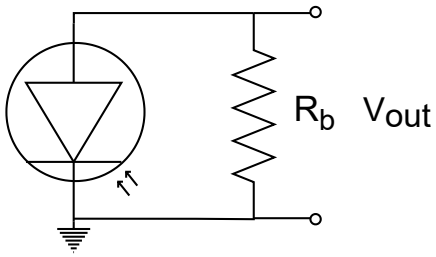

Figure B.2: PD with parallel resistor

Another photovoltaic mode of operation is generally preferred, especially when a it is used in low frequency applications (up to 350 kHz) as well as ultra low light level applications. The schematic representation is illustrated in *figure B.3*, composed of an optimal transimpidance amplifier with a compensated capacitor to hamper gain peaking. It is of better use in case of $R_f \ll R_{sh}$. It offers a fairly operational configuration and the photocurrents in this mode

have less variations in responsivity with temperature and it decouple the diode itself from the output. Depending on the type of situation and photodode under test, the anode may be connected to a negative voltage to increase the performances, taking into account the stability problem rising form the intrinsic capacitance of the p-n junction on the operational amplifier.

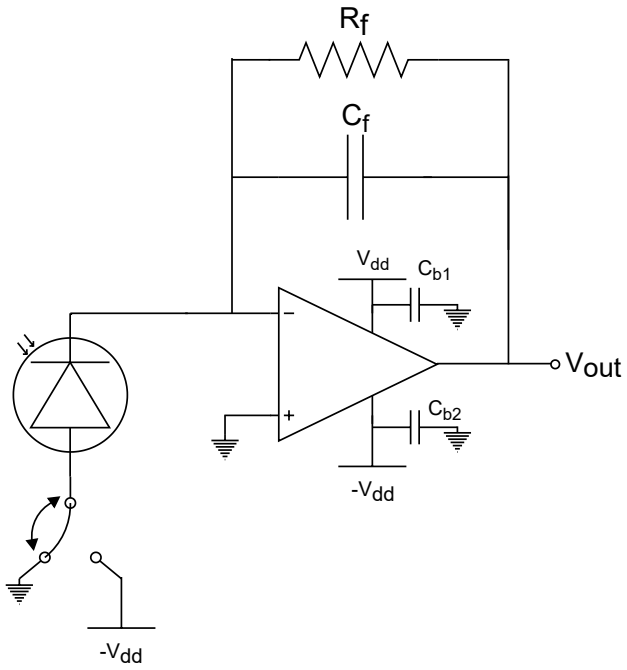

Figure B.3: PD with transimpedance amplification

B.1.2.2 Photoconductive

In photoconductive mode, the application of a reverse bias (i.e. cathode positive, anode negative) can greatly improve the speed of response and linearity of the devices. This is due to increase in the depletion region width and consequently decrease in junction capacitance, whereas this causes an increase in dark and noise currents.
In low light intensity level and wide bandwidth two stage amplification as depicted in *figure B.4*. The two stages include a transimpedance pre-amplifier and a non-inverting amplifier for voltage amplification. Gain and bandwidth ($f_{3dB-\max}$) are directly expressed by R_f, as reported in equation. A feedback capacitor (C_f) will limit the frequency response and avoids gain peaking.

$$f_{3db-\max} = \sqrt{\frac{GBP}{2\pi\left(C_J + C_F + C_A\right)}}$$

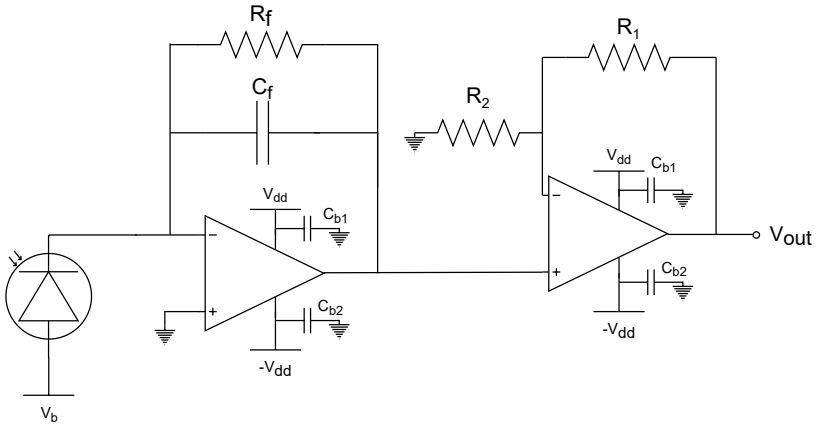

Figure B.4: PD with double stage

Anyhow, in high speed and high light level measurements, however, a different approach is generally suggested. The photodiode output can be either directly connected to an oscilloscope, *figure B.5* or fed to a fast response amplifier. When using an oscilloscope, the bandwidth of the scope can be adjusted to the pulse width of the light source for maximum signal to noise ratio. In this application the bias voltage has to be reasonably large.

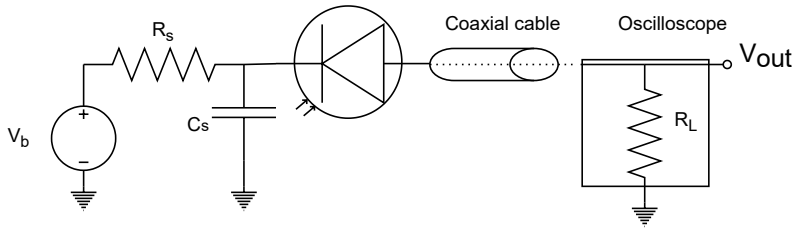

Figure B.5: PD with transimpedance amplification

B.2 Printed circuit board

Despite the possibilities to use a breadboard where routing all the connection needed for the read out circuit, a design and creation of a PCB which incorporates both read out mechanism. The chosen configuration are reported in *figures B.3* and *B.1a*, for a photodiode and photoconductor respectively. A potentiometer has been chosen instead of a resistor with fixed value in the voltage divider, with a range between 10 Ω and 10 MΩ, in order to tune the gain according to the resistance of the DUT and the output node is branched to a voltage follower to convert an high impedance node into a low one.
A more sophisticated analysis has been followed for choosing the C_F and R_F in the transimpedance amplifier. Indeed, replacing the photodiode with an ideal current source in parallel with its equivalent resistance, R_D, and capacitance, C_D the transfer function can be expressed:

$$A(f) = \frac{R_F R_{sh}}{R_F + R_{sh}} \frac{1 + i\frac{f}{f_z}}{1 + i\frac{f}{f_p}} \tag{B.1}$$

with the pole and zero frequency being:

$$f_z = \frac{1}{2\pi \frac{R_F R_{sh}}{R_F + R_{sh}} (C_F + C_D)} \quad \text{and} \quad f_p = \frac{1}{2\pi R_F C_F}$$

The pole frequency, f_p, is set by the feedback network, just as in the transimpedance function. The zero frequency, f_z, is determined by the sum of the feedback and the diode capacitances and the parallel combination of the feedback and the diode resistances. The value of the parallel combination is essentially equal to the feedback resistor alone, since in case of SiC $R_{sh} \gg R_F$. Therefore, f_z will always be lower than f_p. Three different situation may verify, as shown in *figure B.6*. Stability degradation may occur when f_p falls outside the open-loop gain curve. For f_{p1} the circuit will oscillate. If f_p lies inside the open-loop gain curve, the transimpedance circuit will be unconditionally stable. This is the case for f_{p2} but stability is traded off for transimpedance bandwidth. The optimum solution paces f_p on the open-loop gain curve as shown for f_{p3}. Since f_p is chosen according to the feedback network, CF must be selected with extreme accuracy. Since the noise gain is defined by capacitance values alone:

$$A(f \gg f_p) = \frac{C_F + C_D}{C_F}$$

This value should be equal to the op-amp's open-loop gain at f_p, yielding:

$$\frac{\text{GBW}}{f_p} = \frac{C_F + C_D}{C_F}$$

Simple substitution conduces to a quadratic equation whose only real, positive solution is:

$$C_F = \frac{1}{4\pi R_F \text{GBW}} \left(1 + \sqrt{1 + 8\pi R_F C_D \text{GBW}}\right) \tag{B.2}$$

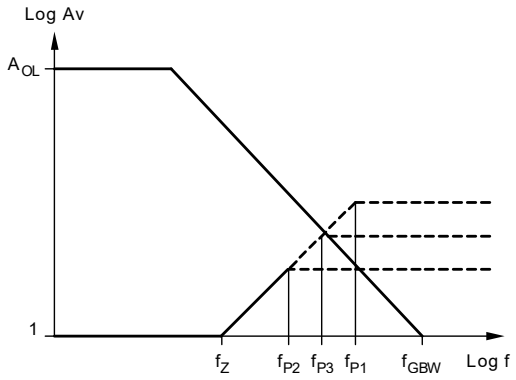

Figure B.6: Various Feedback Responses Noise Analysis Intersecting Op Amp Open-Loop Gain []

Replacing the feedbcak resistor with the exact same potentiometer to have a tunable gain, and choosing a quad high-speed precision difet OPA404 as operational amplifier, and approximately considering the parallele capacitance of a 4H-SIC, the feedback capacitor has been evaluated in the worst and best case to determine the acceptable range for picking up the correct capacitor. The final chosen components to solder are detailed in *table B.1*:

Component	IC-Sockets 40 Pin	IC-Sockets 20 Pin	IC-Sockets 10 Pin	Socket - OPamp	Power connector	Potentiometer 10 MOhm	BNC connector	SMD CF 100pF feedback capacitor	SMD Cb1/ Cb2 10nF/100nF
Characteristics	IC and Component Socket, 40 Contacts, DIP Socket, 2.54 mm, 15.24 mm, Phosphor Bronze	Pin Header, Vertical, Wire-to-Board, 2.54 mm, 1 Rows, 20 Contacts, Through Hole Straight	Pitch C-Grid III Header, Single Row, Vertical, 10 Circuits, Tin (Sn) Plating	14 Position Dual Wipe Ladder Style DIP IC Socket 0.3" Wide 0.1" Pitch	Connector, Terminal Block; Wire Receptacle; 3 Pos.; 16-30 AWG; 3,5 mm CL; Side;	Rotary Potentiometer, 10 Mohm, 1 Turns, Linear, 12 mW, ± 20%, P13	RF/COAXIAL BNC BULKHEAD JACK R/A 50 OHM SOLDER	SMD Multilayer Ceramic Capacitor, 100 pF, 50 V, 0603 [1608 Metric], ± 5%, C0G / NP0, CC Series	SMD Multilayer Ceramic Capacitor, 10000 pF/ 0.1 µF, 50 V, 0603 [1608 Metric], ± 5%, C0G / NP0, CGA

Table B.1: Components selected

The schematic, the 2D front side and 3D model are reported here in *figures B.7*, *B.8* and *B.9*. As may be appreciated, the PCB can be divided in two main parts. One where there is a DIP socket to plug and unplug the DUT where all the sockets are connected one the left and right side to male IC-sockets in order to rout through two external female jumpers the cathode and anode of the diode to the proper read out circuit (the same is valid in the other case whereas the jumpers rout the high and low node of the photoresistor). The other part is only dedicated to the read out mechanism. The spacing between the two has been accurately defined so the clamp used to hold the PCB during the measurements will fit and the DUT will be in between the clamp (as shown in *figure B.10*). Finally, both side of the printed board has been exploited so that all the jumpers will be used on the back side.

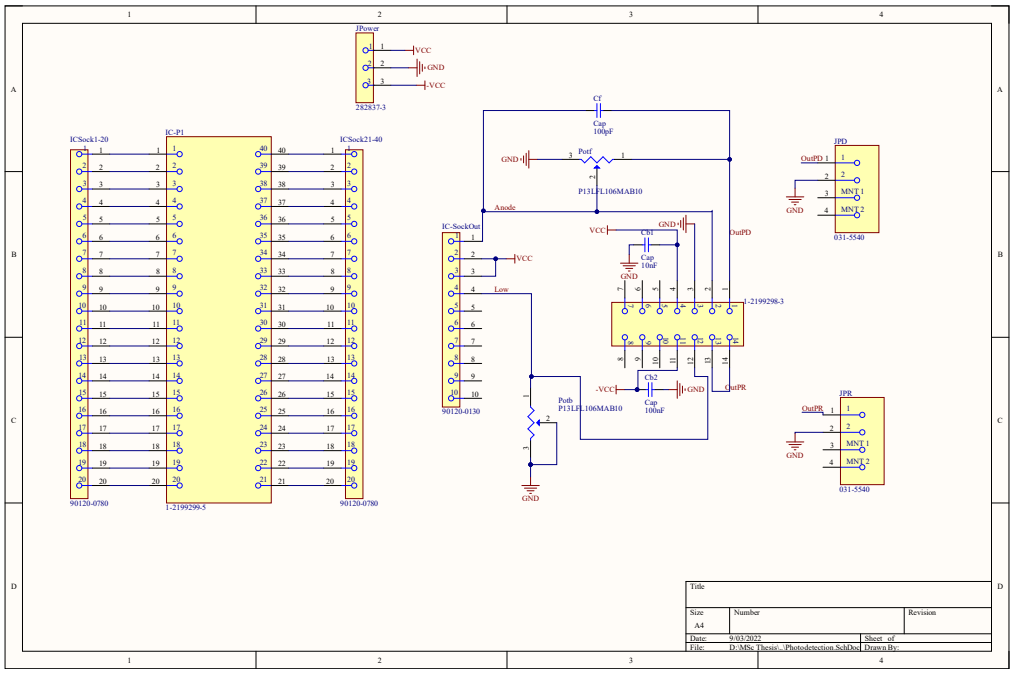

Figure B.7: Schematic of current to voltage converter circuit

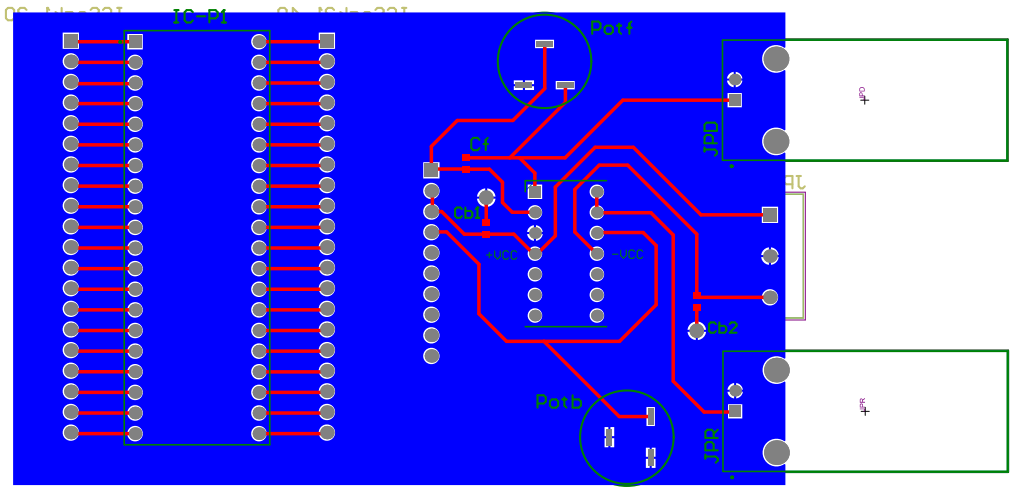

Figure B.8: 2D schematic of current to voltage converter circuit

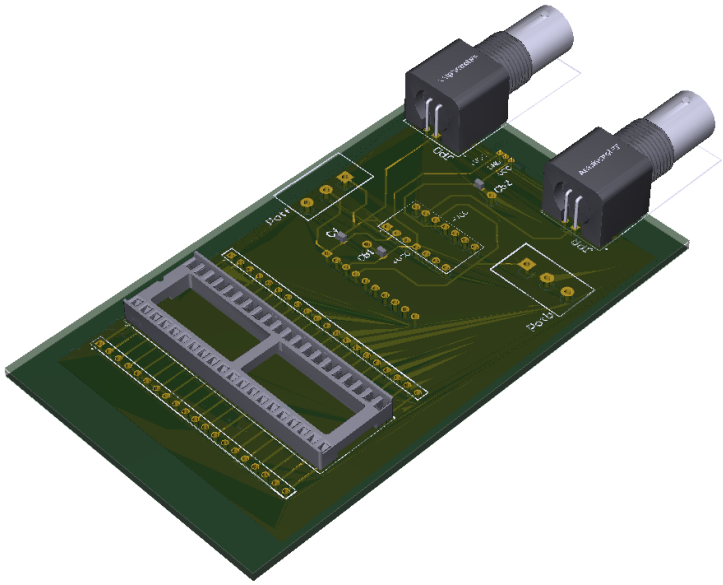

Figure B.9: 3D schematic of current to voltage converter circuit

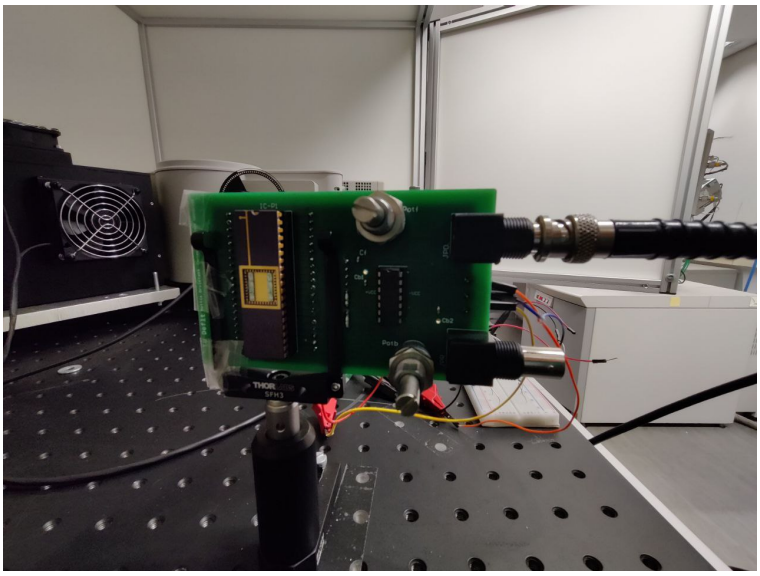

Figure B.10: Picture soldered and placed in position for a measurement

Appendix C

Reflectivity on layers stack

A crucial part of a photodetector is also given by the contribution of the layers stack present in the whole device. The interaction of incident light and a material is characterized by three optical aspects, namely: absorption, reflectance, transmittance, *figure C.1* gives a representative illustration.

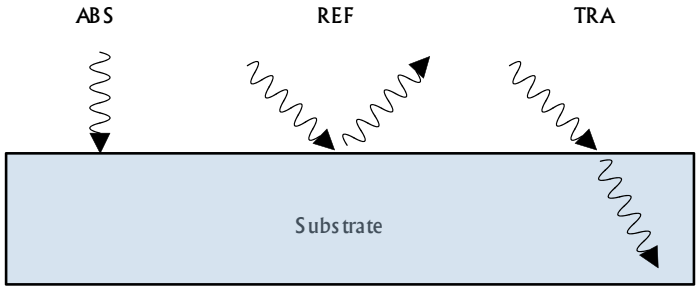

Figure C.1: Light material interaction

Materials through which light travel unhindered or with soft attenuation are defined as transparent or semitransparent, respectively. On the other hand, a material is defined as opaque when an electromagnetic wave is completely reflected or absorbed. Absorption of light is set by two components, namely: absorption coefficient (α) and its reciprocal ($1/\alpha$), defined as penetration depth. The absorption coefficient of any material indicates its ability to absorb photons at a specific wavelength, hence the absorbing layer should have a thickness at least equal or larger than the penetration depth for a given wavelength range. The part of the light not absorbed is either transmitted across the material or reflected. Light travelling from one medium into another experiences a change in propagation direction and intensities, which means that it will be subjected to refraction.

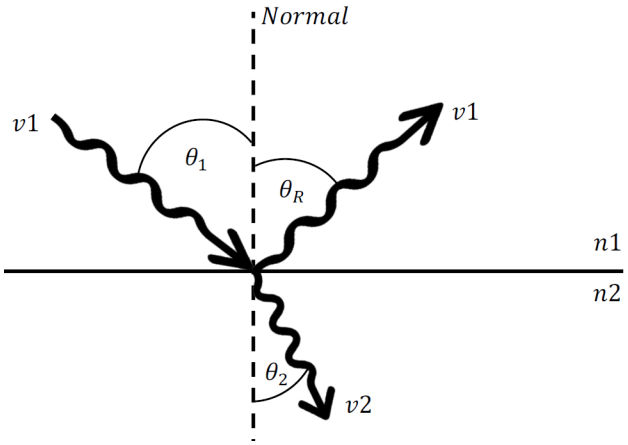

Figure C.2: Reflection and diffraction on a smooth surface

The Snell's law, correlates the speed of light in each medium with their respective angles of incidence and refraction:

$$\frac{v_1}{\sin(\theta_1)} = \frac{v_2}{\sin(\theta_2)} \tag{C.1}$$

Where v_1 and v_2 are the speeds of light in medium one and medium two, respectively, θ_1 and θ_2 are the incident and refractive angles between two different materials, respectively. By introducing the refractive index, which takes into account the difference between the intensities of light speed in a media with respect to vacuum ($n = \frac{c}{v}$), we may reformulate *equation C.1*:

$$\frac{\frac{c}{n_1}}{\sin(\theta_1)} = \frac{\frac{c}{n_2}}{\sin(\theta_2)} \quad \Rightarrow \quad n_1 \sin(\theta_1) = n_2 \sin(\theta_2)$$

The angles are taken with respect to the normal to the interface, where the law of refraction assumes that the incident and refractive rays lie in the same plane at the point of incidence. The refractive index has, close to the propagation angle, an important relation to absorption. Light will propagate and attenuate according to the extinction coefficient k. It is the imaginary part of the complex refractive index, with n as real part:

$$\tilde{n} = n + ik$$

Reflection, instead, is the bouncing of light rays from a smooth surface, without absorption or refraction.The law of reflection states that light will be reflected with the same angle as the incident angle on the surface of the material ($\theta_1 = \theta_R$) as already depicted in *figure C.2*. The reflectance, R, embodies the amount of optical power reflected from a surface. There are two cases to take into account, the s-polarized and p-polarized light, that is when the electric field is polarized either perpendicular or parallel to the incident plane, respectively. Since also the two polarized wave are perpendicular, it may be decomposed in both components, called s- and p-polarization components. The Fresnel equations which fully define the two terms are given below:

$$R_s = \left(\frac{n_1 \cos(\theta_1) - n_2 \cos(\theta_2)}{n_1 \cos(\theta_1) + n_2 \cos(\theta_2)} \right)^2$$

$$R_p = \left(\frac{n_1 \cos(\theta_2) - n_2 \cos(\theta_1)}{n_1 \cos(\theta_2) + n_2 \cos(\theta_1)} \right)^2$$

It should be noted that for this analysis the imaginary part is ignored since we are only concerned with reflection, the extinction coefficient is negligible in the discussion. Moreover, from now on, in order to simplify the analysis even more, we assume that light is perfectly perpendicular to the incidence plane known as reflection at normal incidence ($\theta_1 = \theta_R = 0$), thus the two reflectance polarization becomes identically ($R_s = R_p = R$) resulting in:

$$R = \left(\frac{n_1 - n_2}{n_1 + n_2} \right)^2 \tag{C.2}$$

Thee previous brief description took into account the interface between two material, if considering the presence of another material, with the configuration illustrated in *figure C.3*, different layer the analysis varies slightly.

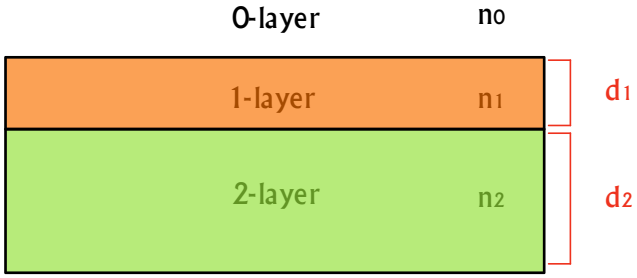

Figure C.3: Layer stack

For normal incidence illumination, the expression of the reflected energy is then given by *equation* **??**.

$$R = \frac{r_1^2 + r_2^2 + 2r_1 r_2 \cos(2\theta)}{1 + r_1^2 r_2^2 + 2r_1 r_2 \cos(2\theta)} \tag{C.3}$$

with the reflection coefficient r_1 and r_2 are:

$$r_1 = \frac{n_0 - n_1}{n_0 + n_1} \quad \text{and} \quad r_2 = \frac{n_1 - n_2}{n_1 + n_2}$$

Where n0, n1 and n2 represent the refractive indices of first, second and third layer as depicted in *figure A.1c*, respectively and θ is the phase shift of the electromagnetic wave caused by the second layer, expressed by:

$$\theta = \frac{2\pi n_1(\lambda_0) d_1}{\lambda_0}$$

where d_1 is the thickness of the second layer and λ_0 is the wavelength of light.
As shown in *figure 4.7*, also mentioned for the reference SiC and also described in detail in *chapter 3*, and detailed before, the presence of other layer beyond the detector's core may play a role in its response.
By adopting the aforementioned equations, several theoretical calculation on the reflectance of a light beam perpendicular to the device under test has been extremely helpful to understand better the responsivity of the PD and on the choice of glass substrates.

C.1 SiO_2/SiC

All the photodetector based on thin film or bulk SiC presents a protective passivation layer on top, based on SiO_2. The above defined second layer, is in this case an ARC (antireflective coating) optimally defined to reduce the reflection of the optical power at different wavelength. The reference 4H-SiC Frahunhofer IISB photodiodes characterized have an oxide thickness of 700 nm, whereas the NW, PW, and SB diodes have an oxide thickness of 50 nm. Using *equation C.3* in case of three layer, *equation C.2* for two layer and the refractive index, as function of wavelength, of material involved available in [64], the reflectance as function of wavelength in the range [210; 500] nm has been evaluated (going to higher wavelength would be out of the aim for UV's PD, and at lower wavelength no data has been found).

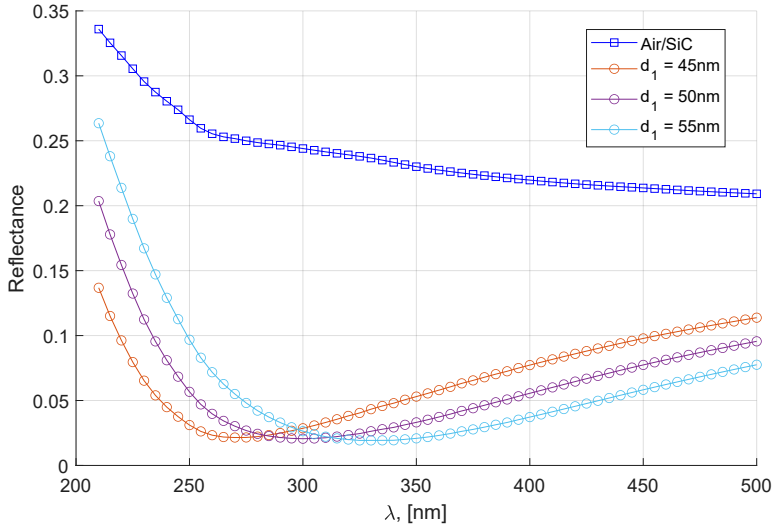

Figure C.4: NW, PW, and SB diodes

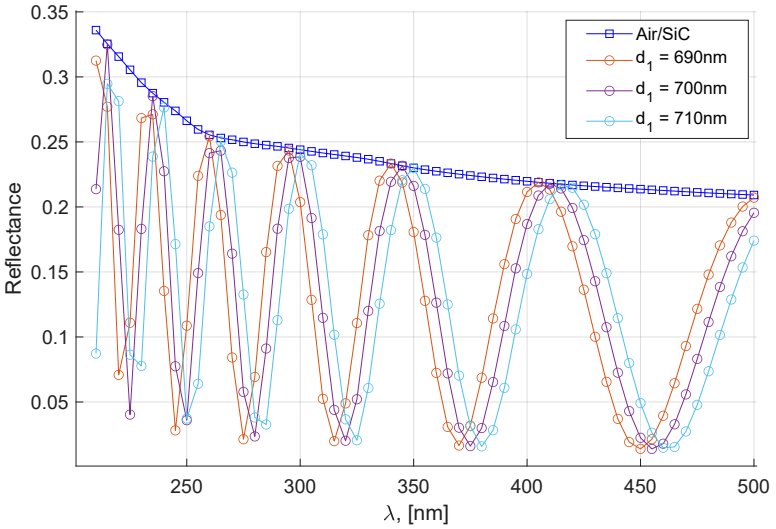

Figure C.5: FRH diode

The light reflected in percentage has been evaluated for the given thickness and for slightly different thicknesses to take into account certain errors which may arise from process variation, just to have a clearer idea on its behaviour. In both figures is reported the reflectance considering just the presence of SiC without any layer on top. At least 20 % of the light is reflected all over the spectral range taken into account, which a very side effect to have a good PD.
Anyway, in *figure C.4*, the presence of the ARC improves increasingly the effective light absorbed, with a valley corresponding in the range between [270; 320] nm depending on the effective thickness of the layer, but at low wavelength the reflected part remain still remarkable and will provoke effect on the responsivity. On the other side, in *figure C.5* the chosen thickness results in an oscillating shape and the performances remain practically unaffected, resulting in a more complex analysis for the effective evaluation of the 4H-SIC FRH photodiode.

C.2 SiO_2/Si

The PDs based on ZnO has different structure with respect to the latter discussed, since the nanocomposite material is on top of all the deposited layer directly in contact with air. In order to have a much closer idea on how reflectance of light affect the devices, it should be examinated the stack composeed of ZnO/SiO_2/Si or ZnO/FusedSilica. Due to the non crystalline and nanoporous morphology of the zinc monoxide film, light will scatter and all the formulas described will no longer be valid, therefore air will be considered in its replacement although the accuracy of the results may differ from reality. Adopting the same procedure used in case of SiC photodiode, in the same spectral range, we obtain:

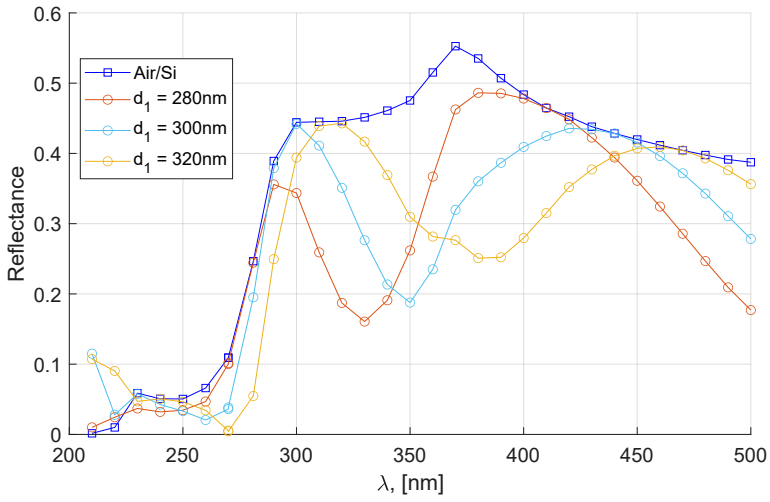

Figure C.6: ZnO PD on Si substrate

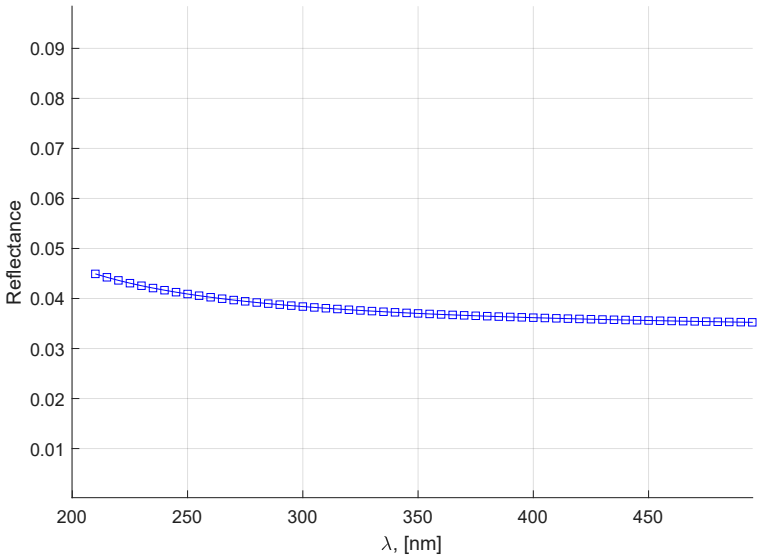

Figure C.7: ZnO PD on fused silica substrate with only the stack Air/Fused Silica

In *figure C.6*, the presence of a dielectric layer alter the reflectivity. Focusing on the curves with ZnO, it may be appreciated that the reflectance is quite high starting from 300 nm reaching roughly 45% that means that almost half of the optical power is completely reflected back, adding also the inhomogeneity of the shape. Moreover, looking at the transmittance results, the effective light absorbed in the zinc oxide structure above 270 nm is given both from the effected beam and part of light transmitted and reflected back, therefore the responsivity may not be coherent in the spectral range analysed in *section 4.3.2*.
Therefore, by analysing the reflectance of a fused silica substrate, as shown in *figure C.7*, we observe that the reflectivity is practically null, avoiding any contribution given by reflection, which translates on a complete absorption or transmission of light after travelling through the ZnO. Furthermore, since the responsivity data has been measured after attaching the dies on a Au package, an analysis on the stack Air/FusedSilica/Au has been asserted, as illustrated in *figure C.8*. There are not remarkable differences with respect to the case where there is only the fused silica due probably to its significant thickness.

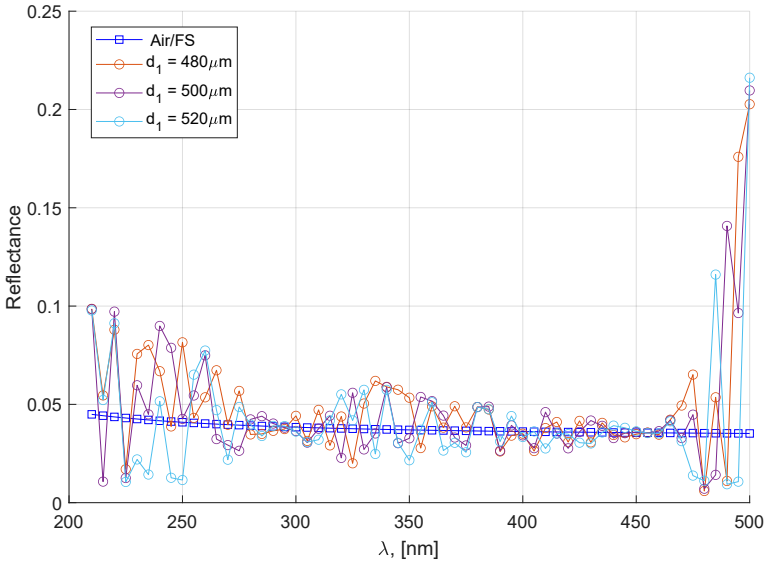

Figure C.8: ZnO PD on fused silica substrate with only the stack Air/Fused Silica

This is why a glass substrate has been chosen, and why all the optical analysis has been carried out only on the devices fabricated on fused silica substrate.

Appendix D

IEEE conference

Accepted manuscript as conference poster in IEEE sensors 2022.

ZnO NANOPARTICLE PRINTING FOR UV SENSOR FABRICATION

Hendrik Joost van Ginkel, Mattia Orvietani, Joost Romijn, Guo Qi Zhang, Sten Vollebregt

Electronic Components, Technology and Materials, Delft University of Technology, Delft, The Netherlands

h.j.vanginkel@tudelft.nl

***Abstract*— In this work, a novel microfabrication-compatible production process is demonstrated and used to fabricate UV photoresistors made from ZnO nanoparticles. It comprises a simple room-temperature production method for synthesizing and direct-writing nanoparticles. The method can be used on a wide range of surfaces and print a wide range of materials. Here, it is used to synthesize, for the first time, a ZnO photoresistor. The sensor shows a two orders of magnitude lower resistance under UV-C exposure compared to darkness. The low cost and simplicity of this synthesis method enables cheap integration of UV-C sensors for human exposure monitoring or UV-output monitoring of light sources.**

Keywords*— *UV sensor, nanoparticles, zinc oxide, spark ablation, printed electronics

I. INTRODUCTION

Wide band-gap semiconductors have attracted significant interest by the semiconductor industry [1]. They are typically hard materials that can operate at higher temperatures than conventional silicon technology and are largely insensitive to optical light [2,3,4]. This makes them excellent candidate materials for selective UV sensing, e.g. for flame detection or for monitoring the power output of UV appliances that are emerging in markets like disinfection, water treatment, etc [5]. One of the wide-bandgap semiconductors of interest for UV sensing is ZnO. ZnO has the benefit of having a direct 3.37 eV bandgap, is non-toxic, chemically and thermally highly stable, has a high radiation hardness, and is widely abundant [2,3,6,7,8]. These properties make ZnO an interesting material for UV sensors that are blind to visible light.

However, applying ZnO is not without difficulty. Zn has a high vapour pressure (6.8 Pa at 422 K) for a metal and will contaminate high vacuum systems [9]. For that reason, and for contamination concerns, its use is often restricted in most semiconductor processing equipment. Deposition is therefore done in dedicated equipment at low vacuum or atmospheric pressure and typically as the last process step. Common methods to deposit ZnO films are evaporating Zn or ZnO [8], sputtering [3,6,10], drop-casting suspended ZnO particles [11], or electroplating [12]. Although these methods can synthesize films of good quality, they require lithography for patterning. A back-end compatible process capable of local deposition on the sensing area would simplify sensor fabrication and reduce costs [8]. This would enable wider adoption for ZnO based devices and open up more possible application areas.

In this work, we propose a method that can direct-write ZnO nanoparticle deposits. The process reported here consists of a spark ablation generator and aerosol impaction printer, see fig. 1. The system only requires a carrier gas, metal electrodes and electricity. It has previously been used to write conducting metal tracks [13], for chemical sensor decoration, [14], and for catalysis [15]. The process can be used to synthesize and immediately deposit a wide range of metal(oxide) nanoparticles at room temperature and is compatible with a wide range of substrates, including flexible or rough substrates provided they are compatible with an ~1 mbar vacuum [16,17].

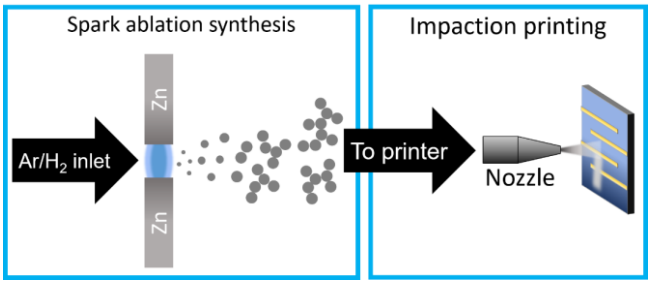

Figure 1. Schematic drawing of the process. Left: A repeating electrical spark (in blue) between two opposing Zn electrodes creates a vapour cloud which rapidly cools down to form nanoparticles (grey spheres) which eventually agglomerate. Right: The aerosol is led to an impaction printer where it is deposited on a device.

We demonstrate, for the first time, that ZnO nanoparticles deposited using spark ablation have a good UV detection capability when used as a photoresistor. Our first results demonstrate that the particles are fully oxidized zincite, show a two orders of magnitude decrease in resistivity when exposed to 265 nm UV, and determine the spectral response of the material.

II. METHODS

A. Substrate prepation

Si wafers were thermally oxidized to have a 300 nm SiO_2 insulating layer. Next, the electrodes were patterned using lithography and a 10/100 nm Cr/Au film was deposited. Lift-off with n-methylpyrrolidone (NMP) was performed to finish the electrode patterning process. The wafer was then diced in 10x10 mm dies and cleaned with acetone, isopropanol, and DI water. The final device has electrode spacings of 160 µm

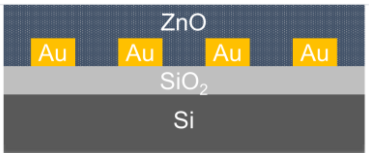

Figure 2. Schematic drawing of the photoresistor devices. Layers and components are not to scale.

between each electrode. A cross-section of the device after coating with ZnO is shown in figure 2.

B. Nanoparticle synthesis and deposition

The nanoparticle synthesis was done with a VSP G1 (VSParticle B.V.) spark ablation generator operating at 3 mA and 1 kV. The spark ablation process is illustrated on the left side in figure 1. Spark ablation uses a repeating spark to ablate material from two opposing doped Zn electrodes (99.95% Zn, 0.05% Al). The resulting metal vapour is carried away by 1.5 l/min. Ar with 5% H_2 gas (1.0 bar) flowing around the electrodes. Ar/H_2 was used to suppress oxidation during deposition and allow the controlled oxidation of the sample after deposition [18]. This should improve particle-to-particle electrical contact. Due to high supersaturation caused by the rapidly cooling gas, nucleation occurs. The nuclei grow and when reaching a final size (5-20 nm, depending on settings), they start to agglomerate [16,17].

The resulting aerosol is then passed to an impaction printer where a pressure drop over a nozzle accelerates the gas. The inertia of the nanoparticles causes them to impact on the substrate surface with enough force to be immobilized. A programmable XYZ-orientable nozzle enables the tool to print complex patterns. The impaction printer is operated at 0.52 mbar with a 0.32 l/min nozzle placed at a 1 mm distance to the sample surface. The deposition process is shown on the right side of figure 1. After deposition, the samples were annealed at 600 °C for six hours in an N_2 atmosphere to complete the oxidation and improve conductivity through sintering.

C. Characterization

Structure characterization was done with scanning electron microscopy (SEM, Hitachi Regulus 8230) operated at 5 kV acceleration voltage and by x-ray diffraction (XRD, Brucker D8 diffractometer with Cu Kα radiation).

To measure the photoresponse of the ZnO devices, two setups were used. The first uses a Microtech probe station equipped with a 5 mW 265 nm LED to measure the charging and discharging time under UV-C exposure. A second, spectral responsivity setup was used to measure the generated current per wavelength. It consists of a combination of a deuterium and a halogen lamp (Bentham D2-QH Deuterium-Halogen Source), whose output is connected to a monochromator (Horiba iHR320). The selected wavelength is moved to the exit slit of the latter device and is then focused on the sample by a UV reflective mirror (CM750-200-F01). The relative output of the photodetector is expressed as voltage per wavelength and an optimal readout circuit has been designed to read out low output voltages.

III. RESULTS

A. Structure

After deposition and annealing, the sample shows cracking around the edges of the printed lines, as can be seen in figure 3A. This is likely due to restructuring during annealing and bad adhesion to the SiO_2 surface. In the middle of the line, where the deposit is the thickest, the cracks are much smaller. At higher magnification, as seen in figure 3B,

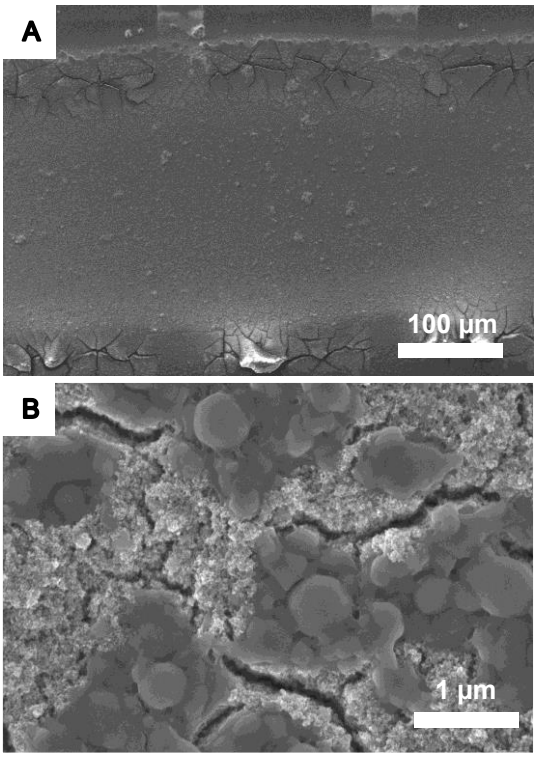

Figure 3. SEM images (Hitachi Regulus 8230, 5 kV) of a nanoparticle deposit on top of electrodes showing cracking at the edges. Note there is no such cracking above the Au electrodes. Inset: close-up in the middle of the line.

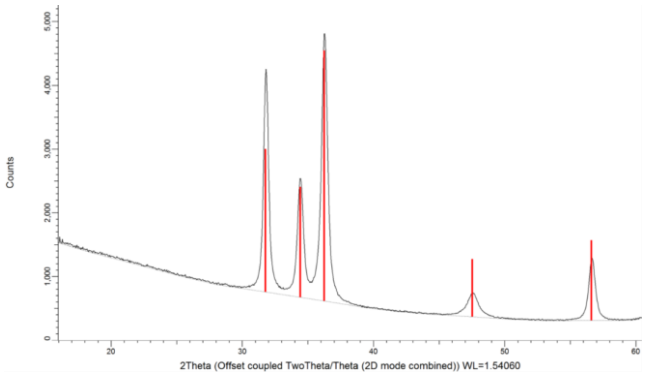

Figure 4. XRD results on a ZnO sample. Red bars indicate the diffraction pattern of zincite.

the nanoporous structure becomes visible and we can observe locally coalesced areas next to micro-cracks. These areas are also formed during the restructuring and possibly local melting of partially oxidized Zn. The thicker area of the film has too much structural strength for cracks to propagate as far as near the edges. Deposition of an adhesion layer would vastly improve the adhesion and reduce delamination and cracking. Removal of cracks would be possible by layered deposition with multiple deposition-annealing cycles to fill any emerging cracks.

The XRD result in figure 4 shows only a zincite phase and no pure Zn crystallites were seen, indicating the sample has been fully oxidized as intended.

B. *Conductivity and UV sensing*

Using a 265 nm LED, four-point-probe IV measurements were done. Despite the micro-cracks the structure electrically conducts. The results shown in figure 5 show Ohmic responses with film resistance of $5.02*10^{10}$ Ω when in complete darkness and $5.82*10^{8}$ Ω when exposed to 265 nm light. This is a nearly two orders of magnitude resistance reduction under UV illumination. As seen in figure 6, it takes several minutes to reach a stable current before and after illumination. The charging time to reach 90% of the plateau value is 79 seconds and discharging to 10% takes 82 seconds. Although the charging and discharge time is slower than other devices reported in literature, the two orders of magnitude response is comparable to other devices [2,3,6,8,10,11]. Considering these are first results of a new, flexible synthesis method with minimal optimization in the design and synthesis process, these values can be expected to improve.

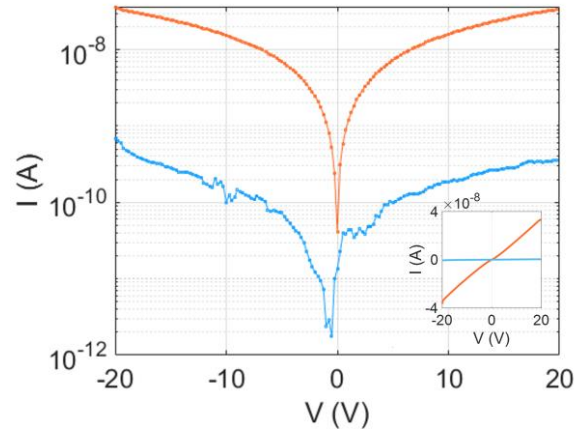

Figure 5. Semilogarithmic IV curves in darkness (blue) and under 265 nm illumination (orange). Inset: The same data plotted with linearly y-axis.

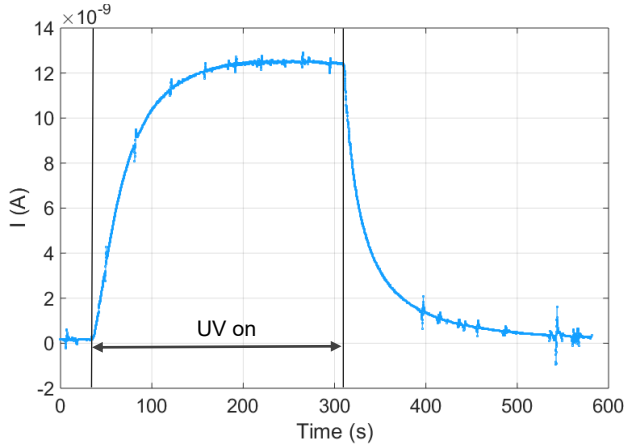

Figure 6. Photo-response curve showing charging and discharging when exposure to 265 nm light starts or stops. Measurement done at 5 V.

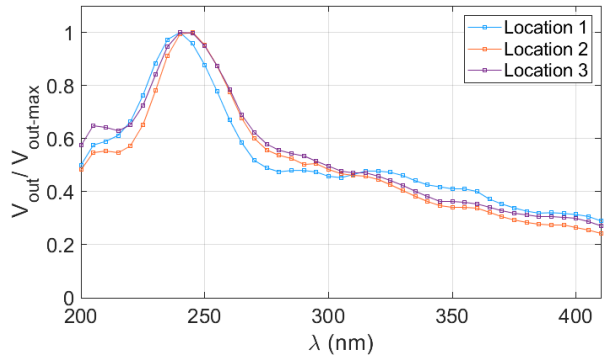

Figure 7. Response per wavelength between 200 and 410 nm for three measurements on one printed ZnO line at a 5 V bias. The curve is normalized for comparison, since changes in illumination intensity and film resistance at different locations affect the response.

The photogenerated current at different wavelengths was measured. Figure 7 shows the spectral response between 200 and 410 nm. Each point was acquired after a 5 min waiting time to ensure the current had stabilized. We can observe a maximum at 240 nm with a steep decline until 280 nm, after which the current slowly keeps declining. With a 3.37 eV bandgap, one would expect photocurrent drop for higher wavelengths than 368 nm. Having an irradiating optical spot bigger than the device itself hampers asserting the light intensity of the measurement. Slight changes in sample location between measurements will therefore change the measured voltage. Future work should add a calibrated reference sensor in parallel to the sample to measure the light intensity during each measurement.

IV. Conclusion

A method to print ZnO films on a broad range of substrates is presented with the first results of UV sensors fabricated this way. The resulting film has a nanoporous structure with partially coalesced areas and is conducting despite crack formation. Under UV-C illumination, resistance is reduced by two orders of magnitude compared to complete darkness, comparable with devices from literature. Charging and discharging times are long, but the devices are relatively large and not optimized yet. Future work should focus on optimization of the sensor design to improve response time and sensitivity. Furthermore, a study for better annealing recipes to reduce resistivity and increase responsivity is needed to further improve the material.

Acknowledgment

We would like to acknowledge the funding provided by NWO grant 729.001.023. We thank VSParticle B.V. for the use of their equipment. We also thank the Else Kooi Lab for facilitating the experiments.

REFERENCES

[1] P. R. Wilson et al., "IEEE ITRW: International Technology Roadmap for Wide-Bandgap Power Semiconductors: An Overview," IEEE Power Electronics Magazine, vol. 5, no. 2, Art. no. 2, Jun. 2018, doi: 10.1109/mpel.2018.2821938

[2] P. S. Shewale and Y. S. Yu, "UV photodetection properties of pulsed laser deposited Cu-doped ZnO thin film," Ceramics International, vol. 43, no. 5, Art. no. 5, Apr. 2017, doi: 10.1016/j.ceramint.2016.12.041.

[3] X. Liu et al., "All-printable band-edge modulated ZnO nanowire photodetectors with ultra-high detectivity," Nature Communications, vol. 5, no. 1, Art. no. 1, Jun. 2014, doi: 10.1038/ncomms5007.

[4] J. Romijn et al., "Visible Blind Quadrant Sun Position Sensor in a Silicon Carbide Technology," Jan. 2022, doi: 10.1109/mems51670.2022.9699533.

[5] G. Knight, "Monitoring of ultraviolet light sources for water disinfection," doi: 10.1109/ias.2004.1348537.

[6] H. S. Al-Salman and M. J. Abdullah, "Fabrication and Characterization of Undoped and Cobalt-doped ZnO Based UV Photodetector Prepared by RF-sputtering," Journal of Materials Science & Technology, vol. 29, no. 12, Art. no. 12, Dec. 2013, doi: 10.1016/j.jmst.2013.10.007.

[7] S. J. Pearton et al., "Recent advances in processing of ZnO," Journal of Vacuum Science & Technology B: Microelectronics and Nanometer Structures, vol. 22, no. 3, Art. no. 3, 2004, doi: 10.1116/1.1714985.

[8] S. K. Panda and C. Jacob, "Preparation of transparent ZnO thin films and their application in UV sensor devices," Solid-State Electronics, vol. 73, pp. 44–50, Jul. 2012, doi: 10.1016/j.sse.2012.03.004.

[9] J. D. McKinley and J. E. Vance, "The Vapor Pressure of Zinc between 150C and 350C," The Journal of Chemical Physics, vol. 22, no. 6, Art. no. 6, Jun. 1954, doi: 10.1063/1.1740276.

[10] Z. Ke et al., "Low temperature annealed ZnO film UV photodetector with fast photoresponse," Sensors and Actuators A: Physical, vol. 253, pp. 173–180, Jan. 2017, doi: 10.1016/j.sna.2016.07.026.

[11] A. J. Gimenez et al., "ZnO-Paper Based Photoconductive UV Sensor," The Journal of Physical Chemistry C, vol. 115, no. 1, Art. no. 1, Dec. 2010, doi: 10.1021/jp107812w.

[12] S. N. Sarangi, "Controllable growth of ZnO nanorods via electrodeposition technique: towards UV photo-detection," Journal of Physics D: Applied Physics, vol. 49, no. 35, Art. no. 35, Aug. 2016, doi: 10.1088/0022-3727/49/35/355103.

[13] H. J. van Ginkel et al., "High Step Coverage Interconnects By Printed Nanoparticles," in 2021 23rd European Microelectronics and Packaging Conference & Exhibition (EMPC), 2021, pp. 1–4, doi: 10.23919/empc53418.2021.9585005.

[14] H. Avdogmus et al., "Dual-Gate Fet-Based Charge Sensor Enhanced by In-Situ Electrode Decoration in a MEMS Organs-On-Chip Platform," Jun. 2021, doi: 10.1109/transducers50396.2021.9495393.

[15] R. Becker et al., "A Scalable High-Throughput Deposition and Screening Setup Relevant to Industrial Electrocatalysis," Catalysts, vol. 10, no. 10, Art. no. 10, Oct. 2020, doi: 10.3390/catal10101165.

[16] T. V. Pfeiffer et al., "New developments in spark production of nanoparticles," Advanced Powder Technology, vol. 25, no. 1, Art. no. 1, 2014, doi: 10.1016/j.apt.2013.12.005.

[17] A. Schmidt-Ott, Spark Ablation: Building Blocks for Nanotechnology, 1st ed. Jenny Stanford Publishing, 2020.

[18] R. T. Hallberg et al., "Hydrogen-assisted spark discharge generated metal nanoparticles to prevent oxide formation," Aerosol Science and Technology, vol. 52, no. 3, Art. no. 3, Dec. 2017, doi: 10.1080/02786826.2017.1411580.

Acknowledgements

At the end of this interesting experience, I would like to express my special thanks of gratitude to both my daily supervisor, Joost2, Joost3 and Sten, for the opportunity of accepting me in joining the lab and showing the fantastic world of WGB. All the discussion has been really inspiring and helpful to achieve what I have done. Unfortunately, owing to external factor, I did not have the time for reaching the final results but I hope to have been helpful somehow. I am also grateful for all the moment shared in non job environment. All the people in the

I wanted to thank also my family, that supported me in this long experience, far from hometown, Perugia„ I have really felt your presence anyhow, as well as my friends I know I have been distance but the will always be there even if long time without seeing each other. I would also like to spend few words for my girlfriend which stood me during my high and low light along the path.

Bibliography

[1] Z. Alaie, S. Mohammad Nejad, and M.H. Yousefi. «Recent advances in ultraviolet photodetectors». en. In: *Materials Science in Semiconductor Processing* 29 (Jan. 2015), pp. 16–55. ISSN: 13698001. DOI: 10.1016/j.mssp.2014.02.054. URL: https://linkinghub.elsevier.com/retrieve/pii/S1369800114001346 (cit. on pp. 1, 2, 16).

[2] N.M. Ravindra and V.K. Srivastava. «Temperature dependence of the energy gap in semiconductors». en. In: *Journal of Physics and Chemistry of Solids* 40.10 (Jan. 1979), pp. 791–793. ISSN: 00223697. DOI: 10.1016/0022-3697(79)90162-8. URL: https://linkinghub.elsevier.com/retrieve/pii/0022369779901628 (cit. on p. 3).

[3] Ahmad Hassan, Yvon Savaria, and Mohamad Sawan. «GaN Integration Technology, an Ideal Candidate for High-Temperature Applications: A Review». en. In: *IEEE Access* 6 (2018), pp. 78790–78802. ISSN: 2169-3536. DOI: 10.1109/ACCESS.2018.2885285. URL: https://ieeexplore.ieee.org/document/8567904/ (cit. on p. 4).

[4] Ümit Özgür, Vitaliy Avrutin, and Hadis Morkoç. «Zinc Oxide Materials and Devices Grown by Molecular Beam Epitaxy». en. In: *Molecular Beam Epitaxy*. Elsevier, 2018, pp. 343–375. ISBN: 978-0-12-812136-8. DOI: 10.1016/B978-0-12-812136-8.00016-5. URL: https://linkinghub.elsevier.com/retrieve/pii/B9780128121368000165 (cit. on p. 5).

[5] Ü. Özgür, Ya. I. Alivov, C. Liu, A. Teke, M. A. Reshchikov, S. Doğan, V. Avrutin, S.-J. Cho, and H. Morkoç. «A comprehensive review of ZnO materials and devices». en. In: *Journal of Applied Physics* 98.4 (Aug. 2005), p. 041301. ISSN: 0021-8979, 1089-7550. DOI: 10.1063/1.1992666. URL: http://aip.scitation.org/doi/10.1063/1.1992666 (cit. on pp. 6, 8, 10).

[6] Hadis Morkoc. *Nitride Semiconductors and Devices*. Springer, 1999. URL: https://link.springer.com/book/10.1007/978-3-642-58562-3 (cit. on p. 6).

[7] W. N. Lawless, C. F. Clark, B. R. Patton, and F. S. Khan. «Electrical and thermal properties of a varistor at cryogenic temperatures». In: *Journal of Applied Physics* 64.8 (1988), pp. 4223–4228. DOI: 10.1063/1.341288. eprint: https://doi.org/10.1063/1.341288. URL: https://doi.org/10.1063/1.341288 (cit. on p. 6).

[8] Norbert H. Nickel and Evgenii Terukov. «Zinc oxide - a material for micro- and optoelectronic applications». In: 2005 (cit. on pp. 8, 9).

[9] D. C. Look, J. W. Hemsky, and J. R. Sizelove. «Residual Native Shallow Donor in ZnO». en. In: *Physical Review Letters* 82.12 (Mar. 1999), pp. 2552–2555. ISSN: 0031-9007, 1079-7114. DOI: 10.1103/PhysRevLett.82.2552. URL: https://link.aps.org/doi/10.1103/PhysRevLett.82.2552 (cit. on p. 9).

[10] D.C. Look, D.C. Reynolds, J.R. Sizelove, R.L. Jones, C.W. Litton, G. Cantwell, and W.C. Harsch. «Electrical properties of bulk ZnO». en. In: 105.6 (Feb. 1998), pp. 399–401. ISSN: 00381098. DOI: 10.1016/S0038-1098(97)10145-4. URL: https://linkinghub.elsevier.com/retrieve/pii/S0038109897101454 (cit. on p. 9).

[11] J. D. Albrecht, P. P. Ruden, S. Limpijumnong, W. R. L. Lambrecht, and K. F. Brennan. «High field electron transport properties of bulk ZnO». en. In: *Journal of Applied Physics* 86.12 (Dec. 1999), pp. 6864–6867. ISSN: 0021-8979, 1089-7550. DOI: 10.1063/1.371764. URL: http://aip.scitation.org/doi/10.1063/1.371764 (cit. on p. 9).

[12] K. Vanheusden, C.H. Seager, W.L. Warren, D.R. Tallant, J. Caruso, M.J. Hampden-Smith, and T.T. Kodas. «Green photoluminescence efficiency and free-carrier density in ZnO phosphor powders prepared by spray pyrolysis». In: *Journal of Luminescence* 75.1 (1997), pp. 11–16. ISSN: 0022-2313. DOI: https://doi.org/10.1016/S0022-2313(96)00096-8. URL: https://www.sciencedirect.com/science/article/pii/S0022231396000968 (cit. on p. 9).

[13] Anderson Janotti and Chris G Van de Walle. «Fundamentals of zinc oxide as a semiconductor». en. In: *Reports on Progress in Physics* 72.12 (Dec. 2009), p. 126501. ISSN: 0034-4885, 1361-6633. DOI: 10.1088/0034-4885/72/12/126501. URL: https://iopscience.iop.org/article/10.1088/0034-4885/72/12/126501 (cit. on pp. 9, 46).

[14] H. Kordi Ardakani. «Electrical conductivity of in situ "hydrogen-reduced" and structural properties of zinc oxide thin films deposited in different ambients by pulsed excimer laser ablation». In: *Thin Solid Films* 287.1 (1996), pp. 280–283. ISSN: 0040-6090. DOI: https://doi.org/10.1016/S0040-6090(96)08744-5. URL: https://www.sciencedirect.com/science/article/pii/S0040609096087445 (cit. on p. 9).

[15] Fabio Quaranta, Antonio Valentini, Federica Rizzi, and Giuseppe Casamassima. «Dual-ion-beam sputter deposition of ZnO films». In: *Journal of Applied Physics* 74 (Aug. 1993), pp. 244–248. DOI: 10.1063/1.354152 (cit. on p. 9).

[16] D.C. Look, D.C. Reynolds, J.R. Sizelove, R.L. Jones, C.W. Litton, G. Cantwell, and W.C. Harsch. «Electrical properties of bulk ZnO». In: *Solid State Communications* 105.6 (1998), pp. 399–401. ISSN: 0038-1098. DOI: https://doi.org/10.1016/S0038-1098(97)10145-4. URL: https://www.sciencedirect.com/science/article/pii/S0038109897101454 (cit. on p. 9).

[17] Seung Yeop Myong, Seung Jae Baik, Chang Hyun Lee, Woo Young Cho, and Koeng Su Lim. «Extremely Transparent and Conductive ZnO:Al Thin Films Prepared by Photo-Assisted Metalorganic Chemical Vapor Deposition (photo-MOCVD) Using AlCl3(6H2O) as New Doping Material». In: *Japanese Journal of Applied Physics* 36.Part 2, No. 8B (Aug. 1997), pp. L1078–L1081. DOI: 10.1143/jjap.36.l1078. URL: https://doi.org/10.1143/jjap.36.l1078 (cit. on p. 9).

[18] A. F. Kohan, G. Ceder, D. Morgan, and Chris G. Van de Walle. «First-principles study of native point defects in ZnO». en. In: *Physical Review B* 61.22 (June 2000), pp. 15019–15027. ISSN: 0163-1829, 1095-3795. DOI: 10.1103/PhysRevB.61.15019. URL: https://link.aps.org/doi/10.1103/PhysRevB.61.15019 (cit. on p. 9).

[19] Chris G. Van de Walle. «Defect analysis and engineering in ZnO». en. In: *Physica B: Condensed Matter* 308-310 (Dec. 2001), pp. 899–903. ISSN: 09214526. DOI: 10.1016/S0921-4526(01)00830-4. URL: https://linkinghub.elsevier.com/retrieve/pii/S0921452601008304 (cit. on p. 9).

[20] S Mridha and D Basak. «Aluminium doped ZnO films: electrical, optical and photoresponse studies». en. In: *Journal of Physics D: Applied Physics* 40.22 (Nov. 2007), pp. 6902–6907. ISSN: 0022-3727, 1361-6463. DOI: 10.1088/0022-3727/40/22/008. URL: https://iopscience.iop.org/article/10.1088/0022-3727/40/22/008 (cit. on p. 10).

[21] Wen Yu et al. «Titanium doped zinc oxide thin film transistors fabricated by cosputtering technique». en. In: *Applied Surface Science* 459 (Nov. 2018), pp. 345–348. ISSN: 01694332. DOI: 10.1016/j.apsusc.2018.07.124. URL: https://linkinghub.elsevier.com/retrieve/pii/S0169433218320221 (cit. on p. 10).

[22] Zhixin Wan et al. «Electrical and optical properties of Ti doped ZnO films grown on glass substrate by atomic layer deposition». en. In: *Materials Research Bulletin* 57 (Sept. 2014), pp. 23–28. ISSN: 00255408. DOI: 10.1016/j.materresbull.2014.04.070. URL: https://linkinghub.elsevier.com/retrieve/pii/S0025540814002554 (cit. on p. 10).

[23] Chris G. Van de Walle, D. B. Laks, G. F. Neumark, and S. T. Pantelides. «First-principles calculations of solubilities and doping limits: Li, Na, and N in ZnSe». In: *Phys. Rev. B* 47 (15 Apr. 1993), pp. 9425–9434. DOI: 10.1103/PhysRevB.47.9425. URL: https://link.aps.org/doi/10.1103/PhysRevB.47.9425 (cit. on p. 10).

[24] Akiko Kobayashi, Otto F. Sankey, and John D. Dow. «Deep energy levels of defects in the wurtzite semiconductors AIN, CdS, CdSe, ZnS, and ZnO». In: *Phys. Rev. B* 28 (2 July 1983), pp. 946–956. DOI: 10.1103/PhysRevB.28.946. URL: https://link.aps.org/doi/10.1103/PhysRevB.28.946 (cit. on p. 10).

[25] P.S. Shewale and Y.S. Yu. «UV photodetection properties of pulsed laser deposited Cu-doped ZnO thin film». en. In: *Ceramics International* 43.5 (Apr. 2017), pp. 4175–4182. ISSN: 02728842. DOI: 10.1016/j.ceramint.2016.12.041. URL: https://linkinghub.elsevier.com/retrieve/pii/S0272884216322933 (cit. on pp. 10, 44).

[26] T. Siva Vijayakumar, S. Karthikeyeni, S. Vasanth, Arul Ganesh, G. Bupesh, R. Ramesh, M. Manimegalai, and P. Subramanian. «Synthesis of Silver-Doped Zinc Oxide Nanocomposite by Pulse Mode Ultrasonication and Its Characterization Studies». en. In: *Journal of Nanoscience* 2013 (Sept. 2013), pp. 1–7. ISSN: 2314-6931. DOI: 10.1155/2013/785064. URL: https://www.hindawi.com/journals/jns/2013/785064/ (cit. on p. 10).

[27] I Ahmad et al. «SYNTHESIS AND CHARACTERIZATION OF SILVER DOPED ZnO NANOPARTICLES FOR HYDROGEN PRODUCTION». en. In: (), p. 14 (cit. on p. 10).

[28] A. Mang, K. Reimann, and St. Rübenacke. «Band gaps, crystal-field splitting, spin-orbit coupling, and exciton binding energies in ZnO under hydrostatic pressure». In: *Solid State Communications* 94.4 (1995), pp. 251–254. ISSN: 0038-1098. DOI: https://doi.org/10.1016/0038-1098(95)00054-2. URL: https://www.sciencedirect.com/science/article/pii/0038109895000542 (cit. on p. 10).

[29] Leonard J. Brillson and Yicheng Lu. «ZnO Schottky barriers and Ohmic contacts». en. In: *Journal of Applied Physics* 109.12 (June 2011), p. 121301. ISSN: 0021-8979, 1089-7550. DOI: 10.1063/1.3581173. URL: http://aip.scitation.org/doi/10.1063/1.3581173 (cit. on pp. 11–13, 22, 46).

[30] Jingxin Jian and Jianwu Sun. «A Review of Recent Progress on Silicon Carbide for Photoelectrochemical Water Splitting». en. In: *Solar RRL* 4.7 (July 2020), p. 2000111. ISSN: 2367-198X, 2367-198X. DOI: 10.1002/solr.202000111. URL: https://onlinelibrary.wiley.com/doi/10.1002/solr.202000111 (cit. on p. 13).

[31] Ulrich Vetter. «Lanthanide Doped Wide Band Gap Semiconductors: Intra-4f Luminescence and Lattice Location Studies». en. PhD thesis. Georg-August-University Göttingen, 2004. DOI: 10.53846/goediss-2860. URL: https://ediss.uni-goettingen.de/handle/11858/00-1735-0000-0006-B555-B (cit. on p. 13).

[32] Catherine Langpoklakpam et al. «Review of Silicon Carbide Processing for Power MOSFET». en. In: *Crystals* 12.2 (Feb. 2022), p. 245. ISSN: 2073-4352. DOI: 10.3390/cryst12020245. URL: https://www.mdpi.com/2073-4352/12/2/245 (cit. on p. 14).

[33] Mohamed L. Megherbi, Hichem Bencherif, Lakhdar Dehimi, Elisa D. Mallemace, Sandro Rao, Fortunato Pezzimenti, and Francesco G. Della Corte. «An Efficient 4H-SiC Photodiode for UV Sensing Applications». en. In: *Electronics* 10.20 (Oct. 2021), p. 2517. ISSN: 2079-9292. DOI: 10.3390/electronics10202517. URL: https://www.mdpi.com/2079-9292/10/20/2517 (cit. on p. 14).

[34] G. Pennington and N. Goldsman. «Self-consistent calculations for n -type hexagonal SiC inversion layers». en. In: *Journal of Applied Physics* 95.8 (Apr. 2004), pp. 4223–4234. ISSN: 0021-8979, 1089-7550. DOI: 10.1063/1.1687977. URL: http://aip.scitation.org/doi/10.1063/1.1687977 (cit. on p. 14).

[35] Mingwei Huang, Neil Goldsman, Chien-Hwa Chang, Isaak Mayergoyz, James M. McGarrity, and Dwight Woolard. «Determining 4H silicon carbide electronic properties through combined use of device simulation and metal–semiconductor field-effect-transistor terminal characteristics». en. In: *Journal of Applied Physics* 84.4 (Aug. 1998), pp. 2065–2070. ISSN: 0021-8979, 1089-7550. DOI: 10.1063/1.368267. URL: http://aip.scitation.org/doi/10.1063/1.368267 (cit. on p. 14).

[36] Xu She, Alex Q. Huang, Óscar Lucía, and Burak Ozpineci. «Review of Silicon Carbide Power Devices and Their Applications». In: *IEEE Transactions on Industrial Electronics* 64.10 (2017), pp. 8193–8205. DOI: 10.1109/TIE.2017.2652401 (cit. on p. 15).

[37] Xiaojun Xu, Alex Huang, Yan Gao, Anant Agarwal, Sumi Krishnaswami, Sei-Hyang Ryu, and Xu Huang. «Performance evaluation of SiC MOSFET/BJT/schottky diode in a 1MHz single phase PFC». In: Apr. 2007, pp. 1268–1272. DOI: 10.1109/APEX.2007.357678 (cit. on p. 15).

[38] C. Codreanu, M. Avram, E. Carbunescu, and E. Iliescu. «Comparison of 3C–SiC, 6H–SiC and 4H–SiC MESFETs performances». en. In: *Materials Science in Semiconductor Processing* 3.1-2 (Mar. 2000), pp. 137–142. ISSN: 13698001. DOI: 10.1016/S1369-8001(00)00022-6. URL: https://linkinghub.elsevier.com/retrieve/pii/S1369800100000226 (cit. on p. 15).

[39] Xiao Guo, Zeyu Peng, Pengbo Ding, Long Li, Xinyi Chen, Haoyun Wei, Zhen Tong, and Liang Guo. «Nonlinear optical properties of 6H-SiC and 4H-SiC in an extensive spectral range». In: *Opt. Mater. Express* 11.4 (Apr. 2021), pp. 1080–1092. DOI: 10.1364/OME.415915. URL: http://opg.optica.org/ome/abstract.cfm?URI=ome-11-4-1080 (cit. on p. 15).

[40] Takashi Mukai, Motokazu Yamada, and Shuji Nakamura. «Current and Temperature Dependences of Electroluminescence of InGaN-Based UV/Blue/Green Light-Emitting Diodes». In: *Japanese Journal of Applied Physics* 37 (1998), p. L1358 (cit. on p. 20).

[41] B. el Mansouri. «Design and processing of silicon and silicon carbide sensors». en. PhD thesis. Delft University of technology, 2021. DOI: 10.4233/UUID:5B19A1EF-8C82-41F0-A6EE-C16402DAA110. URL: http://resolver.tudelft.nl/uuid:5b19a1ef-8c82-41f0-a6ee-c16402daa110 (cit. on pp. 20, 24).

[42] Alessandro Grillo and Antonio Di Bartolomeo. «A current-voltage model for double Schottky barrier devices». en. In: (), p. 15 (cit. on pp. 22, 24).

[43] Zuo Wang et al. «Extraction and Analysis of the Characteristic Parameters in Back-to-Back Connected Asymmetric Schottky Diode». en. In: *physica status solidi (a)* 217.8 (Apr. 2020), p. 1901018. ISSN: 1862-6300, 1862-6319. DOI: 10.1002/pssa.201901018. URL: https://onlinelibrary.wiley.com/doi/10.1002/pssa.201901018 (cit. on pp. 23, 24).

[44] Marc Ullmann, Sheldon K Friedlander, and Andreas Schmidt-Ott. «Nanoparticle Formation by Laser Ablation». en. In: (), p. 11 (cit. on p. 31).

[45] R Reinmann and M Akram. «Temporal investigation of a fast spark discharge in chemically inert gases». In: *Journal of Physics D: Applied Physics* 30.7 (Apr. 1997), pp. 1125–1134. DOI: 10.1088/0022-3727/30/7/010. URL: https://doi.org/10.1088/0022-3727/30/7/010 (cit. on p. 31).

[46] H. Martinen and H. Tholl. In: *Zeitschrift für Naturforschung A* 25.3 (1970), pp. 430–439. DOI: doi:10.1515/zna-1970-0315. URL: https://doi.org/10.1515/zna-1970-0315 (cit. on p. 31).

[47] T.V. Pfeiffer, J. Feng, and A. Schmidt-Ott. «New developments in spark production of nanoparticles». en. In: *Advanced Powder Technology* 25.1 (Jan. 2014), pp. 56–70. ISSN: 09218831. DOI: 10.1016/j.apt.2013.12.005. URL: https://linkinghub.elsevier.com/retrieve/pii/S0921883113002446 (cit. on pp. 31, 32).

[48] Schmidt-Ott. *Introduction to Magnetic Materials*. Jenny Stanford Publishing, (Ed.). (2020), 2020. URL: https://doi.org/10.1201/9780367817091 (cit. on p. 32).

[49] Sebastian Binder, Markus Glatthaar, and Edda Rädlein. «Analytical Investigation of Aerosol Jet Printing». en. In: *Aerosol Science and Technology* 48.9 (Sept. 2014), pp. 924–929. ISSN: 0278-6826, 1521-7388. DOI: 10.1080/02786826.2014.940439. URL: http://www.tandfonline.com/doi/abs/10.1080/02786826.2014.940439 (visited on 02/28/2022) (cit. on p. 33).

[50] Ethan B Secor. «Principles of aerosol jet printing». en. In: *Flexible and Printed Electronics* 3.3 (Sept. 2018), p. 035002. ISSN: 2058-8585. DOI: 10.1088/2058-8585/aace28. URL: https://iopscience.iop.org/article/10.1088/2058-8585/aace28 (cit. on p. 33).

[51] URL: https://www.bentham.co.uk/products/components/ild-d2-qh-deuterium-halogen-source-200-2500nm-86/ (cit. on p. 36).

[52] URL: https://www.thorlabs.com/newgrouppage9.cfm?objectgroup_id=6615 (cit. on p. 37).

[53] Hong-Ying Chen and Fu-Hsing Lu. «Oxidation behavior of titanium nitride films». en. In: *Journal of Vacuum Science & Technology A: Vacuum, Surfaces, and Films* 23.4 (July 2005), pp. 1006–1009. ISSN: 0734-2101, 1520-8559. DOI: 10.1116/1.1914815. URL: http://avs.scitation.org/doi/10.1116/1.1914815 (cit. on p. 40).

[54] URL: https://www.thorlabs.com/thorproduct.cfm?partnumber=PDA10A2 (cit. on p. 51).

[55] URL: https://www.iisb.fraunhofer.de/content/dam/iisb2014/en/Documents/Research-Areas/Devices/FraunhoferIISB_ProductSheet_DEV_Ion-Implanted-SiC-UV-Photodiodes_WWW.pdf (cit. on p. 51).

[56] URL: https://sglux.de/en/produkt/sg01m-5lens-en/ (cit. on p. 51).

[57] C.D. Matthus, Tobias Erlbacher, Alexander Burenkov, Anton J. Bauer, and Lothar Frey. «Ion Implanted 4H-SiC UV Pin-Diodes for Solar Radiation Detection – Simulation and Characterization». In: *Silicon Carbide and Related Materials 2015*. Vol. 858. Materials Science Forum. Trans Tech Publications Ltd, June 2016, pp. 1032–1035. DOI: 10.4028/www.scientific.net/MSF.858.1032 (cit. on p. 52).

[58] Munizer Purica, Elena Budianu, and Emil Rusu. «ZnO thin films on semiconductor substrate for large area photodetector applications». en. In: *Thin Solid Films* 383.1-2 (Feb. 2001), pp. 284–286. ISSN: 00406090. DOI: 10.1016/S0040-6090(00)01579-0. URL: https://linkinghub.elsevier.com/retrieve/pii/S0040609000015790 (cit. on p. 57).

[59] G. Wisz, I. Virt, P. Sagan, P. Potera, and R. Yavorskyi. «Structural, Optical and Electrical Properties of Zinc Oxide Layers Produced by Pulsed Laser Deposition Method». en. In: *Nanoscale Research Letters* 12.1 (Dec. 2017), p. 253. ISSN: 1931-7573, 1556-276X. DOI: 10.1186/s11671-017-2033-9. URL: http://nanoscalereslett.springeropen.com/articles/10.1186/s11671-017-2033-9 (visited on 03/07/2022) (cit. on pp. 57, 58).

[60] Andrew M. Smith and Shuming Nie. «Semiconductor Nanocrystals: Structure, Properties, and Band Gap Engineering». en. In: *Accounts of Chemical Research* 43.2 (Feb. 2010), pp. 190–200. ISSN: 0001-4842, 1520-4898. DOI: 10.1021/ar9001069. URL: https://pubs.acs.org/doi/10.1021/ar9001069 (cit. on p. 58).

[61] Madan Singh, Monika Goyal, and Kamal Devlal. «Size and shape effects on the band gap of semiconductor compound nanomaterials». en. In: *Journal of Taibah University for Science* 12.4 (July 2018), pp. 470–475. ISSN: 1658-3655. DOI: 10.1080/16583655.2018.1473946. URL: https://www.tandfonline.com/doi/full/10.1080/16583655.2018.1473946 (cit. on p. 58).

[62] K.W. Liu et al. «Ultraviolet photoconductive detector with high visible rejection and fast photoresponse based on ZnO thin film». en. In: *Solid-State Electronics* 51.5 (May 2007), pp. 757–761. ISSN: 00381101. DOI: 10.1016/j.sse.2007.03.002. URL: https://linkinghub.elsevier.com/retrieve/pii/S0038110107001049 (cit. on p. 58).

[63] M T Sultan, A Manolescu, H G Svavarsson, and A Valfells. «Solid-state dewetting of silver-thin films: self-assembled nano-geometries». en. In: *IOP SciNotes* 1.3 (Dec. 2020), p. 035203. ISSN: 2633-1357. DOI: 10.1088/2633-1357/abcea2. URL: https://iopscience.iop.org/article/10.1088/2633-1357/abcea2 (cit. on p. 63).

[64] URL: https://refractiveindex.info (cit. on p. 76).